X-Ray Study of Mass Distribution in Clusters of Galaxies

Akira Hayakawa

Department of Physics, Tokyo Metropolitan University
1-1 Minami-Ohsawa, Hachioji, Tokyo 192-0397, Japan

February 17, 2006

Abstract

A cluster of galaxies is the largest structure in the universe, which is an ensemble of 10–1000 galaxies, extending over ∼10 25 cm. It consists of the galaxies, X-ray-emitting hot gas which has a temperature of 10^{7-8} K and has mass several times more than that of the galaxies in total, and the dark matter which is again several times as massive as the hot gas in total. It has been known that some clusters of galaxies which show regular and relaxed morphology often harbor at their center a cD galaxy which is a gigantic elliptical galaxy ($M \sim 10^{13} M_\odot$) with extremely high luminosity and bright halo. Other clusters with the same degree of regularity, on the other hand, do not host such a cD galaxy. The reason to cause such difference has not been clear yet.

To understanding the reason of segregating cD and non-cD clusters, it is certainly of great use to investigate degree of dynamical evolution by means of the X-ray surface brightness. For this purpose, we analyzed the *XMM-Newton* archival data of 20 nearby regular clusters of galaxies, of which 7 and 11 are cD and non-cD type with the redshift $z < 0.2$, respectively, and the other two are distant clusters. In evaluating the radial gravitational mass distribution, we developed a new and model-independent method utilizing the raw X-ray surface brightness, and discovered that the mass distribution under the assumption of hydrostatic equilibrium has a universal slope of $\propto r^{-1.5}$, irrespective of cD/non-cD clusters, at their center. Utilizing this mass distribution, we systematically obtained the virial radius of the clusters which is ∼180 times as large as the critical density of the universe and within which the gas is believed to be virialized after the initial gravitational infall. We finally found that, although the virial radius shows a good correlation with the average temperature of the cluster hot gas, it is only ∼80 % of the radii predicted by the conventional relation. We also found that within ∼1 % of the virialized radius thus obtained, the gravitational mass in the cD type clusters is more concentrated toward the center than the non-cD type clusters. The concentration becomes, however, more unclear in outer radii, and disappears at a radius of 10−20 % of the virial radius. Since the cooling time scale of the X-ray-emitting hot gas is evaluated roughly equal to the Hubble time at around this radius, we consider that the infall of the mass due to the gas cooling plays some role on the formation of the cD galaxy.

In addition to the mass distribution, we also carried our systematic and detailed analysis on the temperature and metallicity distributions. We found that the temperature declines in the region 5−55 % of the virialized radius. The resulting temperature profile is universal as long as we normalize the temperature by an emission-weighted average value for each cluster. The radial abundance profile shows significantly more metal concentration toward the center in the cD type clusters than in the non-cD type clusters.

Contents

List of Figures

List of Tables

Chapter 1

Introduction

Cluster of galaxies have been regarded as the largest virialized systems in the universe with dimensions of 1-5 Mpc across. Since the time-scale for the cluster evolution is comparable to the age of the universe, $\sim$10 Gyr, their properties should reflect the initial condition and the evolutional history over the cosmological time scale.

The constituents of clusters are divided into three components: galaxies, intracluster medium (ICM), and dark matter. The galaxies are mainly observed in the optical band with the number of about few hundreds a cluster. The ICM is a diffuse, X-ray emitting hot plasma with temperatures of typically 10^{7-8} K. Their masses are heavier than the stellar mass by a factor 3-5, and the distributions generally trace the gravitational potential. The dark matter occupies around 80% of the total cluster mass of 10^{14-15} $M_\odot$. The primary energy source of the ICM is considered to be the kinetic energy released through the gas infall into the gravitational potential of the dark matter. The heating mechanism is, however, not yet fully understood. Numerical simulations based on a bottom-up formation scenario predict that the cluster was formed through the mergers of smaller groups and subclusters. Thus, the study of the cluster of galaxy is important to consider the dynamical evolution of the universe.

Around the central region of regular clusters of galaxies, a very luminous elliptical galaxy often exists. The optical luminosity of such a galaxy is typically $L_B \sim 10^{12}$ $L_\odot$, which is $\sim$ 10 times as high as our Galaxy. Since its line-of-sight velocity is often coincident with the systemic velocity of the host cluster, such a galaxy is thought to sit at the bottom of the gravitational potential of the cluster (Leir and van den Bergh 1977). These galaxies are often embedded in an extended amorphous halo, exceeding the typical surface brightness profile of normal ellipticals (de Vaucouleurs 1948). According to this feature, these galaxies are called cD galaxies (Mathews et al. 1964).

Recent observational studies of the clusters with *Chandra* and *XMM-Newton*, which have unprecedented imaging capability and large effective area, unveil a lot of new interesting features around the central cD galaxy: unusual X-ray morphology, for example, in the central dense region of the 2A 0335+096 (Mazzotta et al 2003) and high metallicity concentration toward the center of the AWM 7 (Furusho et al. 2003). On the other hands, a lot of clusters of galaxies which have no central bright cD galaxy (non-cD cluster) exist.

In figure 1.1, we show examples of typical cD and non-cD clusters. The top figure shows the Centaurus cluster which is on of the most famous cD clusters. The bottom figure, on the other hand, displays the non-cD cluster klemola 44. In the optical image of Centaurus cluster, we can see the dominant cD galaxy NGC 4696 at the center of dense population of galaxies, while the klemola 44 cluster has no dominant cD galaxy. However, the X-ray radial brightness profiles show the smooth change of the central brightness slope in both cases, namely no segregation of the cD galaxy from the other, except for slight

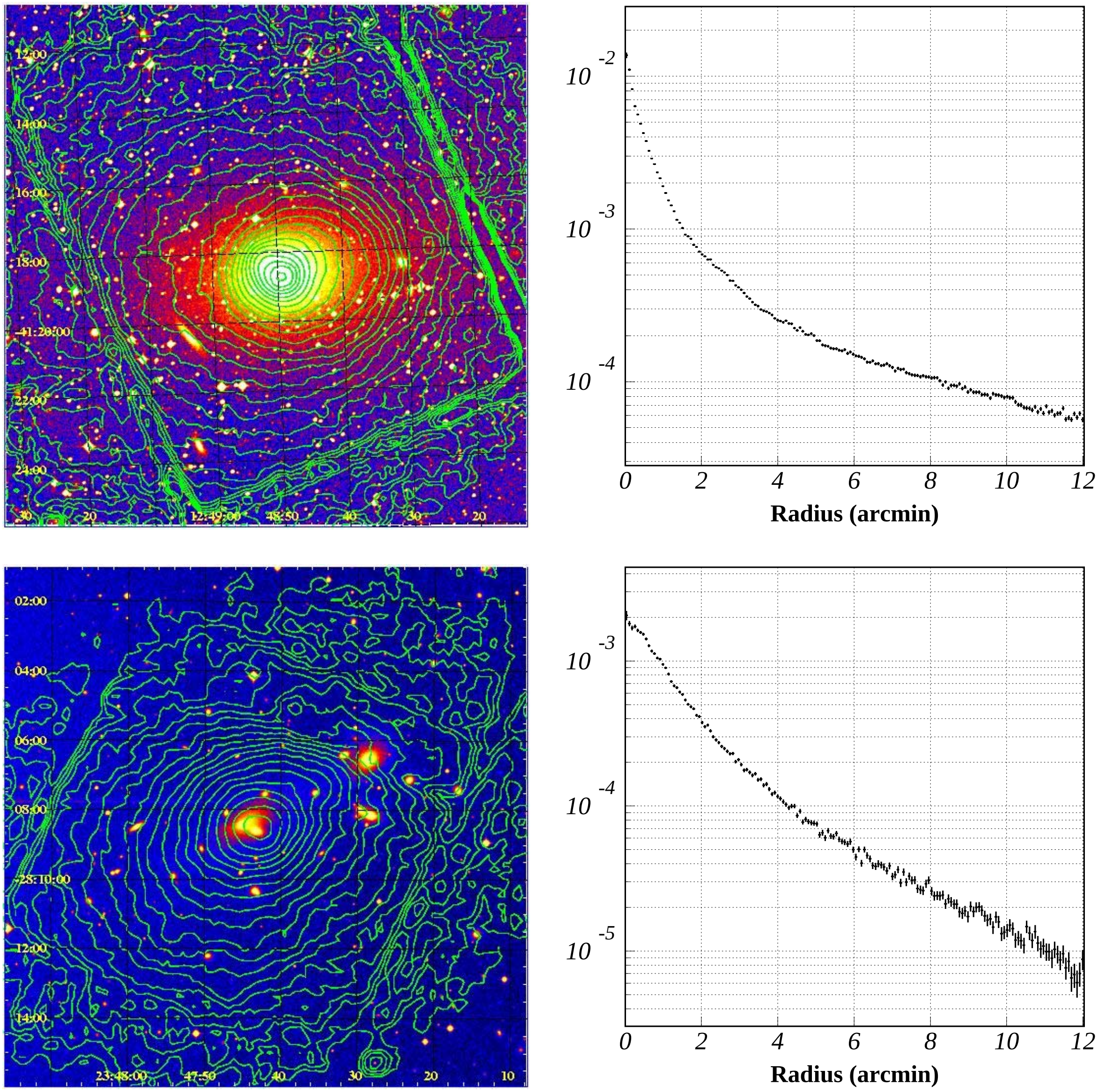

Figure 1.1: Optical (left) image of the $15' \times 15'$ region of Centaurus (top) and klemora 44 (bottom) cluster from the Digitized Sky Survey. The overlaid contours show a smoothed X-ray image which was observed by *XMM-Newton*. The right figure show the radial surface brightness profile centered on the X-ray peak. We normalize these profile by the peak luminosity and plot it against the radius in units of r_{180}.

differece at the central slope associated with the cD galaxy (the right panels of fig. 1.1).

It has been a matter of debate what causes the difference between cD and non-cD clusters. It is widely accepted that the self-gravitational constriction of the dark matter plays the most dominant role on the clusters evolution, and probably so it does for the cD galaxy formation. Accordingly, it is important to investigate gravitational mass distribution of the clusters observationally, in order to study the condition of the cD galaxy formation and, resultingly, the reason to cause the difference between the cD and non-cD clusters. Assuming the hydrostatic equilibrium and the spherical symmetry of ICM, we can calculate the total gravitational mass distribution within the radius as a function of temperature and gas density. In doing this, we use the archival data of *XMM-Newton*, which have unprecedented imaging capability and large effective area, of relatively relaxed nearby twenty clusters of galaxies.

This thesis is organized in the following manner. In the next chapter, we will briefly review the present understanding of cluster structure and introduce important physical quantities used in the later analysis. In Chapter 3, the instruments onbaord *XMM-Newton* that are used in this thesis are described. In Chapter 4, we will explain the cluster sample we collected and data reduction procedure. In Chapter 5, we will study the temperature and abundance distribution based on the spectral analysis. In Chapter 6, we will investigate the cluster total mass distribution with a dark matter model and with a model-independent method developed by ourselves separately. In Chapter 7, we will discuss the implications of the results. Finally in Chapter 8, we will summarize and conclude this thesis.

Throughout this thesis, we assume $H_0 = 75$km s^{-1} Mpc^{-1} with $q_0 = 0.5$. The solar number abundance of iron relative to H is assumed to be 4.68×10^{-5} (Anders & Grevesse 1989).

Chapter 2

Review of Cluster Structure

The hierarchical structure formation in the universe forms the basis of our study. In this chapter, we briefly review the current scenario of the structure formation and its effects on the cluster evolution in order to provide background knowledge for our X-ray study of clusters. We also summarize relevant past results observed in X-rays, and describe previous results on the clusters by summarizing their observed properties of the hot gas and member galaxies.

2.1 Clusters of Galaxies

Clusters of galaxies are the largest well-defined structures in the universe, with a typical linear dimension of 1-3 Mpc. A cluster consists of 100-1000 member galaxies, ranging from the cD galaxy, which belongs to the most luminous galaxy class in the universe, to dwarf galaxies.

In the early 1930s, Zwicky measured velocities of member galaxies in the Coma cluster, and found that they are traveling too fast (~ 1000 km s^{-1} in average) to be gravitationally bound unless the total mass in the cluster greatly exceeds that expected from optical luminosities of member galaxies. This is the first evidence for large-scale dark matter. Through sub sequent measurements velocity dispersions of rich clusters were found typically to be 700 km s^{-1}, implying mass-to-light ratios of $M_{total}/L_{total} \sim 150 - 400\ M_{\odot}/L_{\odot}$ (e.g., Peebles 1993). Here M_{total} and L_{total} are the total dynamical mass and the total optical luminosity, respectively. In contrast, individual galaxies typically have mass-to-light ratios of 10 $M_{\odot}/L_{\odot}$ in their luminous central regions.

With cosmic X-ray observation, witch started in the 1960s, clusters were found to be the most luminous class of X-ray sources in the universe after some types of active galactic nuclei (AGNs). The X-ray emission originates from the intracluster medium (ICM), a hot ($10^7 - 10^8$ K) and low density ($10^{-4} - 10^{-2}$ cm^{-3}) plasma in the intracluster space. Extensive observation with previous X-ray satellites such as *HEAO-1*, *Einstein*, *Ginga*, *ROSAT*, and *ASCA* provided measurements of densities and temperatures of the ICM. These results implied that the mass if the ICM is comparable to, or even greater than that of the stellar component in member galaxies. Characteristic emission lines from ionized heavy elements (mainly from iron) were detected in the X-ray spectra of clusters. The implied sub-solar metallicity of the ICM indicates that the ICM is a mixture of the primordial gas and that reprocessed in the stellar interior. Moreover, X-ray observations of the ICM have provided independent and more accurate measurements of the total mass, and hence of the dark matter, in clusters of galaxies. A rough agreement between the optical and X-ray measurements of the total cluster mass supports the basic assumption that the ICM is in hydrostatic equilibrium. According to a contemporary consensus, about $5-10$ % of a cluster mass is in the stellar component, another $10-20$ % is in the ICM, and the rest is in dark matter.

2.2 Scenario of the evolution in the universe

The evolution of the universe is divided broadly into the structure formation and the chemical evolution. The former is dynamical processes of celestial objects, and the latter represents the production of heavy elements in galaxies. Clusters of galaxies are regarded as useful probes to study both evolutions by several reasons: 1) since the dynamical time-scale of clusters is close to Hubble time, clusters retain the cosmological initial conditions well, 2) clusters can be approximated that they consist of dark matter, hot gas, and galaxies, and also the shape is almost spherical, thus they are easy to deal with, 3) though a part of metals produced in galaxies run away into ICM, they do not escape from clusters. We can thus obtain the total metal abundance without omission. In order to obtain the properties of clusters, X-ray observations are particularly suited, because the X-ray-emitting gas gives us the physical parameters such as temperature, mass, and metal abundance.

2.3 Formation of cluster of galaxies

At present, the hierarchical clustering scenario is widely supported, because it is naturally expected from the cold dark matter model. Also, the fact that the galaxies at redshifts of ~ 5 have been observed, whereas the most distant observed clusters is at $z \sim 1$, indicates that small systems have been formed first. According to the bottom-up scenario, large-scale structures of the universe have formed from infinitesimally small density perturbations at the early universe through the gravitational interaction. A number of numerical simulations for the structure formation have also shown producing the large-scale structures and clusters of galaxies. This result is recognized as a strong support to the hierarchical clustering scenario. Following an early work by White's 700-body simulations (1976), recent calculations, such as the one by Eke, Navarro, and Frenk (1998), include N-body/gas-dynamical simulations as shown in figure 2.1 which are designed to investigate the evolution of clusters. Their result shows hierarchical clustering for the hot gas and dark matter, and indicates that the clusters are formed through subcluster mergers and/or absorption of groups of galaxies.

2.3.1 Collapse condition

In above, we outlined the hierarchical structure formation scenario. In this subsection, we briefly review the collapse scenario according to the spherical collapse model. First of all, consider a mass shell with a radius r_i at epoch $t = t_i$, which is moving with the general expansion until $t = t_i$ (Peebles 1980). The kinetic energy per unit mass of the shell relative to the center is,

$$K_i = \frac{1}{2}(H_i r_i)^2, \tag{2.1}$$

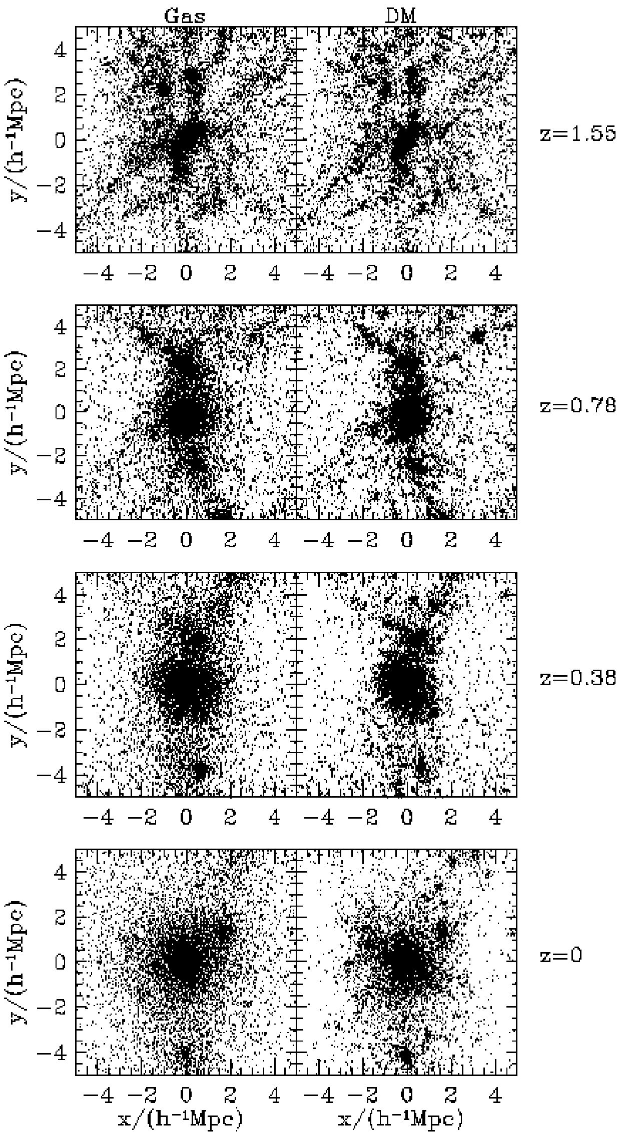

Figure 2.1: Dot plots showing the projected particle positions in cubes of physical size 10 h^{-1} Mpc centered on a cluster at different times (Eke et al. 1998).

where H_i is the Hubble constant at $t = t_i$. Suppose that the average density inside the shell, $\bar{\rho}_i$, is higher than the homogeneous background, $\rho_{b,i}$, by a factor $1 + \delta$, i.e.

$$\bar{\rho}_i = \rho_{b,i}(1+\delta) \tag{2.2}$$

$$= \frac{3}{8\pi G}\Omega_i H_i^2 (1+\delta) \tag{2.3}$$

where Ω_i is the density parameter at $t = t_i$. Then th potential energy per unit mass of the shell is,

$$W_i = -\frac{4\pi G \bar{\rho}_i r_i^3}{3 r_i} \tag{2.4}$$

$$= -\Omega_i K_i (1+\delta). \tag{2.5}$$

Thus the total energy is

$$E = K_i + W_i \tag{2.6}$$

$$= \frac{W_i}{1+\delta}\left[\delta - \left(\frac{1}{\Omega_i - 1}\right)\right]. \tag{2.7}$$

Therefore if $\Omega_i < 1$, when

$$\delta > \frac{1}{\Omega_i} - 1, \tag{2.8}$$

in other words, when

$$\bar{\rho}_i = (1+\delta)\Omega_i \rho_{crit,i} > \rho_{crit,i}, \tag{2.9}$$

total energy is negative and the shell will eventually collapse. Here, we use the critical density $\rho_{crit,z}$ at the redshift z as,

$$\rho_{crit,z} = \frac{3H_z^2}{8\pi G}, \tag{2.10}$$

where

$$H_z = H_0\ E(z), \tag{2.11}$$

$$E^2(z) = \Omega_0(1+z)^3 + \Omega_\Lambda, \tag{2.12}$$

$$\Omega_0 = \frac{8\pi G\rho_0}{3H_0^2}; \qquad \Omega_\Lambda = \frac{\Lambda}{3H_0^2}. \tag{2.13}$$

Here ρ_0 is the non-relativistic matter density, R is the radius of curvature, H_0 is the current Hubbule constant, and Λ is the cosmological constant.

If the density parameter, Ω_i, is close to unity, density perturbations with a small amplitude can collapse. Thus clusters of galaxies are effectively formed in such epochs. Figure 2.2 shows how the radii of over-dense spheres behave during the expansion of the universe. For a large initial over-density, the expansion is stopped at an early stage and the system collapses into a virialized system.

2.3.2 Virial radius and the virial density

We assume that the amplitude of the density perturbation is small, i.e $\delta \ll 1$. Then we have,

$$\frac{d^2r}{dt^2} = -\frac{GM}{r^2} \tag{2.14}$$

where M is the mass inside the shell and the constant (Gunn & Gott 1972). The first integral of this equation is,

$$\left(\frac{dr}{dt}\right)^2 = \frac{2GM}{r} + C. \tag{2.15}$$

C is a constant, and the total energy $C/2$ must be negative for collapse to occur. The solution of equation 2.15 is given in a parametric form,

$$t = \frac{GM}{|C|^{3/2}}(\theta - \sin\theta) \tag{2.16}$$

$$r = \frac{GM}{|C|}(1-\cos\theta). \tag{2.17}$$

The radius, r, is 0 at $\theta = 0$, i.e. $t = 0$. Then it increases with increasing θ. It takes the maximum,

$$r_m = \frac{2GM}{|C|} \tag{2.18}$$

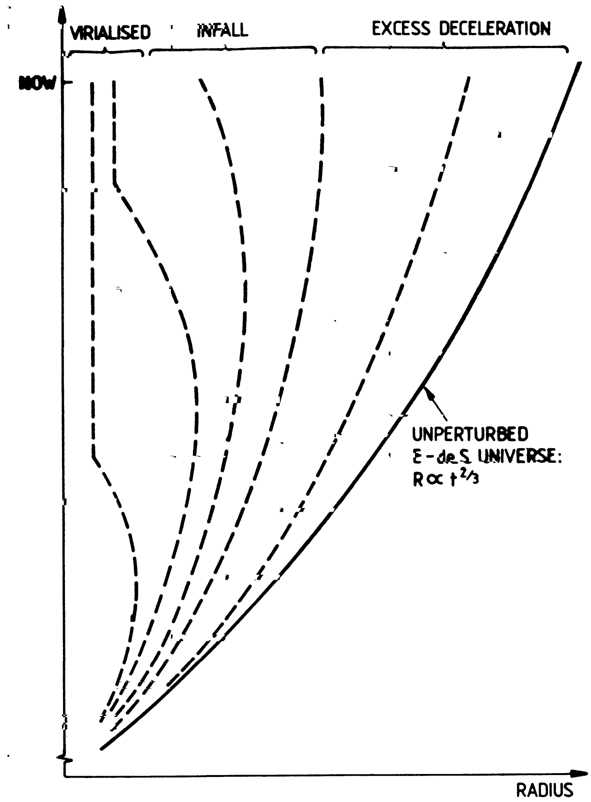

Figure 2.2: The dynamics of over-dense spheres in the expanding universe. The larger initial over-density, the earlier the sphere's expansion halts (Rees 1992).

at $\theta = \pi$, i.e.

$$t = t_m = \frac{\pi GM}{|C|^{3/2}} \tag{2.19}$$

(turn around). Then it shrinks to 0 and again at $\theta = 2\pi$, i.e.

$$t = t_c = \frac{2\pi GM}{|C|^{3/2}} \tag{2.20}$$

(collapse). After collapse, the system will be virialized. In the virialized system, the potential energy is related to the total energy as $W = 2E$. Assuming the radius of the system after virialization is r_{vir}, we have

$$W = -\frac{GM^2}{r_{vir}} = 2E = -2\frac{GM^2}{r_m}. \tag{2.21}$$

Therefore, $r_{vir} = r_m/2$. The average density inside the virial radius r_{vir} is

$$\bar{\rho}_{vir} = \frac{3}{4\pi}\frac{|C|^3}{G^3M^2}. \tag{2.22}$$

On the other hand, the solution of equation 2.15 with $C = 0$ describes the background expansion, because $\Omega \sim 1$. The solution is

$$\rho_{vir} = \left(\frac{9}{2}GM\right)^{1/3} t^{2/3}. \tag{2.23}$$

Thus we obtain the important relation,

$$\Delta_{crit} = \frac{\bar{\rho}_{vir}}{\rho_{crit}} = 18\pi^2. \tag{2.24}$$

We can assume that a cluster is virialized within the radius within which the average density is equal to Δ_{crit} times the critical density of the collapsed epoch. Furthermore, For a ΛCDM cosmology, Δ_{crit} is described as

$$\Delta_{crit} = 18\pi^2 + 82x - 39x^2, \tag{2.25}$$

where

$$x = \Omega(z) - 1, \tag{2.26}$$

$$\Omega(z) = \frac{\Omega_0(1+z)^3}{\Omega_0(1+z)^3 + \Omega_\Lambda}, \tag{2.27}$$

(Bryan & Norman 1998).

2.4 Mass distribution

2.4.1 Hydrostatic equilibrium and gravitational mass distribution

Since the collision time scale for ions and electrons in the intracluster gas are much shorter than the time scales of the heating or cooling, we can treat the gas as a fluid (Sarazin 1988). In general, the time required for a sound wave in the intracluster gas to cross a cluster (sound crossing time) is shorter than the probable age of a cluster. Therefore we can assume that the ICM is under the hydrostatic equilibrium, so that the pressure gradient is balanced with the gravitational force as,

$$\nabla P_{gas} = -\mu m_p n_{gas} \nabla \phi. \tag{2.28}$$

Here P_{gas} and n_{gas} are the ICM pressure and number density, ϕ is the gravitational potential, and $\mu \sim 0.6$ is the mean molecular weight relative to the proton mass m_p. Since the ICM density is quite low, the ICM pressure can be expressed as

$$P_{gas} = n_{gas} kT = \frac{\rho_{gas}}{\mu m_p} kT, \tag{2.29}$$

where k is the Boltzman constant, and ρ_{gas} is the ICM mass density. When we assume a spherical symmetry, the equation 2.28 becomes

$$\frac{dP_{gas}}{dr} = -\mu m_p n_{gas} \frac{GM_{tot}(<r)}{r^2}, \tag{2.30}$$

where G is the gravitational constant, and $M_{tot}(<r)$ is the gravitational (total) mass (i.e. the dark matter + galaxies + hot gas) within the radius r. Thus, we obtain the total mass as

$$\begin{aligned} M_{tot}(<r) &= -\frac{r^2 k}{\mu m_p G n_{gas}} \frac{d}{dr}(n_{gas} T) & (2.31) \\ &= -\frac{kTr}{\mu m_p G}\left(\frac{d \ln n_{gas}}{d \ln r} + \frac{d \ln T}{d \ln r}\right), & (2.32) \end{aligned}$$

that is to say, once we measure the ICM density distribution $n_{gas}(r)$ and the temperature distribution $T(r)$, we can estimate the total mass distribution.

2.4.2 β-model

If the heat conduction were sufficiently rapid compared to the other important time scales, the gas would become isothermal. Substituting the equation 2.29 into the equation 2.28 and assuming the ICM temperature T is constant, we obtain

$$\frac{d\ln\rho_{gas}}{dr} = -\frac{\mu m_p}{kT}\frac{d\phi(r)}{dr}. \tag{2.33}$$

Similarly, assuming that the galaxies are in hydrostatic equilibrium, the hydrostatic equation of the galaxies is written as,

$$\frac{d\ln\rho_{gal}}{dr} = -\frac{1}{\sigma^2}\frac{d\phi(r)}{dr}. \tag{2.34}$$

From equation 2.33 and 2.34, we obtain

$$\rho_{gas} \propto \rho_{gal}^{\beta} \tag{2.35}$$

where

$$\beta \equiv \frac{\mu m_p \sigma^2}{kT}. \tag{2.36}$$

King (1962) has derived an analytic approximation to the isothermal sphere of self-gravitational isothermal collision-less particles. The density profiles of the galaxies have been found to be well approximated with the King profile,

$$\rho_{gal}(r) \sim \rho_{King}(r) = \rho_{King}(0)\left[1+\left(\frac{r}{r_c}\right)^2\right]^{-\frac{3}{2}}. \tag{2.37}$$

Then the isothermal gas distribution may be represented as

$$\rho_{gas}(r) = \rho_{gas}(0)\left[1+\left(\frac{r}{r_c}\right)^2\right]^{-\frac{3}{2}\beta}. \tag{2.38}$$

The surface brightness profile of an isothermal spherical plasma with a radial density profile given by equation 2.38 is calculated by integrating the local emission per unit volume given by equation 2.69 and the EM given by equation 2.70 along the line of sight (l). We obtain the X-ray surface brightness $S(r)$ at projected radius r,

$$\begin{aligned} S(r) &= \Lambda(T,Z)\int n_{gas}^2\ dl & (2.39)\\ &= 2\pi\Lambda(T,Z)\int_{-\infty}^{+\infty} dl\ \ n_{gas}^2(0)\left[1+\left(\frac{r^2+l^2}{r_c^2}\right)\right]^{-3\beta} & (2.40)\\ &= S(0)\left[1+\left(\frac{r}{r_c}\right)^2\right]^{-3\beta+\frac{1}{2}}. & (2.41)\end{aligned}$$

Once we have obtained the β profile parameters to characterize the surface brightness distribution, we can estimate the three-dimensional density profile of the gas. Here, the total X-ray luminosity $L_X(< R)$ within the radius R is written as,

$$\begin{aligned} L_X(< R) &= \int_0^R S(r)dr & (2.42)\\ &= \frac{\pi^{3/2}n_0^2 r_c^3\Lambda}{3\beta-1}\left[1-\left(\frac{r_c^2}{r_c^2+R^2}\right)^{3\beta-2}\right]\frac{\Gamma(3\beta-3/2)}{\Gamma(3\beta-1)} & (2.43)\end{aligned}$$

where the n_0 is the ICM number density at $r = 0$. In order to estimate the 3-dimensional density profile based on the equation 2.41, we calculate the n_0 using equation 2.43. A detailed estimation of equation 2.43 is summarized in Appendix A. When we obtained the 3-dimensional β-model density profile, we derive the total mass of the cluster inside a radius r from the assumption of hydrostatic equilibrium (eq. 2.31.),

$$\begin{aligned} M(r) &= \frac{3kT\beta r}{\mu m_p G}\frac{(r/r_c)^2}{1+(r/r_c)^2} && (2.44)\\ &\propto \beta\, T\, r. && (2.45)\end{aligned}$$

In an actual observation, we can obtain the 2-dimensional surface brightness profile as described in equation 2.41.

It has been known that the observed cluster X-ray surface brightness is well fitted by equation 2.41 with $\beta \sim 0.7$ on average (e.g. Jones & Forman 1984). However resent observational studies of the clusters with *Chandra* and *XMM-Newton* observation, which have unprecedented imaging capability and large effective area, reveal that a lot of clusters could not represent by the simple β profile.

2.4.3 Dark matter density distribution

As discussed in the previous subsection, the gas density profile of X-ray clusters of galaxies are known to be approximated by the equation 2.38. Theoretically, this is consistent with the observed indication that luminous member galaxies obey the King profile and the assumption of the hydrostatic equilibrium of cluster gas. The galaxies in clusters, however, constitute a very small fraction of the gravitational mass of the entire cluster because of the presence of dark matter. Recent high-resolution N-body hydrodynamical simulations have strongly suggested that dark halos of cluster scales are described by a family of fairly universal density profiles. Nabarro, Frenk, & White (1996, and 1997) found from their numerical simulations of structure formation, that the virialized dark matter halos with masses over several orders of magnitude follow a universal density profile,

$$\rho_{DM}(r) = \frac{\rho_s}{(r/r_s)(1+r/r_s)^2}, \tag{2.46}$$

where ρ_s and r_s are the characteristic density and length, respectively. ρ_s is related to the critical density of the universe ρ_{crit} and characteristic density δ_c through $\rho_s = \delta_c \rho_{crit}$. Instead of the flat core of the King profile, the NFW profile has a core with $\propto r^{-1}$ dependence.

Suto, Sasaki, & Makino (1998) generalize the NFW profile in equation 2.46 and consider a family of density profiles describing the dark matter halo

$$\rho_{DM}(x) = \frac{\rho_s}{x^\mu(1+x^\nu)^\lambda}, \tag{2.47}$$

where $x \equiv r/r_s$ is the dimensionless radius in units of the characteristic scale r_s. Then the total mass of the dark matter halo within the radius r is given by

$$M(r) = 4\pi\rho_s r_s^3 m(r/r_s), \tag{2.48}$$

with

$$m(x) \equiv \int_0^x \frac{u^{2-\mu}}{(1+u^\nu)^\lambda} du. \tag{2.49}$$

If one neglects the gas and galaxy contributions to the gravitational mass, the gas density profile ρ_{gas} in hydrostatic equilibrium with the above dark matter potential satisfies the equation 2.30 and described as

$$\frac{d\ln\rho_{gas}}{dr} = -\frac{\mu m_p}{kT}\frac{GM(r)}{r^2}. \tag{2.50}$$

Equation 2.50 can be formally integrated to yield

$$\ln\frac{\rho_{gas}(r)}{\rho_{gas,0}} = -B\int_0^{r/r_s}\frac{m(x)}{x^2}dx, \tag{2.51}$$

where

$$B \equiv \frac{4\pi G\mu m_p \rho_s r_s^2}{kT}. \tag{2.52}$$

With the density profile of the form in equation 2.46, equation 2.51 converges for $\mu < 2$ and is rewritten as

$$\rho_{gas}(r) = \rho_{gas,0}\exp[-B\ f(r/r_s)], \tag{2.53}$$

where

$$f(x) = \int_0^x \frac{m(u)}{u^2}du. \tag{2.54}$$

In some specific cases, this equations are analytically integrated and $f(x)$ is described as follows.

1. $\mu = 1, \nu = 1, \lambda = 2$ (NFW)

$$f(x) = 1 - \frac{1}{x}\ln(1+x) \tag{2.55}$$

2. $\mu = 3/2, \nu = 3/2, \lambda = 1$ (Moore's profile)

$$f(x) = \frac{x-2}{3x}\ln(1+\sqrt{x^3}) + \ln(1+\sqrt{x}) + \frac{2}{\sqrt{3}}\tan^{-1}\frac{2\sqrt{x}-1}{\sqrt{3}} + \frac{\sqrt{3}}{9}\pi \tag{2.56}$$

3. $\mu = 3/2, \nu = 1, \lambda = 3/2$

$$f(x) = 2\sqrt{\frac{1+x}{x}} - \frac{2}{x}\ln(\sqrt{x}+\sqrt{1+x}) \tag{2.57}$$

Furthermore, based on the above gas density profile, Suto, Sasaki, & Makino (1998) computed the gas density profile in hydrostatic equilibrium in the case of $\mu = \alpha$, $\nu = 1$, and $\lambda = 3 - \alpha$ with the restriction $1 < \alpha < 2$. Note that the case with $\alpha = 1$,$\nu = 1$, and $\lambda = 2$ corresponds to the NFW model. They further computed the X-ray surface brightness distribution at a projected radius r on the sky, and derived a useful fitting formula in the following generalized shape.

$$S(\phi) \propto \frac{1}{[1+(\phi/\phi_c)^\zeta]^\eta}\quad,\quad \phi \equiv \frac{\theta}{\theta_s} \tag{2.58}$$

$$\phi_c = 0.3\left(\frac{2}{\alpha} - 1\right) \tag{2.59}$$

$$\zeta = 0.41 - 5.4(2-\alpha)^6 + (0.585 + 6.47\alpha^{-5.1B})B^{\alpha^6/30} \tag{2.60}$$

$$\eta = -0.68 - 5.09(\alpha-1)^2 + (0.202 + 00206\alpha^8)B^{1.1} \tag{2.61}$$

These are valid for $5 \le B \le 20$ and $1.0 \le \alpha \le 1.6$ in the range of $10^{-4} \le \phi \le \phi_{max}$, where $S(\phi_{max}) = 10^{-4}S_0$.

2.5 Observational studies of cluster evolution

2.5.1 X-ray emission process

The X-ray spectrum emitted from an ionized plasma of the low density ($\sim 10^{-3}$ cm^{-3}) ICM is described with a combination of thermal bremsstrahlung (free-free) emission and line emission from heavy elements. In the temperature range of typical cluster (1 keV$<$ $kT <$ 10 keV) the total emission is dominated by the free-free emission if the abundance of heavy elements does not exceed the solar abundance by very much. The emissivity of the free-free emission at a frequency ν from a hot plasma with an electron temperature of T_g is given by

$$\epsilon_\nu = \frac{2^5\pi e^6}{3m_e c^3}(\frac{2\pi}{2m_e k})^{1/2} n_e \sum_i Z_i^2 n_i g_{ff}(Z, T_g, \nu) \times T_g^{-1/2}\exp(-h\nu/kT_g) \tag{2.62}$$

$$= \Lambda(T, Z, \nu) n_e^2 \tag{2.63}$$

where Z_i and n_i are the charge and number density of the ion i, respectively, and n_e is the electrons number density (e.g. Rybicki & Lightman 1979). The Gaunt factor is a correction factor for quantum mechanical effects and is approximately $g_{ff} \sim 0.9(h\nu/kT)^{-0.3}$. The emissivity in a given bandpass, $\nu_1 < \nu < \nu_2$, is then

$$\epsilon^{ff} = \int_{\nu_1}^{\nu_2} \epsilon_\nu^{ff} d\nu \tag{2.64}$$

$$= \Lambda(T, Z) n_e^2. \tag{2.65}$$

The $\Lambda(T, Z)$ is the cooling function, with T and Z representing the plasma temperature and the heavy element abundance, respectively. Figure 2.3 shows the cooling function as a function of the plasma temperature assuming the cosmic abundances. The contribution

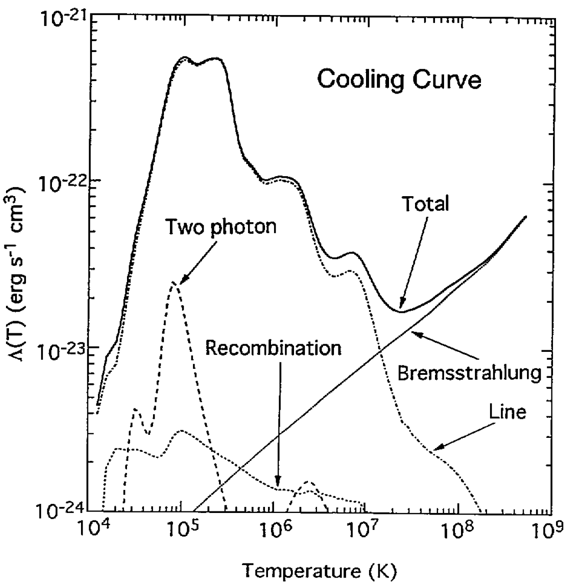

Figure 2.3: Temperature dependence of the cooling function with its components for optically thin plasma containing cosmic abundances of elements (Gehrels & Williams 1993).

of the bremsstrahlung continuum to Λ increases as $\propto T^{1/2}$.

We can obtain the total X-ray luminosity by integrating equation 2.65. It is useful to define the emission integral as

$$EI = \int n_e^2 dV, \tag{2.66}$$

where V is the volume of the cluster. If we assume that th ICM has a spatially-uniform temperature and abundance in the volume V, and that the ICM density is constant over the projected sky area S, then the luminosity L_X is given as

$$\begin{aligned} L_X &= \int \epsilon^{ff} dV & (2.67) \\ &= EI \times \Lambda(T, Z) & (2.68) \\ &= EM \times S \times \Lambda(T, Z). & (2.69) \end{aligned}$$

The EM is the emission measure defined as

$$EM = \int n_e^2 dl, \tag{2.70}$$

where l is the depth of the plasma along the line of sight. The emission integral determines the normalization of the spectrum, and the shape of the spectrum depends only on the temperature T and the heavy element abundance Z, and EI (or EM if S is known) from the observed X-ray spectra.

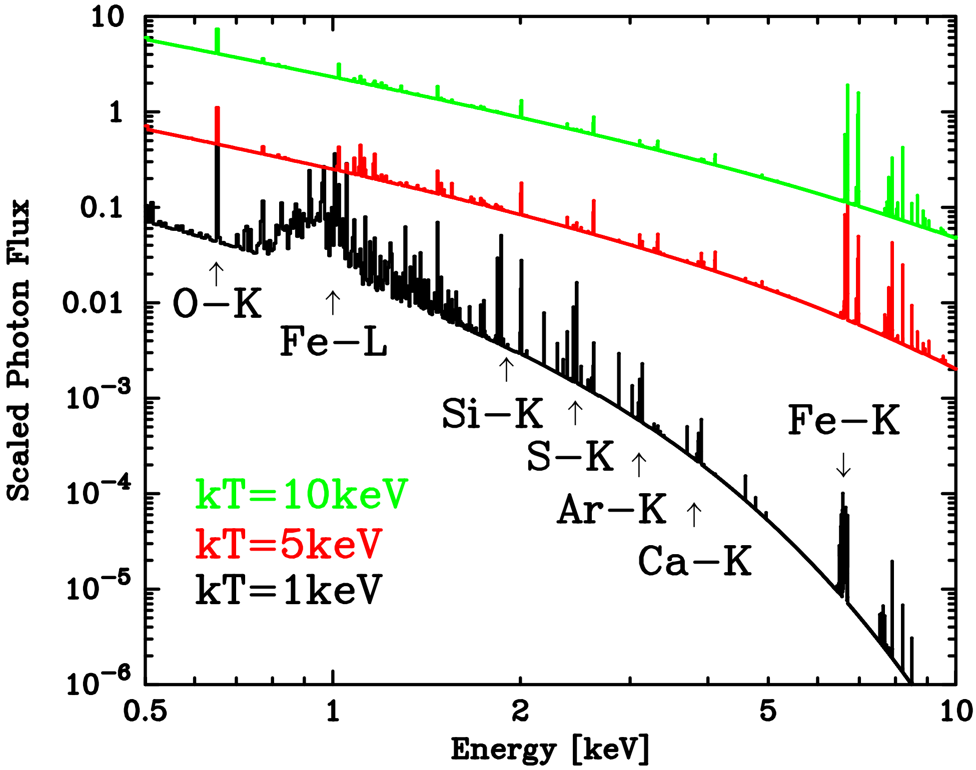

Figure 2.4: Calculated X-ray spectra from optically thin hot plasmas with various temperatures. The MEKAL plasma emission code is used, assuming a metal abundance of 0.3 solar. Vertical scale is arbitrary.

Emission of atomic lines becomes significant when the ICM temperature falls below a few keV. Since the temperature of the ICM is of the same order as the K-shell ionization potentials of heavy elements such as O, Ne, Mg, Si, S and Fe, these elements become mainly He/H-like ions and are completely ionized. These ions are collisionally excited, and then emit their resonance K-lines. In lower temperature clusters, in which Fe ions are not only He-like but also of a low ionization status, the spectrum exhibits resonance L-lines at $\sim$ 1 keV. We show predicted X-ray spectra for various temperature in figure 2.4.

The emission lines and continuum spectra from the ionization equilibrium plasma have been calculated by various authors, e.g. Raymond & Smith (1977), Kaastra & Mewe (1993), and so on. In this thesis, we use the MEKAL code, which is based on the model calculations of Mewe, Lemen, & van den Oord (1986) and Laastra & Mewe (1993) with Fe L calculations by Liedahl, Osterheld & Goldstein (1995), in the XSPEC data analysis Package.

2.5.2 Morphology

The X–ray morphology of clusters is classified by Jones and Forman (1984) as shown in table 2.1. Roughly speaking, there are two types of the X-ray morphology. One type has a circularly symmetric X-ray emission sharply centered on the cD galaxy (XD type), and the other type does not have such a sharp X-ray peak associated with any galaxies (nXD typ). Moreover, either type is subdivided into two groups; so-called early systems and late systems. Early systems have a high X-ray luminosity and a low fraction of spiral galaxies, and they are thought to be dynamically evolved according to their galaxy distribution. Rich clusters are typical early systems. Late systems have a low X-ray luminosity and a high fraction of spiral galaxies, and a thought to be dynamically young. Poor clusters are examples of typical late systems.

nXD	XD
Large core radius ($\sim$400–800 kpc)	Small core radius ($<$300 kpc)
	Central, dominant galaxy
Early system—A1367:	Early systems—Virgo, A262:
Low X-ray luminosity ($<10^{44}$ ergs s^{-1})	Low X-ray luminosity ($<10^{44}$ ergs s^{-1})
Cool X-ray gas (1–4 keV)	Cool X-ray gas (1–4 keV)
No central cooling flows	Central cooling flows
X-ray emission around galaxies	X-ray emission from halo of central galaxy
High spiral fraction ($>$40%)	High spiral fraction ($>$40%)
Low central galaxy density	Low central galaxy density
Irregular cluster structure	Irregular cluster structure
Evolved systems—Coma, A2255, A2256:	Evolved systems—A85, A1795, Perseus:
High X-ray luminosity ($>10^{44}$ ergs s^{-1})	High X-ray luminosity ($>10^{44}$ ergs s^{-1})
Hot X-ray gas ($\geq$6 keV)	Hot X-ray gas ($\geq$6 keV)
No central cooling flows	Central cooling flows
High velocity dispersion	High velocity dispersion
Low spiral fraction ($\lesssim$20%)	Low spiral fraction ($\lesssim$20%)
High central galaxy density	High central galaxy density
Regular, symmetric cluster structure	

Table 2.1: Classifications of galaxies based on the X-ray morphology by Jones and Forman (1984).

2.5.3 Temperature structure

Recent experiments made it possible to obtain spatially resolved spectra of clusters, and are revealing the temperature structure. Markevitch et al. (1998) analyzed spatially resolved X-ray spectra of 30 nearby clusters with ASCA and ROSAT. They reported that most of them show a similar temperature decline at large radii, and about a half of the sample shows signs of merging. Determination of the dynamical structure of the clusters can constrain cosmological models because clusters should be dynamically more relaxed in a low-density universe than in a high-density one (e.g. Richstone et al. 1992). Comparing the temperature profiles with the results of cluster hydrodynamic simulations, Markevitch et al. (1998) found the low Ω (0.3) cosmological models are suitable to explain the temperature profiles.

For example, we cite two instances of 2-dimensional temperature structures of the Coma cluster and A754. Figure 2.5 shows color-coded temperature map of the Coma cluster obtained from ASCA (Watanabe et al. 1999) and XMM-Newton (Arnaud et al. 2000). The extended north-west region is clearly hotter than the surrounding regions. This result indicates the evidence of a recent merger in the Coma cluster. It is interesting to see no substructure in the X-ray image around the hot region. Hence, the temperature structure gives us much information of merging, which is not given by the morphology only. Note that the Coma cluster also shows that the abundance distribution is almost uniform. This probably mean that the metals in the Coma cluster are mixed by mergers. Figure 2.6 shows temperature map with CXO (Markevitch et al. 2000) and simulated result for A754 (Roettiger et al. 1998). The north small region of substructure shows a hot spot (fig. 2.6 left), which is expected to be due to the shock heating. The numerical simulation for A754 represents quite similar structure of the temperature map.

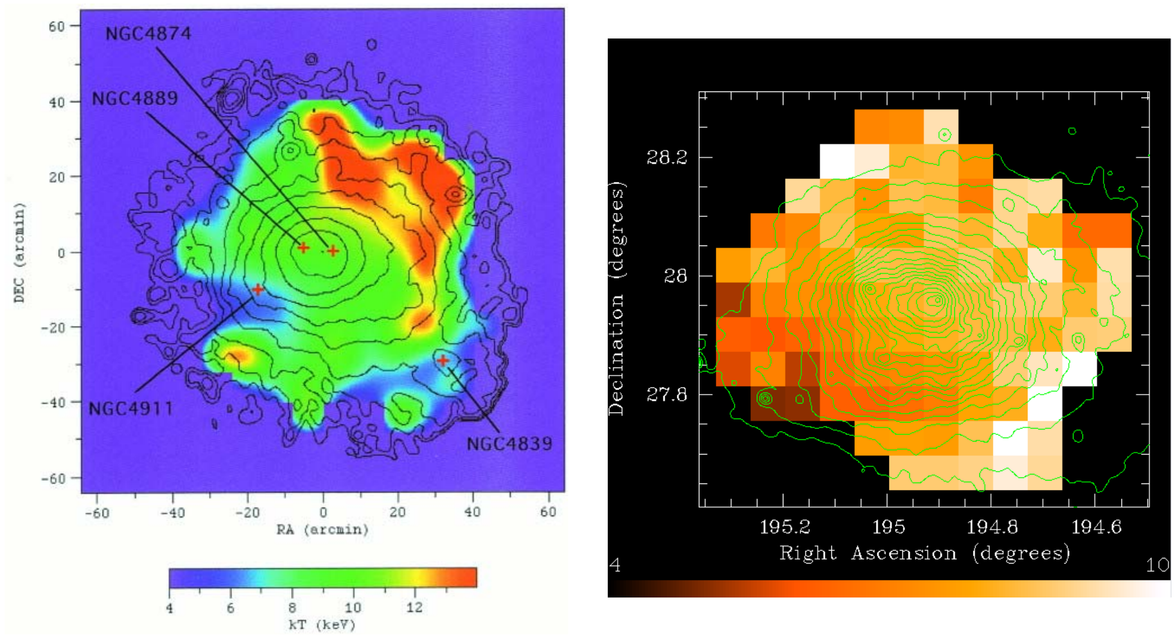

Figure 2.5: Color coded temperature map of the Coma cluster with ASCA (Watanabe et al. 1999) and XMM-Newton (Arnaud et al. 2000).

2.5.4 Metal distribution

The existence and distribution of the chemical elements and their isotopes are a consequence of nuclear processes that have taken place in the past in the Big Bang and subsequently in stars and in the interstellar medium where they are still ongoing. These processes have been studied theoretically and observationally. Based on the optical study, the element and star formation history of the universe is derived as shown in figure 2.7

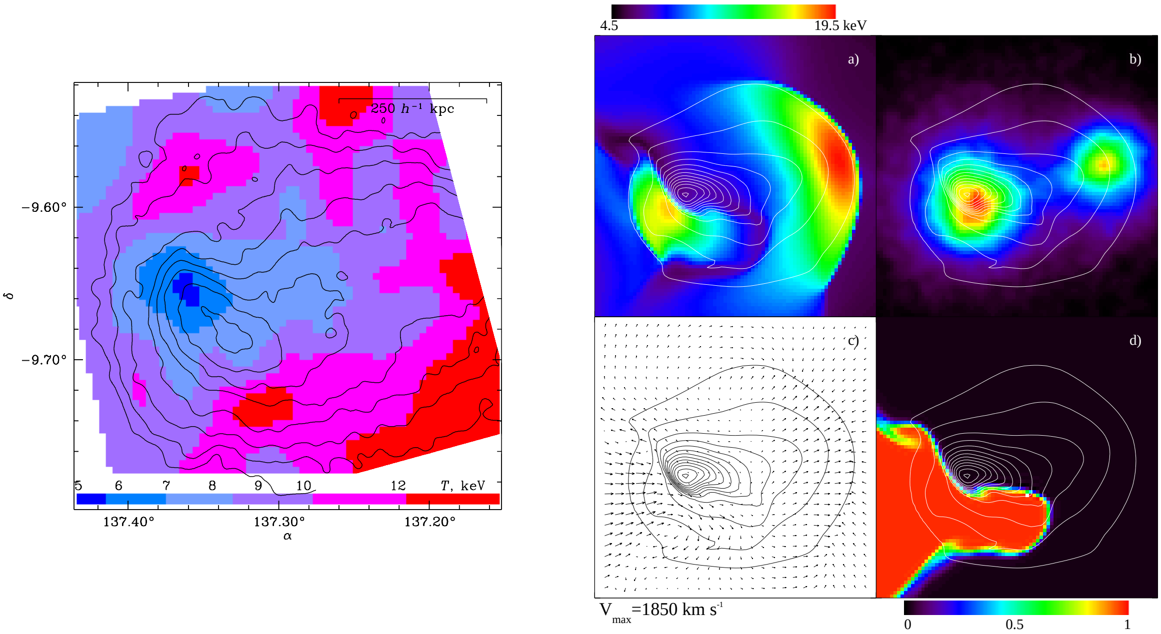

Figure 2.6: A754 temperature map with CXO (Markevitch et al. 2000) and simulation (Roettiger et al. 1998).

(Madau 1999). The results appear the existence of a decline in the universal metal production rate at the redshift $z < 1$ irrespective of being uncorrected or corrected for dust extinction.

The main source of metal production is supernovae (SN), which are classified roughly into Type Ia and Type II. Type Ia SN are important contributers to iron-group elements in the galaxy. Type II SN are explosions of massive stars, which have short lives of about 10 Myr with initial mass above about 10 $M_{\odot}$. Type II SN produce mainly α elements such as O, Ne, Mg, Si, and S. The metal abundances for the elements are given by X-ray spectroscopy of the ICM. Since part of metals are transfered into the ICM by galactic wind or ram pressure stripping, observation of the ICM, not galaxy only, gives total abundance. The observed ratio of Fe to α elements constrains the ratio of Type Ia to Type II and the explosion rate. This enables us to study other essential subjects such as the initial mass function, and star formation rate based on z-evolution.

Since heavy elements can be produced only by thermonuclear reactions in stars and supernovae, the presence of the emission lines found in the spectra from the ICM implies that heavy elements processed in galaxies largely contaminate the ICM.

Koyama et al. (1991) discovered Fe abundance increases at the center of the Virgo cluster with Ginga. From the ASCA observation, similar central abundance increases were found in several clusters (Fukazawa et al. 1994; David et al. 1996; Xu et al. 1997; Kikuchi et al. 1999).

Moreover, recent observational studies of the clusters with *Chandra* and *XMM-Newton* unveil a lot of new interesting abundance distribution in the cluster. Figure 2.8 shows the steep metallicity concentration and the two high-metallicity blobs located symmetrically with respect to the center of the poor cluster AWM 7 (furusho et al. 2003). Even Abell 1060 cluster which has been regarded as one of the most uniform cluster shows the blob like metallisity excess in the extended region located at $\sim 1'.5$ north-east of central galaxy NGC 3311 (figure 2.9), discovered by our *XMM-Newton* observation.

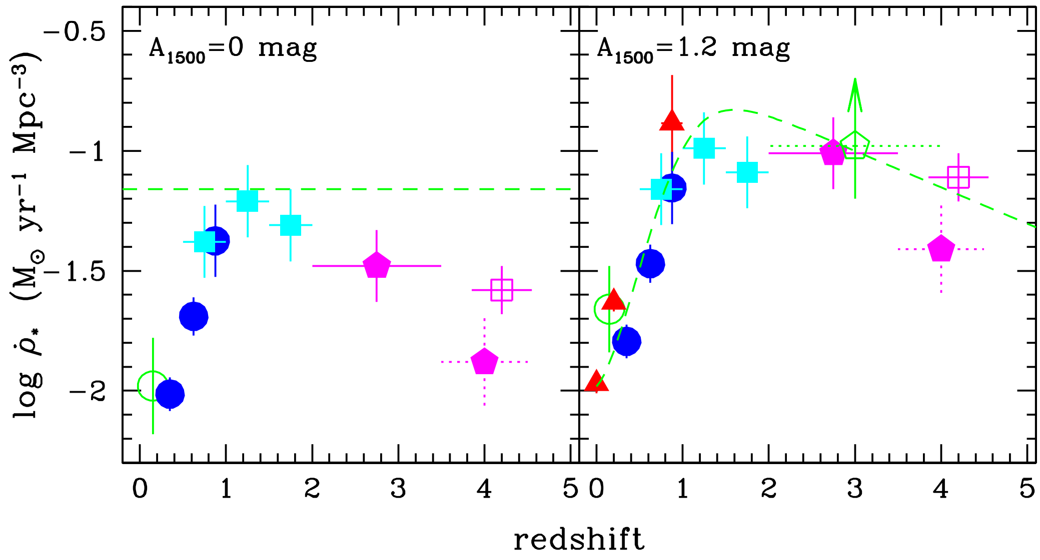

Figure 2.7: *left:* Mean comoving density of star formation as a function of cosmic time. The data points with error bars have been inferred from the UV-continuum luminosity densities. The dotted line shows the fiducial rate, $<\dot{\rho}_{*}>= 0.054 M_{\odot}\ \mathrm{yr}^{-1}\ \mathrm{Mpc}^{-3}$, required to generate the observed extragalactic background light. *right:* dust corrected values ($A_{1500} = 1.2$ mag). The Hα determinations (filled triangles) together with the SCUBA lower limit (empty pentagon) have been added for comparison (Madau 1999).

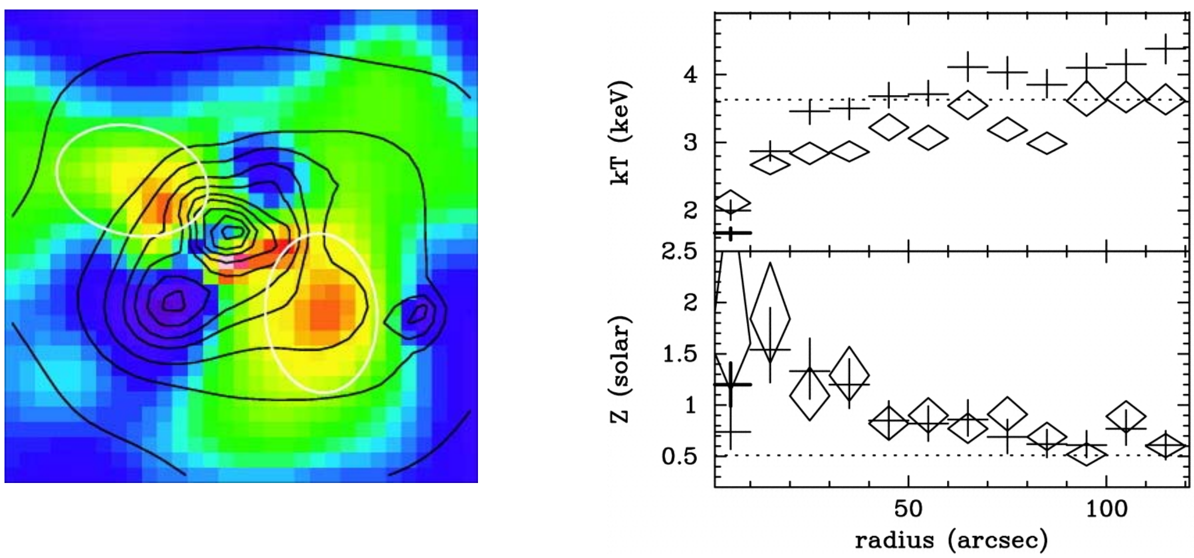

Figure 2.8: Left: The 6-7 keV image of the central 1′ squara region of the AWM 7 cluster with the 2-10 keV intensity contours (furusho et al. 2003 with *Chandra*). The white ellipses indicate the Fe blob region to extract a spectrum analysis. Right: The radial temperature (top) and abundance (bottom) distribution of AWM 7. The crosses and diamonds show the results of 1-9 keV and 2-9 keV band fits.

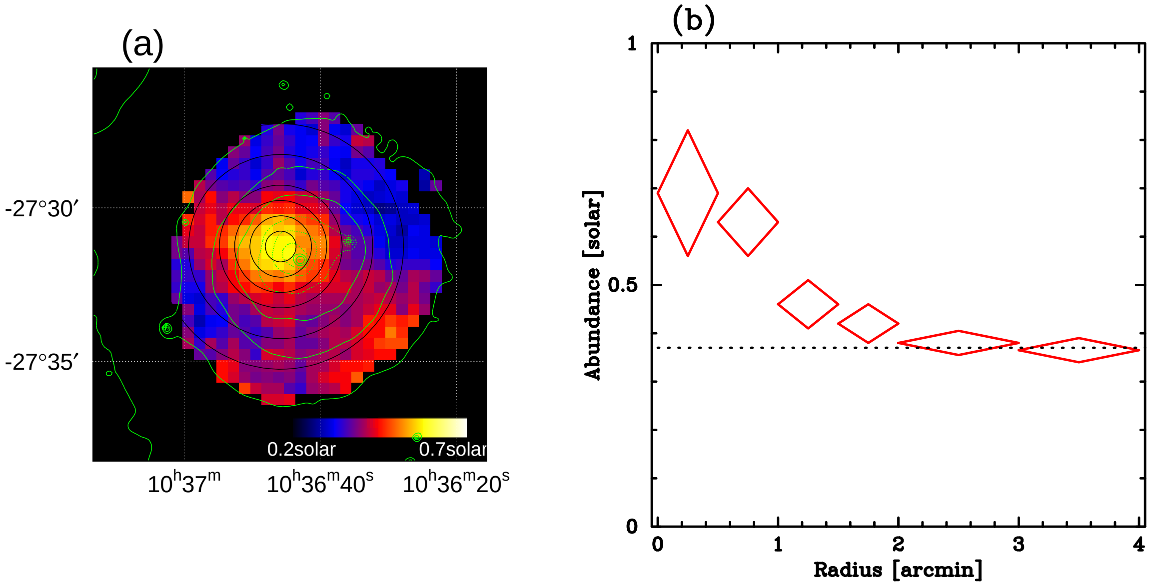

Figure 2.9: (a) Metal abundance distribution in the central $r < 5'$ region of the Abell 1060 cluster with *XMM-Newton* based on spectral analysis. The pixel size is $22'' \times 22''$ (5kpc across). Spectral analysis is carried out for a square region of 3×3 pixels. The overlaid contours show smoothed X-ray surface brightness. (b) Radial metallicity distribution in annuli centered on the position of the high metallicity blob, according to the concentric annuli of (a). The crosses show the projected metallicity distribution.

Chapter 3

Instrumentation

3.1 XMM-Newton

The ESA (European Space Agency) X-ray satellite *XMM-Newton* was launched on 10 December 1999 from Kourou (French Guiana), by the Ariane-V rocket (Jansen et al. 2001). It was placed into a highly eccentric orbit, with an apogee of about 115,000 km, a perigee of about 6,000 km, and an orbital inclination of 33°, which provides the best visibility in the southern celestial sky. Although the orbital period is 48 hours, the exposure available for scientific data analysis is limited to 39 hours (140 ksec) per orbit. This is because observations are not carried out when the satellite altitude is less than 46,000 km, where the radiation background related to the Earth's magnetosphere is severe. *XMM-Newton* provides the following three types of science instrument.

- European Photon Imaging Camera (EPIC)
- Reflection Grating Spectrometer (RGS)
- Optical Monitor (OM)

The three EPIC cameras; the two different types of CCD camera, MOS and pn, and the two detectors of the RGS spectrometers reside in the focal planes of the X-ray telescopes, while the OM has its own telescope. A sketch of the *XMM-Newton* payload is displayed in Fig.3.1.

There are in total six science instruments on board *XMM-Newton*, which are operated simultaneously. The instruments can be operated independently and each in different modes of data acquisition.

In the following sections, we describe the X-ray telescopes and EPIC cameras, because we mainly use these instruments in our study. We summarize the basic performance of the EPIC cameras in table 3.1.

3.2 X-ray Telescopes

3.2.1 Design Structure

XMM-Newton's three XRTs are co-aligned with an accuracy of better than about 1 arcmin. Each of the three telescopes consists of 58 Wolter type-I mirrors, and the mirror grazing incidence angles range between 17 and 42 arcmin. The focal length is 7.5 m and the diameter of the largest mirrors is 70 cm. One telescope with the PN camera at the focal point has a light path as shown in Figure 3.2. The two others have grating assemblies in

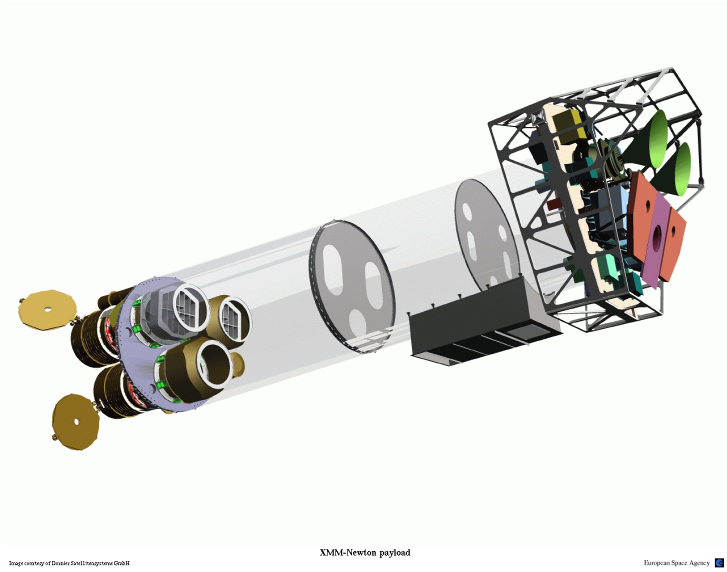

Figure 3.1: Sketch of the *XMM-Newton* payload. The mirror modules, two of which are equipped with Reflection Grating Arrays, are visible at the lower left. At the right end of the assembly, the focal X-ray instruments are shown: The EPIC MOS cameras with their radiators (black/green horns), the radiator of the EPIC pn camera (violet) and those of the (light blue) RGS detectors (in pink). The OM telescope is obscured by the lower mirror module.

Table 3.1: Basic performance of the EPIC detectors

	EPIC-MOS	EPIC-pn
Illumination method	Front illuminated	Back illuminated
Pixel size	40 μm	150 μm
	$1.1''$	$4.1''$
Field of view (FOV)	$30'$	$30'$
PSF (FWHM/HEW)	$5''/14''$	$6''/15''$
Spectral resolution	$\sim$70 eV	$\sim$80 eV
Timing resolution	1.5 ms	0.03 ms
Bandpass	0.15-12keV	0.15-15keV

their light paths, diffracting part of the incoming radiation onto their secondary focus (see Figure 3.3). About 44 % of the incoming light focused by the XRT is directed onto the MOS camera at the prime focus, while 40 % of the radiation is dispersed by a grating array onto a linear strip of CCDs. The remaining light is absorbed by the support structures of the RGAs.

3.2.2 Point-spread function (PSF) of XRTs

A point-spread function (PSF) determines the imaging quality of an XRT. Figure 3.4 shows the in orbit on-axis images obtained by each detector. The radial substructures are caused by the spiders holding the mirror shells. Figure 3.5 displays the azimuthally averaged profile of the PSF of one XRT together with the best-fit King profile, which has the form $A(1/[\{1 + (r/r_c)^2\}^{\alpha}])$, where r is the radial distance from the center of

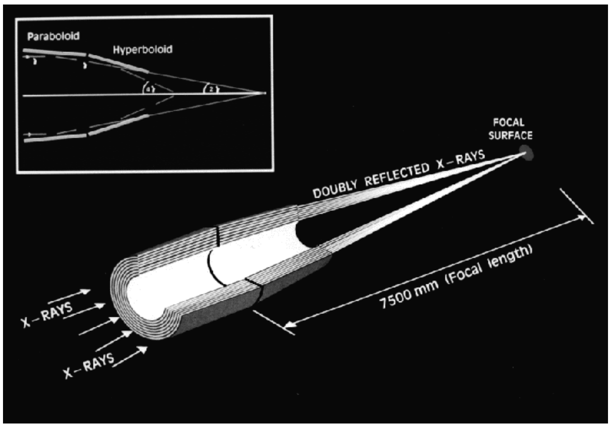

Figure 3.2: The light path in *XMM-Newton*'s XRT with the PN camera in focus.

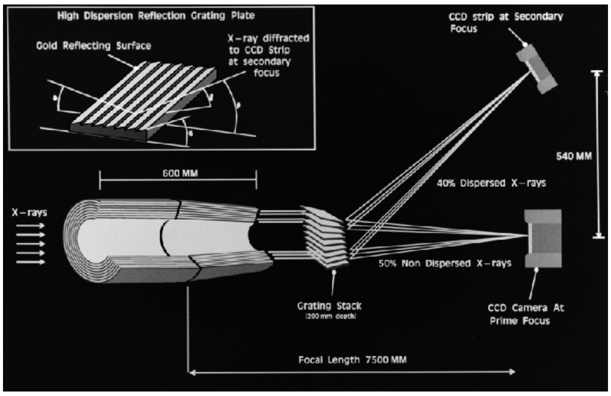

Figure 3.3: The light path in *XMM-Newton*'s XRT with the MOS camera and RGA.

the PSF, r_c is the core radius and α is the slope of the King model. Figure 3.6 shows the encircled energy function (EEF) as a function of radius from the center of the PSF for several different energies. For on-axis source, high energy photons are reflected and focused predominantly by the inner shells of the XRTs. The inner shells apparently give better focus than the average of all shells, hence the EEF increase with increasing photon energy. A half energy width (HEW), which means the width including half of all the reflected photons, of the PSF can be derived from EEF. Table 3.2 lists the on-axis HEW of the different XRTs measured in orbit and on ground.

The PSFs of the XRTs depend on the source off-axis angle. As the off-axis angle increases, the HEW of PSF becomes larger.

Table 3.2: The on-axis in orbit and on ground 1.5 keV HEW of the different XRT.

Instr.	PN	MOS1	MOS2
	orbit/ground	orbit/ground	orbit/ground
HEW [arcsec]	15.2/15.1	13.8/13.6	13.0/12.8

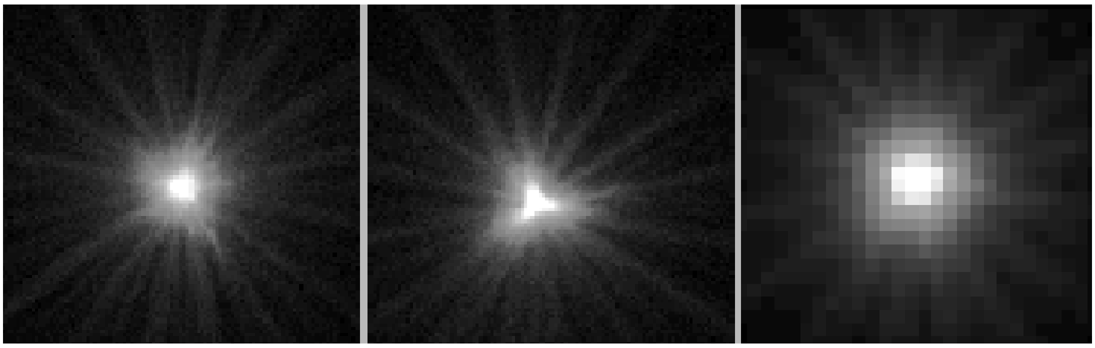

Figure 3.4: On-axis images of the MOS1, MOS2 and PN XRTs (left to right). The images are 110 arcsec wide and a logarithmic scale has been used to visualize the wings of the point spread function.

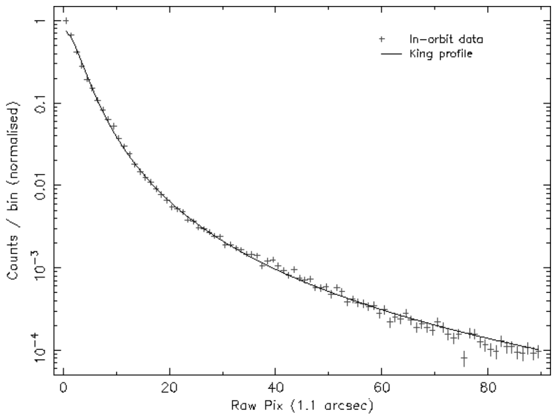

Figure 3.5: Radial counts distribution for the on-axis PSF of the MOS1 XRT in the 0.75–2.25 keV energy range. The solid line indicates the best-fit King profile.

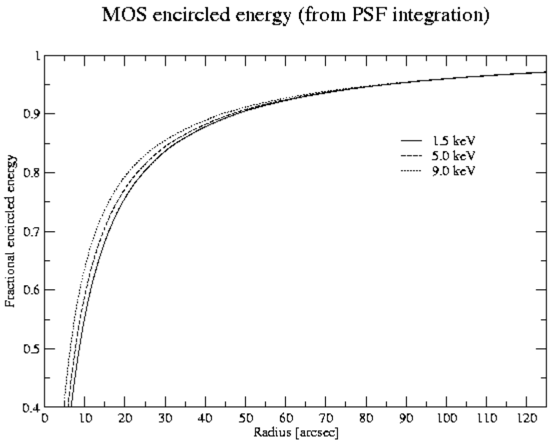

Figure 3.6: The encircled energy function as a function of angular radius (on-axis) at different energies. The curves are calculated assuming a fractional encircled energy of 100 % at a radial distance of 5 arcmin.

3.2.3 Effective Area (EA) of XRTs

An effective area is an indicator of ability of collecting photons. *XMM-Newton* carries the XRT with the largest effective area of focusing telescope ever. The total mirror geometric effective area (EA) at 1.5 keV energy is about 1,550 cm^2 for each telescope, i.e., 4,650 cm^2 in total. Figure 3.7 shows the on-axis effective area of all *XMM-Newton* XRTs. The EAs of the two MOS cameras are lower than that of the pn, because only part of the incoming radiation falls onto these detectors, which are partially obscured by the RGAs (see Figure 3.3). Not only the shape of the X-ray PSF, but also the effective area of the XRT is a function of off-axis angle within the field of view. Decreasing of photons reflected effectively in the XRT arises from an increasing off-axis angle. This effect is called vignetting. Figure 3.8 displays the vignetting function as a function of off-axis angle for several different energies. The vertical axis is normalized by the on-axis effective area.

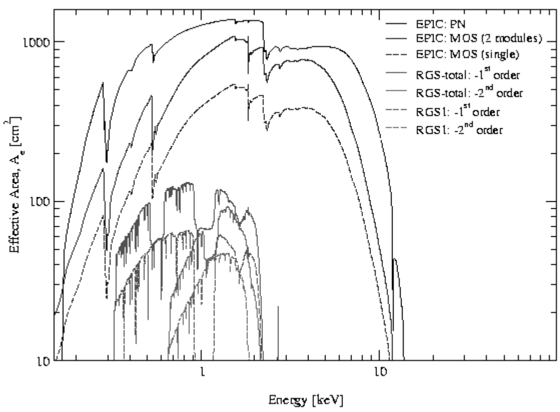

Figure 3.7: The net effective area of all *XMM-Newton* XRT, combined with the response characteristics of the focal detectors.

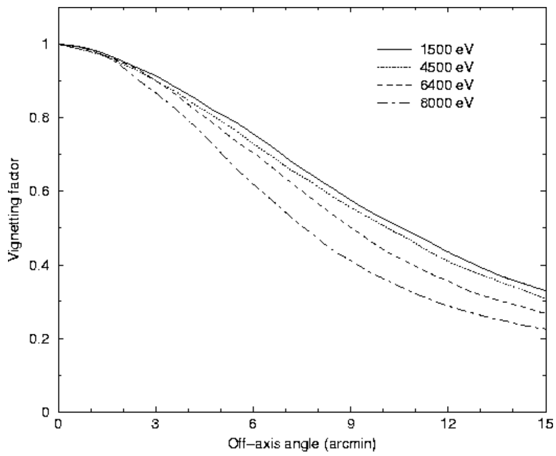

Figure 3.8: Vignetting function as a function of off-axis angle at several different energies (based on simulations).

3.2.4 Straylight Rejection

X-ray straylight is produced by rays which are singly reflected by the mirror hyperbolas and which reach the sensitive area of the focal plain detectors. Thus, an X-ray baffle was implemented to shadow those singly reflected rays. It consists of two sieve plates made of concentric annular aperture stops located in front of the mirrors at 85 mm and 145 mm, respectively. The design is such that the entrance annular aperture of each mirror remains unobstructed for on-axis rays. The collecting area of straylight in the EPIC detector as a function of off-axis angle for a point source is about 3 cm^2 for stray sources located between 20 arcmin and 1.4° from the optical axis. The ratio of the X-ray straylight collecting area to the on-axis effective area is smaller than 0.2 % at 1.5 keV for a point source located at off-axis angles of 0.4–1.4° and negligible at higher off-axis angles. Figure 3.9 displays the effect of straylight, which is obtained from the observation of GRS 1758-258 (a black hole candidate near the Galactic center). Some sharp arcs are caused by single mirror reflections of photons possibly from GX 5-1 which is located at off-axis angle of 40 arcmin to the north and outside the field of view.

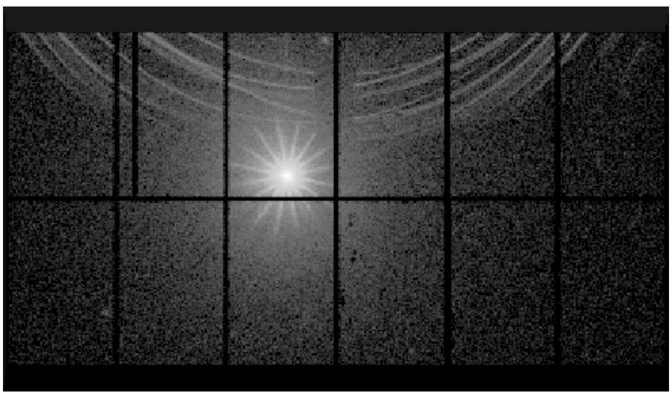

Figure 3.9: The effect of straylight appeared in PN image of GRS 1758-258.

3.3 European Photon Imaging Camera (EPIC)

Two of *XMM-Newton*'s X-ray telescopes are equipped with EPIC MOS (Metal Oxide Semi-conductor, Turner et al. 2001) CCD arrays, the third carries a different CCD camera called EPIC PN (Strüder et al. 2001). The EPIC cameras offer the possibility to perform extremely sensitive imaging observations over a field of view of 30 arcmin and the energy range from 0.15 to 15 keV, with moderate spectral ($E/\Delta E \sim$ 20–50) and angular resolution (15 arcsec HEW). The detector layout and the baffled X-ray telescope FOV of both types of EPIC cameras are shown in Figure 3.10. The PN chip array is slightly offset with respect to the optical axis of its X-ray telescope so that the nominal, on-axis observing position does not fall on the central chip boundary. This ensures that more than 90 % of the energy of an on-axis point source are collected on one PN CCD chip. Two EPIC MOS cameras are rotated by 90° with respect to each other. The dead spaces between the MOS chips are not gaps, but unusable areas due to detector edges (the MOS chip physically overlap each other, the central one being located slightly behind the ones in the outer ring). All EPIC cameras are operated in photon counting mode with a fixed, mode dependent frame read-out frequency.

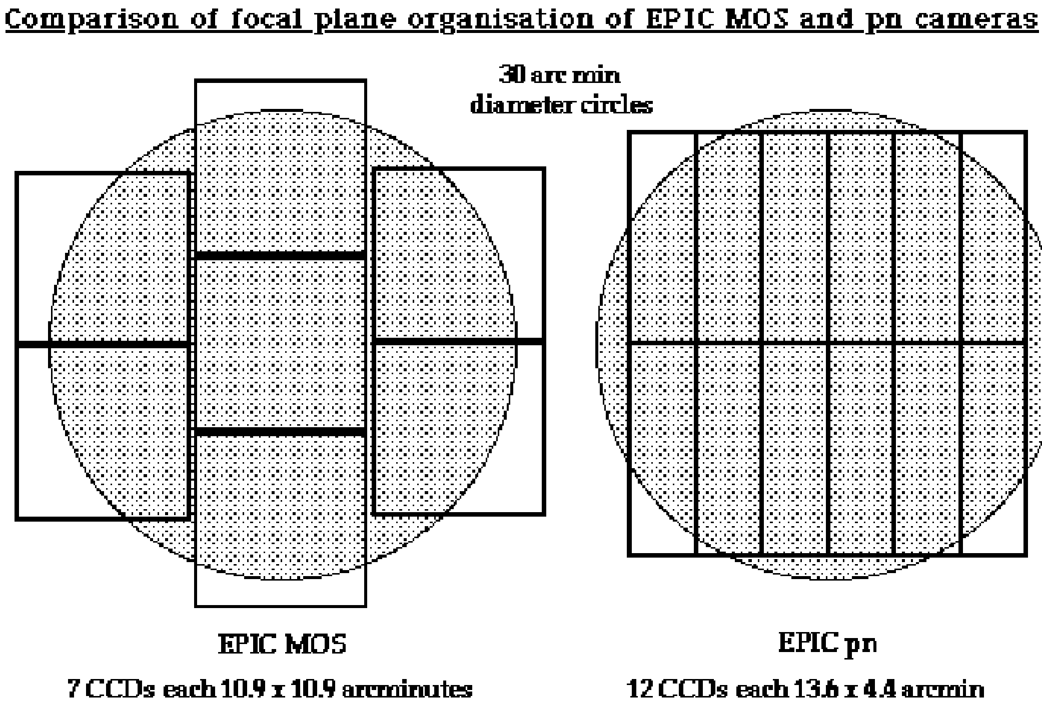

Figure 3.10: A rough sketch of the field of view of the two types of EPIC cameras (MOS, left; PN, right). The shaded circle depicts a 30 arcmin diameter area which is equivalent with the XRT field of view.

3.3.1 Basic properties

Angular resolution

The EPIC MOS and PN cameras have pixels with sizes of 40 and 150 μm, respectively. For the focal length of the X-ray telescopes (7.5 m), these pexel size corresponds to 1.1 arcsec and 4.1 arcsec on the sky. Since they are smaller than the HEW of XRT (15 arcsec), EPIC's angular resolution is basically determined by the PSF of the mirror modules.

Energy resolution

The resolving power of EPIC cameras is determined by the intrinsic energy resolution of the individual pixels. Figure 3.11 and 3.12 show the energy resolution (FWHM) of MOS and PN, respectively. The measured in-flight FWHM of the Al Kα (1.5 keV) and Mn Kα (5.9 keV), which are the on-board calibration lines, are also plotted in Figure 3.11. It is well known that the energy resolution of MOS cameras has been gradually decrease due to the CTI (charge transfer inefficiency) effect, which means the imperfect transfer of charge as it is transported through the CCD to the output amplifiers. The latest calibration status is found at *XMM-Newton* Science Operation Centre.[1] The accuracy of the energy determination is about 10 eV over the full energy range and for all modes except for MOS timing mode.

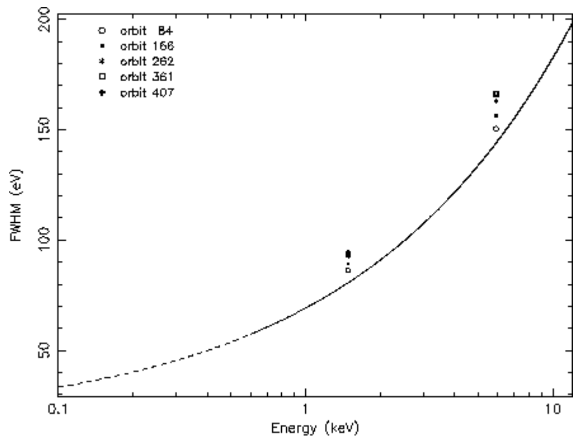

Figure 3.11: The EPIC MOS energy resolution (FWHM) as a function of energy. The solid curve is a best-fit $E^{0.5}$ function to ground calibration data between 0.1–12.0 keV. Below around 0.6 keV (shown by the dotted region), surface charge loss effects distort the main photopeak significantly from a Gaussian form and, hence the effective energy resolution. The measured in-flight FWHM of the Al Kα (1.487 keV) and Mn Kα (5.893 keV) lines are also plotted.

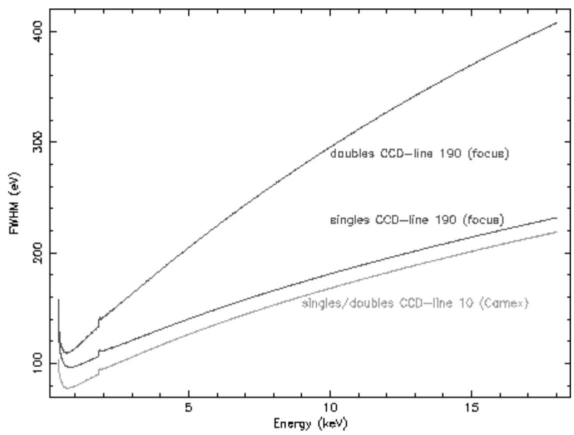

Figure 3.12: The EPIC PN energy resolution (FWHM) as a function of energy. Curves are given for single and double events (full frame mode) at the focus position as well as at a position 10 pixels away from the readout node.

Quantum efficiencies

The quantum efficiency of both types of EPIC CCD chips as a function of photon energy is displayed in Figure 3.13 and 3.14. These chips were calibrated using laboratory X-ray beams, synchrotron generated monochromatic X-ray beams, before launch, and celestial X-ray source measurements. We can see the typical X-ray absorption fine structure

[1] *http://xmm.vilspa.esa.es/external/xmm_sw_cal/calib/documentation.shtml#EPIC*

(XAFS) behavior around the silicon K edge at 1.838 keV. Ground calibration measurements have shown that the quantum efficiency of MOS CCDs is uniform above 400 eV. Below this energy, spatial variations are seen as patches in the outer parts of the CCDs where the response is degraded. This inhomogeneity is currently not taken into account by the *XMM-Newton* science analysis system (SAS).

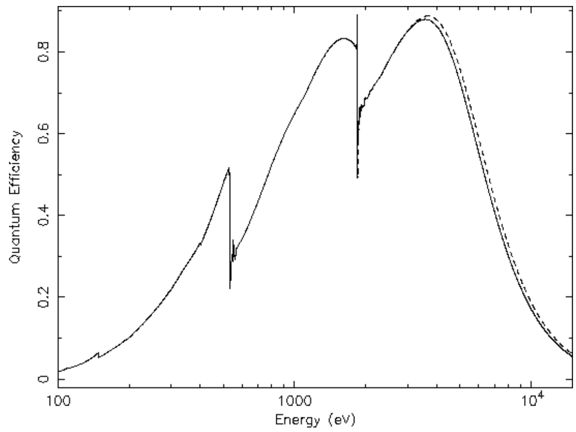

Figure 3.13: Quantum efficiency of the EPIC MOS camera as a function of photon energy.

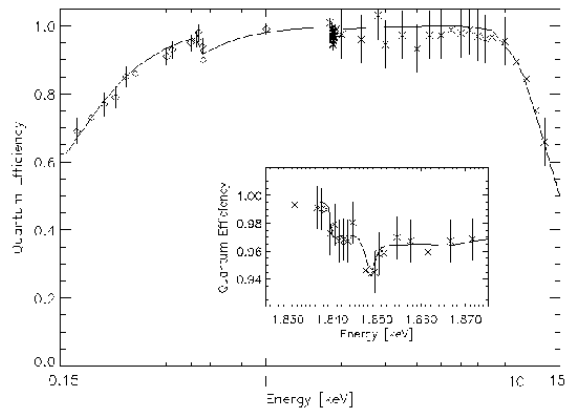

Figure 3.14: Quantum efficiency of the EPIC PN camera as a function of photon energy.

EPIC Filters

The EPIC CCDs are not only sensitive to X-ray photons, but also to IR, visible and UV light. Therefore, if an astronomical target has a high optical to X-ray flux ratio, there is a possibility that the X-ray signal becomes contaminated by those photons. To prevent such a contribution, each EPIC camera is equipped with a set of 3 separate aluminised optical blocking filters, named *thick*, *medium* and *thin*. The thick filter should be used for all point source targets up to m_V of 1–4 (MOS) or 0–3 (PN). The medium filter is about 10^3 less efficient than the thick filter, therefore, it is useful for preventing optical contamination from point sources as bright as m_V = 8–10. The thin filter is about 10^5 less efficient than the thick filter, so the use of this filter will be limited to point sources with optical magnitudes about 14 magnitudes fainter than the corresponding thick filter limitations.

Event pattern

An absorbed sometimes deposits its energy over more than one pixels. This is called split event, and in this case the charges mus be summed up over the relevent pixels. This process is automatically done by analysis software. The split pattern is classified in Figure 3.15. The patterns 0-12 for MOS and 0-4 for pn are considered to be X-ray events, while the others are false events induced by charged particles. Because of its much larger pixel size than MOS, the charge split occurs less frequently in pn (Turner et al. 2001).

Any events which located at around an edge or bad pixel are flagged by negative value. These events have possibility that the energy of these events are not correct. If we make a condition that the events have flag=0, we remove the events which are rocated around the edge ore bad pixel.

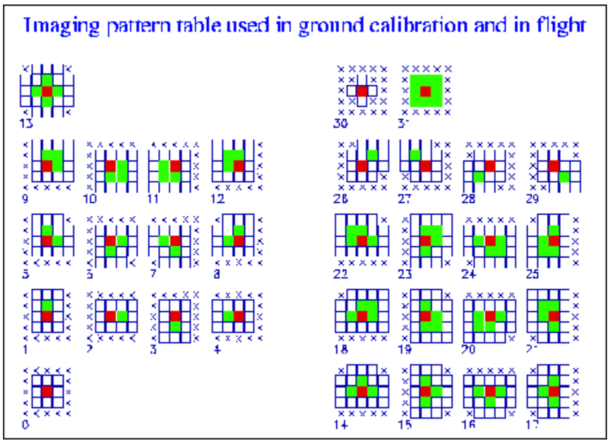

Figure 3.15: Event patterns recognized by the MOS (pn) detectore. The red pixel is the centre pixel, its signal is above threshold and is the largest signal in the 3×3 inner matrix. The green pixels have signals above threshold. The white pixels have signal below threshold. The crosses indicate pixels no considered.

3.4 EPIC Background

The EPIC background can be divided into two parts: a cosmic X-ray background (CXB), and an instrumental background. The latter component may be further divided into a detector noise component, which becomes important at low energies (i.e. below 200eV) and a second component which is due to the particles interaction. This component is characterized by a flat spectrum and is particularly important at high energies (i.e. above a few keV).

The particle induced background can be divided into two components: an external 'flaring' component, characterized by strong and rapid variability, which is often totally absent and a second more stable internal component. The flaring component is currently attributed to soft protons, which are presumably funneled towards the detectors by the X-ray mirrors. The stable component is due to the interaction of high-energy particles with the structure surrounding the detectors and possibly the detectors themselves. We summarize the all background component below.

Back Ground

- Cosmic X-ray Background
- Instrumental Background
  - Detector noise component (below 200eV)
  - Particle component (above a few keV)
    - flaring component (attributed soft photons)
    - stable component (attributed high-energy particles)

In the following we describe some of the main properties of both components.

3.4.1 Temporal properties

As shown in Figure 3.16, the EPIC background count rate often exhibits sudden increases by as large as two orders of magnitudes, called 'flares'. Such phenomena are not observed in the *ASCA* SIS. This is mainly due to the difference in their orbits. *ASCA* had an almost circular orbit with an altitude of 520-620 km, while XMM-Newton take highly eccentric orbits, with apogees of $\sim 115,000$ km and perigees of $\sim 6,000$ km. Therefore, XMM-Newton fly mostly outside the Earth's magneto-sphere. Now it is known that the background flares are caused by soft protons with energies below 1 MeV, reflected and focused by the X-ray mirrors. The spectra of soft proton flares are variable and no clear correlation is found between intensity and spectral shape. The current understanding is that soft protons are most likely organized in clouds populating the Earth's magneto-sphere. The number of such clouds encountered by XMM-Newton in its orbit depends upon many factors, such as the altitude of the satellite, its position with respect to the magneto-sphere, and the amount of solar activity.

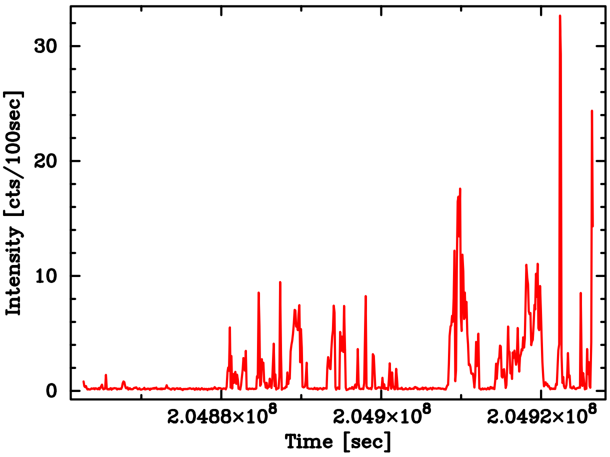

Figure 3.16: An example of light Curve from a MOS1 observation badly affected by proton flares.

The EPIC background events in quiescent (non-flaring) periods are produced mainly by the interaction of high energy particles with the structure surrounding the detectors, and the detectors themselves. This component varies only by a small fraction, and on relatively longer timescales. On a representative time scale of several tens ksec, the standard deviation of both PN and MOS count rates is about 8 % (Katayama et al. 2004; Pizzolato 2001; Read & Ponman 2003).

3.4.2 Spectral properties

In Figure 3.17, we show the MOS1 and PN spectra extracted from a blank sky region. These background spectra consist of non X-ray background (NXB) and cosmic X-ray background (CXB). The NXB is induced mainly by charged particles. The CXB is mainly dominates at lower energies by soft thermal emission around the solar system. The entire background spectra are dominated by the NXB at high energy regions, and the CXB becomes more important as the energy decreases. Their contributions are comparable at the energy of ~ 1 keV.

Fig. 3.17 shows several distinct fluorescence lines. In PN spectra, Al-K, Ni, Cu, and Zn-K complex lines are prominent, while Al and Si-K lines are outstanding in the MOS.

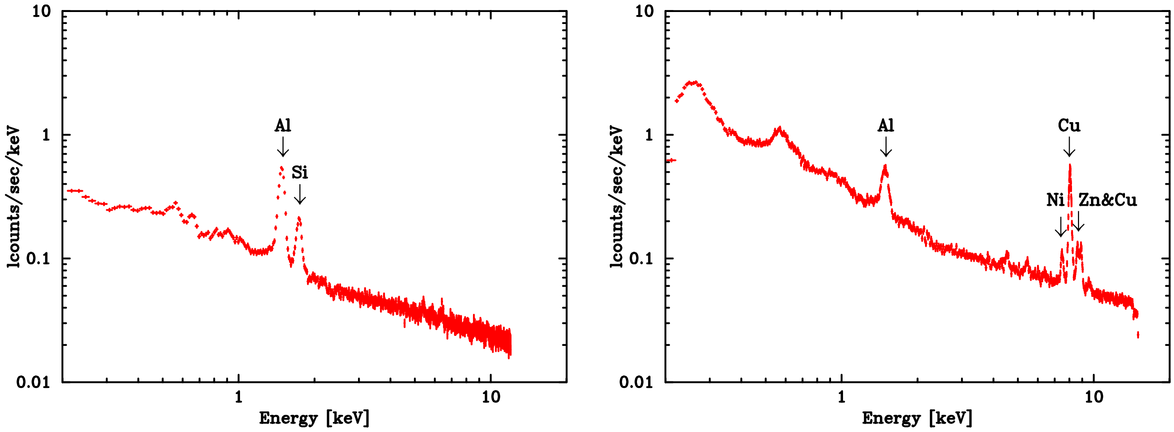

Figure 3.17: MOS1(left) and PN(right) background spectrum from a blank sky region. In the left figure, the prominent features around 1.5 and 1.7 keV are Al K and Si K fluorescence lines, respectively. On the other hands, he prominent features, in right figure, are identified as Al-K (1.5 keV), Cr-K (5.5 keV), Ni-K, Cu-K, Zn-K (8.0 keV) and Mo-K (17.5 keV), respectively.

These lines are emitted from surrounding materials such as electronic circuit boards for the signal readout, excited by high energy charged particles. Both the PN and MOS spectra rise below $\sim$ 0.5 keV, due to the detector noise which is more time variable than the continuum above 0.5keV.

3.4.3 Spatial properties

Because the CXB surface brightness is highly uniform, its brightness distribution on the focal plane obeys the effective area. Due to the vignetting effect, the CXB brightness is highest at the detector center, and gradually decreases toward the periphery.

The distribution of the Si-K line in the MOS is concentrated along the edges of some CCDs. This is attributed to Si-K X-rays escaping from the back side of a neighboring CCD. The asymmetric distribution arises because the 7 CCD chips slightly overlap with one another when viewed from the telescope, although their 3-dimensional positions are offset along the optical axis. This layout is intended to reduce the gaps between CCD chips.

Spatial distributions of emission lines are rather complicated. Figure 3.18 show some background images in limited energy bands. The emission in the Cu-K band is very weak at the center of PN (fig. 3.18 right). Actually, the Cu-K line is insignificant in the spectrum extracted there. The Cu-K line image with the central hole agrees with the layout of electronics boards beneath the PN CCDs, indicating that the Cu-K photons come from them. The same mechanism produces semicircular dark regions at the right and reft sides.

The continuum components of the NXB also have inhomogeneous distribution on the focal plane. The NXB image shows central excess brightness, by about 25 %. The shape is similar to the central hole seen in the Cu-K band image (fig. 3.18), although in this case the brightness shows excess, not a deficit.

As is implied by these non-uniform distributions of various components, the background spectrum strongly depends on the detector position. Therefore, when we use other observations as the background fields, we must extract the background spectrum from the same detector region as the analyzing target.

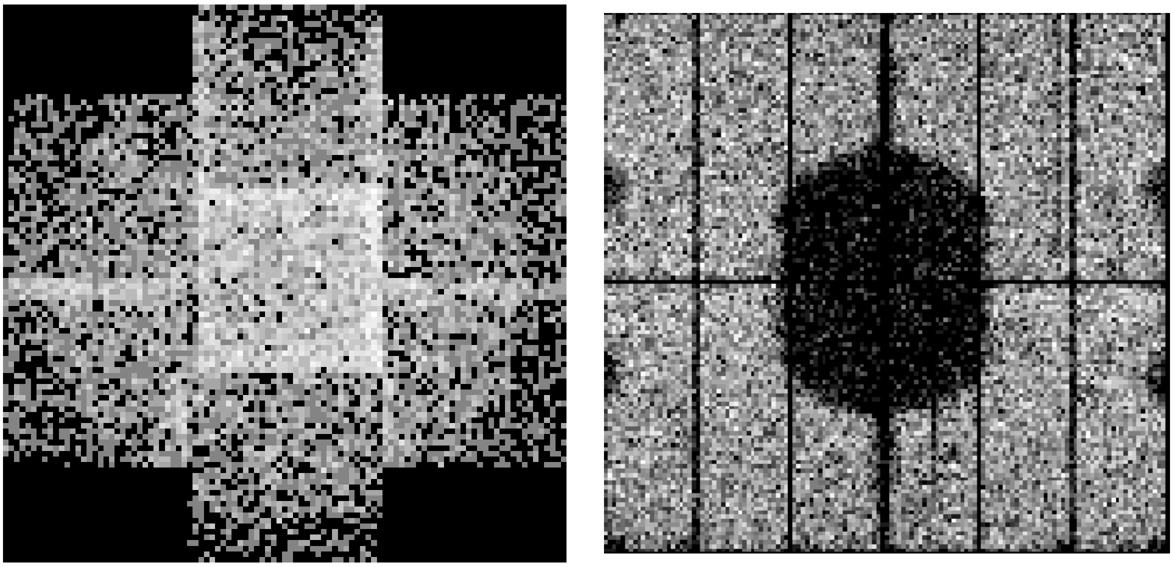

Figure 3.18: The MOS(left) and PN(right) background image. The MOS image in the energy band centered on Si-K fluorescent line region. As the same, the PN image in the Cu-K fluorescent line energy region.

Chapter 4

Observation and Data Reduction

4.1 Target Selection

As discussed in §1, the purpose of this thesis is to study the difference in the mass distribution of the cD and non-cD clusters. Accordingly, we use *XMM-Newton* observatory, which has excellent imaging capability, large effective area and large FOV, to carry out the high-resolutional X-ray imaging analysis and high-quality imaging spectroscopy after subtract the point-like sources. Until the present, a lot of scientist study the cD clusters. However, there are no study that pay attention to the non-cD cluster samples. Therefore, at the first time we select the non-cD clusters on the following criteria.

1. We select the clusters of galaxies in the XMM-Newton archived targets list. There are ~ 130 clusters in all.

2. In order to carry out the detailed study into the the cluster central region, we surveyed all nearby clusters.

3. Since we measure the temperature and the surface brightness profile based on the assumption that the cluster is spherically symmetric to obtain the density and the gravitational mass profile, we need to select relaxed and nearly spherically symmetric clusters. We exclude the clusters which show the merging evidence and obviously irregular clusters.

4. For detailed study, we need enough amount of photons. We thus selected the clusters with observed photons more than 20,000 per each MOS detectors.

5. From the remaining samples, we first select the non-cD type clusters based on the Bautz-Morgan (BM) cluster classification type. We summarize the BM classification type in table 4.1.

Table 4.1: Bautz-Morgan clsuter classification

B-M type	description
I	dominated by a single, central cD galaxy.
II	the brightest galaxies are intermediate between cD and normal giant ellipticals.
III	no dominanting cluster galaxies.

Through these criteria, we have obtained 15 non-cD clusters (we classified MKW 9 as type III based on the classification in Bahcall & Soneira (1980)). This is the complete sample of the spherically symmetric clusters in the region $z \leq 0.2$ from the *XMM-Newton* archival database.

Next, we select the cD clusters, in order to compare the non-cD cluster samples. After the same way of the previous selection procedures from 1 to 4, we select the seven poor cD clusters which features (redshift, ICM temperature, and so on.) is close to the selected non-cD clusters. We note that the cD cluster samples are not complete sample. In addition, to study the gas distribution at the outer region, we add a few high redshift spherically symmetric clusters, RXJ1347-1145 ($z = 0.4510$) and RXJ2129+0005 ($z = 0.2350$). Since these two clusters show the same feature as cD cluster, we deal with these clusters as the group of cD cluster samples. Through these procedure, we have selected arbitrarily 22 clusters for our analysis, whose basic properties are shown in table 4.2. Table 4.3 shows the observation logs of the sample clusters.

Table 4.2: Cluster Basic Information

Cluster	z	D [Mpc]	$1'$ [kpc]	N_H [$\times10^{20}$ cm^{-2}]	Morphology [BM]	Richness
AWM 7	0.0172	69.1	20.1	9.83	(I)	(0)
AWM 4	0.0318	128.1	35.0	5.00	(I)	(1)
A 2717	0.0490	198.1	52.4	1.11	I-II	1
A 0133	0.0566	225.3	58.8	1.54	(I)	0
A 3112	0.0750	305.2	76.8	2.61	I	2
A 3827	0.0984	402.6	97.1	2.10	I	2
A 1413	0.1427	589.4	131.3	2.19	I	3
RXJ2129+0005	0.2350	988.9	188.6	4.28	-	-
RXJ1347-1145	0.4510	1970.0	272.2	4.85	-	-
A 1060	0.0114	45.7	13.0	4.90	III	1
A 4038	0.0300	120.8	33.1	1.55	III	2
A 0576	0.0389	157.0	42.3	5.71	III	1
MKW 9	0.0397	160.2	43.1	4.18	(II-III)	(1)
A 1983	0.0442	178.6	47.6	2.04	III	1
A 3532	0.0554	224.4	58.6	5.91	II-III	0
A 0278	0.0891	363.8	89.2	5.35	III	0
A 2034	0.1130	463.8	108.9	1.58	II-III	2
A 2051	0.1150	472.2	110.5	5.43	II-III	2
A 2050	0.1183	486.1	113.1	4.71	II-III	1
A 2328	0.1470	607.7	134.4	4.69	III	2
A 1689	0.1832	763.1	158.6	1.82	III	1
A 0209	0.2060	862.0	172.4	1.65	II-III	3

Table 4.3: Cluster sumple and XMM-Newton Observertion logs

Cluster	Position		Obs. date	Rev.	Obs. ID	Exp.[ks]		Mode		Filter	
	RA	DEC				MOS	pn	MOS	pn	MOS	pn
AWM 7	02h54m23.04s	+41D34m01.3s	2003-02-02	0577	0135950301	29/31	13/27	F	F	M	T
AWM 4	16h04m55.77s	23D55m53.70s	2003-01-25	0573	0093060401	17/21	12/15	F	E	M	M
A 2717	00h03m12.89s	-35D56m12.30s	2002-11-26	0558	0145020201	52/53	44/47	F	F	T	T
A 0133	01h02m41.10s	-21D52m47.00s	2002-12-22	0556	0144310101	21/33	16/25	F	E	T	T
A 3112	03h17m56.00s	-44D14m06.0s	2000-12-24	0191	0105660101	23/23	17/17	F	F	M	M
A 3827	22h01m56.00s	-59D56m57.00s	2002-11-16	0538	0149670101	22/24	14/21	F	F	M	M
A 1413	11h55m19.00s	23D24m36.00s	2000-12-06	0182	0112230501	25/26	19/19	F	F	T	M
RXJ2129+0005	21h29m37.90s	00D05m38.40s	2002-10-29	0529	0093030201	37/58	27/33	F	E	M	M
RXJ1347-1145	13h47m31.00s	-11D45m9.00s	2002-07-31	0484	0112960101	33/38	25/49	F	F	T	T
A 1060	0h42m27.42s	-27D31m35s	2004-06-29	0834	0206230101	36/63	25/53	F	F	M	M
A 4038	1h35m11s	-28D8m26.7s	2004-12-08	0916	0204460101	29/29	25/25	F	F	M	M
(klemola44)											
A 0576	0h29m27.28s	55D49m11s	2004-03-27	0787	0205070401	16/20	11/16	F	F	M	M
MKW 9	15h32m29.25s	+04D40m54.3s	2001-08-21	0311	0091140401	30/41	19/33	F	E	T	T
A 1983	14h52m44.00s	16D44m48.00s	2002-02-14	0400	0091140201	26/32	18/25	F	E	T	T
A 3532	12h57m22.00s	-30D22m3.00s	2002-07-03	0470	0030140301	10/17	5/14	F	F	M	M
(klemola22)											
A 0278	1h57m18.0s	+32d13m37s	2004-02-11	0765	0203980101	18/22	18/32	F	E	M	M
A 2034	15h10m13.1s	+33d31m41s	2003-08-01	0667	0149880101	10/25	7/18	F	E	T	T
A 2051	15h16m46.5s	-00d56m59s	2004-08-03	0852	0201902101	30/30	23/23	F	E	T	T
A 2050	15h16m21.6s	+00d05m59s	2004-07-22	0846	0201902001	26/28	21/21	F	E	T	T
A 2328	20h48m13.9s	-17d48m53s	2004-05-13	0811	0201902401	25/26	19/20	F	E	T	T
A 1689	13h11m29.40s	-01D20m29.00s	2001-12-24	0374	0093030101	37/38	29/31	F	E	T	T
A 0209	01h31m57.5s	-13d34m35s	2001-02-28	0328	0084230301	18/22	12/16	F	F	M	M

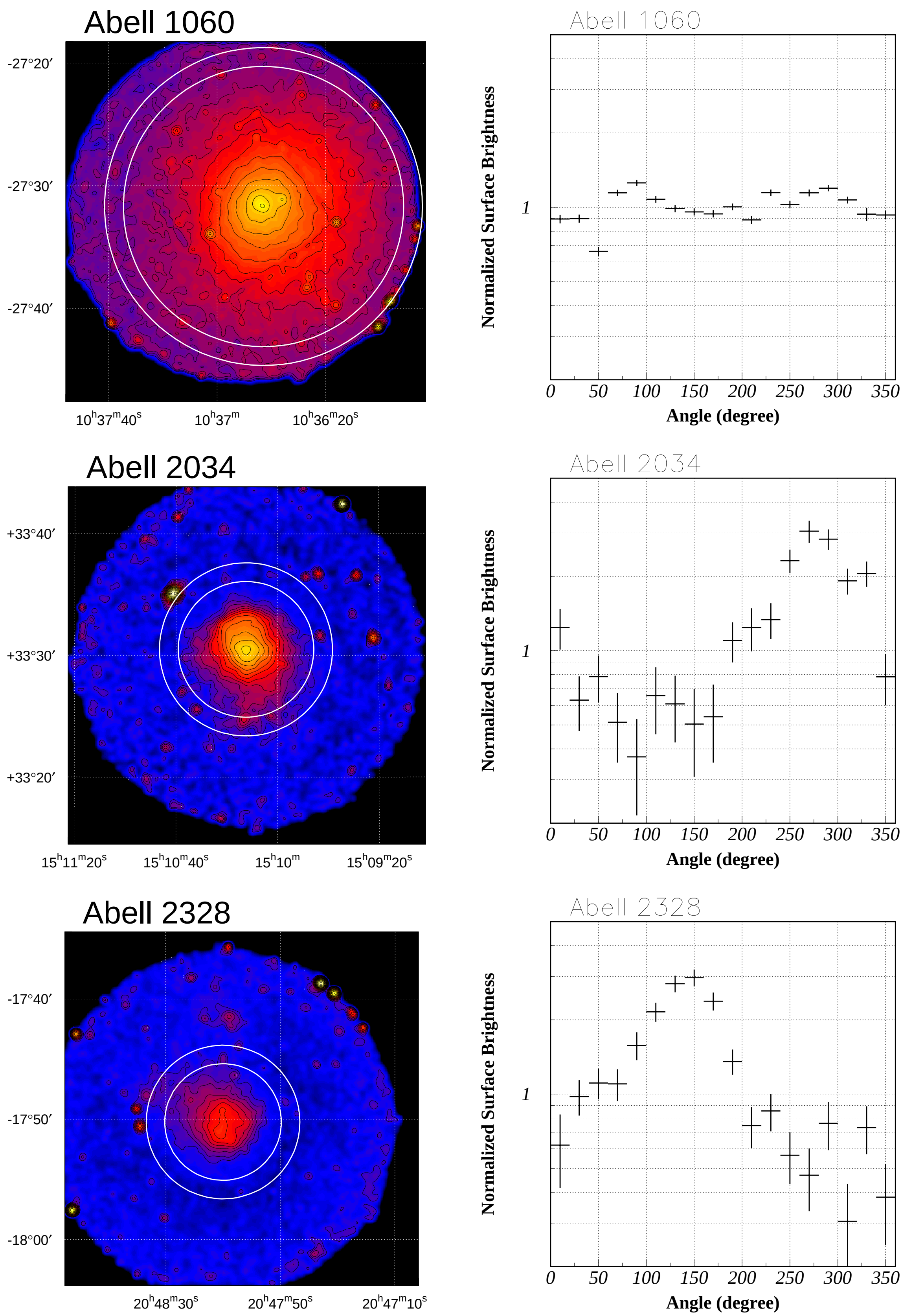

Figure 4.1: The resultant azimuthal intensity distribution (right) and selected annulus (left) of three clusters, A 1060, A 2034 and A 2328. A 2034 adn A 2328 are removed after the selection.

4.1.1 Definition of spherical symmetry

In the previous section, we have selected the cluster samples which satisfied our requests in the *XMM-Newton* archived data list, and then we select the relatively relaxed cluster under the condition that its shape is spherical symmetric. However, we remove the irregular sources based on the quick looking in the present situation. Therefore, we define the cluster circlurity quantitatively, and then we reevaluate the cluster circlurity based on this new evaluation.

We estimate the radial signal to background ratio centered on the luminosity peak of the sample culsters, and pull out the $1.5'$ width annulus around the radius which is consistent to the twice as large as the radial signal to background ratio. In the case of A 1060 and AWM 7 clusters, we use the most outer radius ($\sim 14'$) which we can selected, since the radius that signal to background ratio doubles become out of FOV. The annulus is divided into 18 azimuthal sectors. After calculation of the surface intensity of each 18 sectors, we estimate the cluster circlurity using this azimuthal intensity profile. We limited this analysis into MOS 1 detector to discuss it easily. The blank sky data set of Read & Ponman (2003) were used to subtract the background events. To correct for vignetting effect, the SAS task "evigweight" was applied to both the source and background images. When we defined the average azimuthal intensity as a unit, we excluded the two clusters, A 2034 and A 2328, that out of the average intensity range from 0.2 to 2. Figure 4.1 (right) shows the resultant azimuthal intensity distribution as an example of three clusters (A 1060, A 2034 and A 2328). The selected annulus of each clusters are shown in 4.1 (left). The resultant azimuthal intensity distribution and selected annulus of all our samples are summarized in figure 4.12-4.13 and 4.6-4.11 (left).

4.2 Background Estimation

In §3.4, we described the EPIC background properties, and found that the background was divided into following components.

(1) CXB

(2) detector noise component

(3) high energy particle background (stable component)

(4) soft photon background (flaring component)

The components of (1)-(3) were basically removed when we use the blank sky data subtraction (see §4.2.2). The remaining component (4) was excluded using the timing analysis. Here, we briefly explain the background elimination process, using the case of A 1060 as an example.

4.2.1 Flare event

Many of our samples were affected by high background flares. In order to remove them, we adopted the following data cleaning process. First, we made light curves in the bands 10-12 keV for MOS and 12-14 keV for pn, where the singals are dominated by background events, and then we removed the time interval when the count rate is larger than 0.3 c s^{-1} for MOS, and 0.8 c s^{-1} for pn. Figure 4.2 compare the light curves before and after this screening. Then , we selected the photon events with pattern 0-12 for MOS and 0-4 for pn, and flag=0 (see §3.3.1). The exposure times listed in table 4.3 are those after these selections.

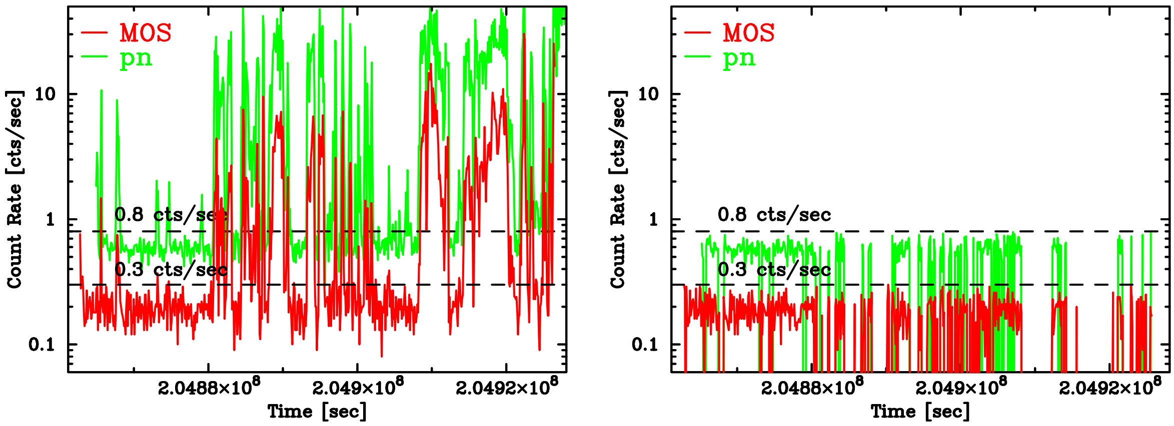

Figure 4.2: Example of A 1060 light curve for MOS and pn detectors. Left (and right) figure shows the light curve before (and after) the flare events were eliminated. The red and green curves represent the MOS and pn detector, respectively.

4.2.2 Background

In analyzing point sources, we can subtract local and simultaneous background accumulated around them. This ,however, for sources being extended over the FOV like the samples of this thesis. Accordingly, we are forced to extract the background spectrum from the blank sky data sets of Read & Ponman (2003) in the same detector region, in order to exclude the background events of (1)-(3). In this case, the remaining problem is that the non X-ray background (2), (3) is time variable, although the CXB (1) is nearly identical everywhere. Katayama et al. (2004) studied this problem and found that the count rate in the high energy band (above 10 keV) well represent the particle origin background. Therefore, the source-to-background count rate ratio was calculated from the count rates in the bands 10-12 keV and 12-14 keV for MOS and pn and the background spectrum is scaled by this factor when it is subtracted. In extracting the background spectrum, we applied the same selection criteria as explained in the previous subsection. Figure 4.3 shows the background images for MOS1,MOS2, and pn detectors from the blank sky data sets, respectively.

4.3 Elimination of Point Sources

Since we are interested in the nature of the ICM, we should remove the point sources (background or foreground AGN, binary, and galaxy) from the images. For this, we utilize the CIAO wavdetect command. This command operates on the input in two stages. First it detects possible source pixels in a dataset by repeatedly correlating it with "Mexican Hat" wavelet functions with different scale sizes. Pixels with sufficiently large positive correlation values are removed from the image as assumed sources, and subsequent correlations are performed at the same scale. The second stage generates a source list from information from the first stage at each wavelet scale. Figure 4.4 shows the result of this source detect process. These sources were eliminated when we carried out the spectral and spatial analysis.

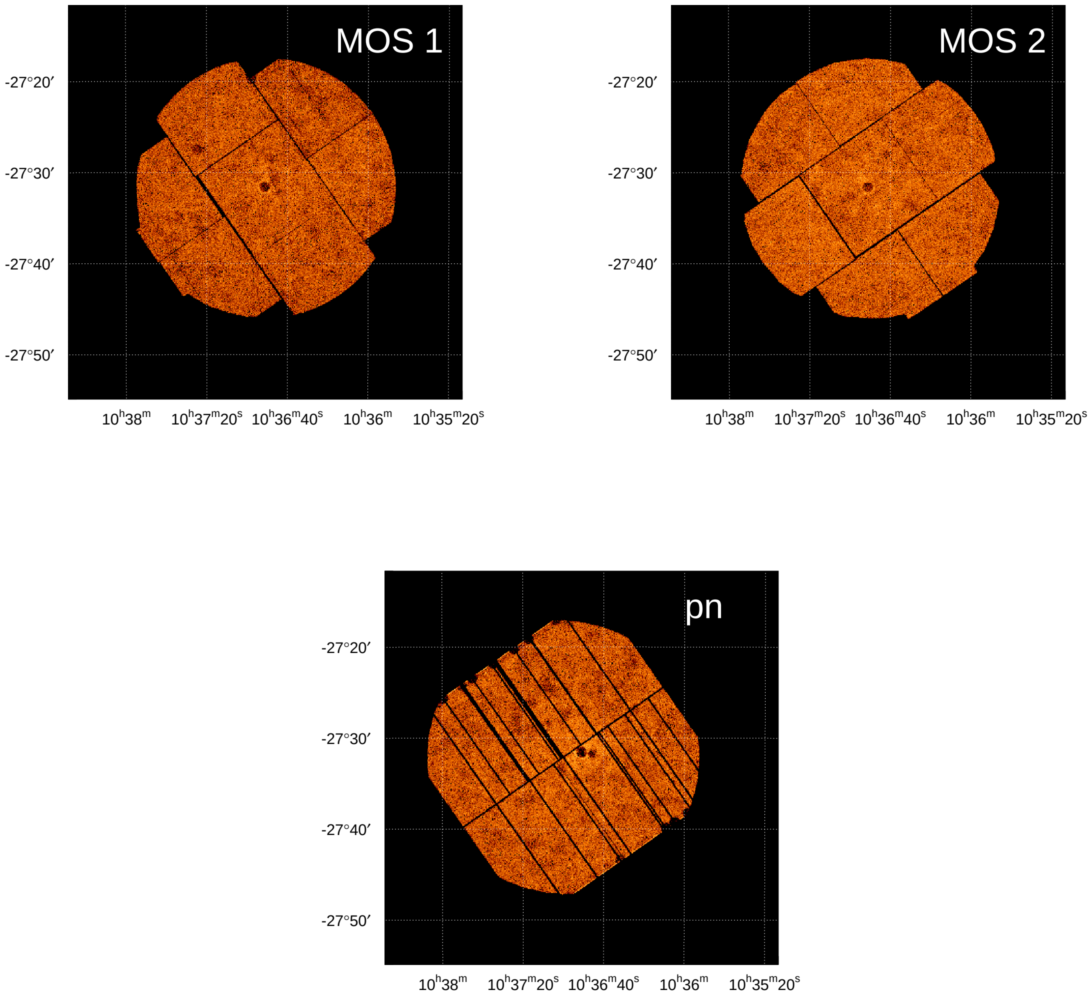

Figure 4.3: MOS1 (upper left), MOS2 (upper right), and pn (bottom) background images for full-frame model with the medium filter inserted. These images were casted onto the sky, at the position given by the A 1060, and the out of FOV region was removed.

4.4 X-ray image and radial surface brightness profile

As discussed in §3.2.1, the effective area at a given energy depends on the distance from the optical axis in the focal plane detector. In order to evaluate the surface brightness, it is necessary to correct the effect of this so-called the vignetting effect. For this to be done, the photon-weighting method of Arnanud et al. (2001), as implemented in the SAS task evigweight, was applied to source and background events separately. For each event, this task computes the corresponding weight coefficient, defined as the ratio of the effective area at the photon position and the energy to the central effective area at that energy. The weight for each photon j falling at detector coordinates ($DETX_j$, $DETY_j$) and of energy E_j were descrived by the inverse of the ratio of the effective area at that position

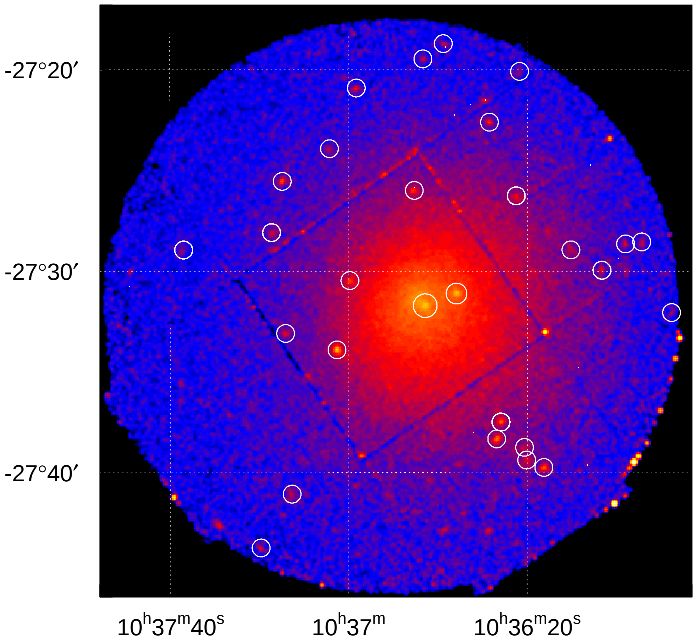

Figure 4.4: Adaptively smoothed MOS 1+2 X-ray images of A 1060 in the central $30' \times 30'$ region. The open white circles indicate the source positions which were detected using the CIAO wavdetect command.

to the central effective area,

$$w_j = \frac{A_{0,0}(E_j)}{A_{(DETX_j, DETY_j)}(E_j)}. \tag{4.1}$$

When extracting images for specified energy bands, each event is weighted by this coefficient.

Alternatively, we can use the exposure map which was calculated using the SAS eexpmap command, which takes into account the spatial quantum efficiency, filter transmission, and the telescope vignetting. This map contains the effective exposure times of the pixels, which gradually declines toward the periphery. Figure 4.5 shows the exposure map image for MOS1,MOS2, and pn detectors, respectively. We use the latter exposure map method to create the X-ray image, and when we examine the radial surface brightness profile we use the photon-weighted method. In figure 4.6-4.11, we summarized the X-ray images and the radial surface profiles of all our samples. The X-ray images were extracted in the energy range of 0.8-3.0 keV for MOS 1 & 2 detectors. The images are smoothed by a Gaussian filter with $\sigma = 3$ pixel (1 pixel = $4.4''$). The surface brightness profiles were ploted in the same energy range as the images centered on the brightness peak.

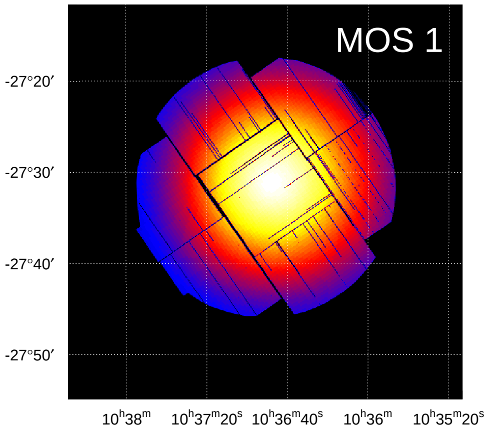

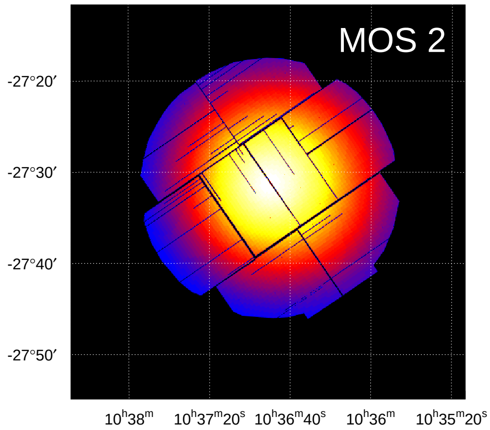

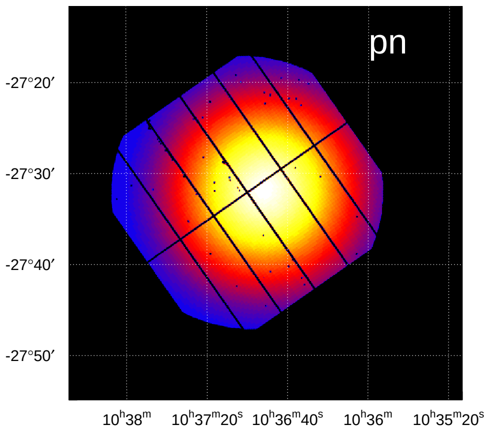

Figure 4.5: MOS1 (upper left), MOS2 (upper right), and pn (bottom) exposure map images for the A 1060 cluster observation. These images were casted onto the sky, at the position given by the A 1060, and the out of FOV region was removed.

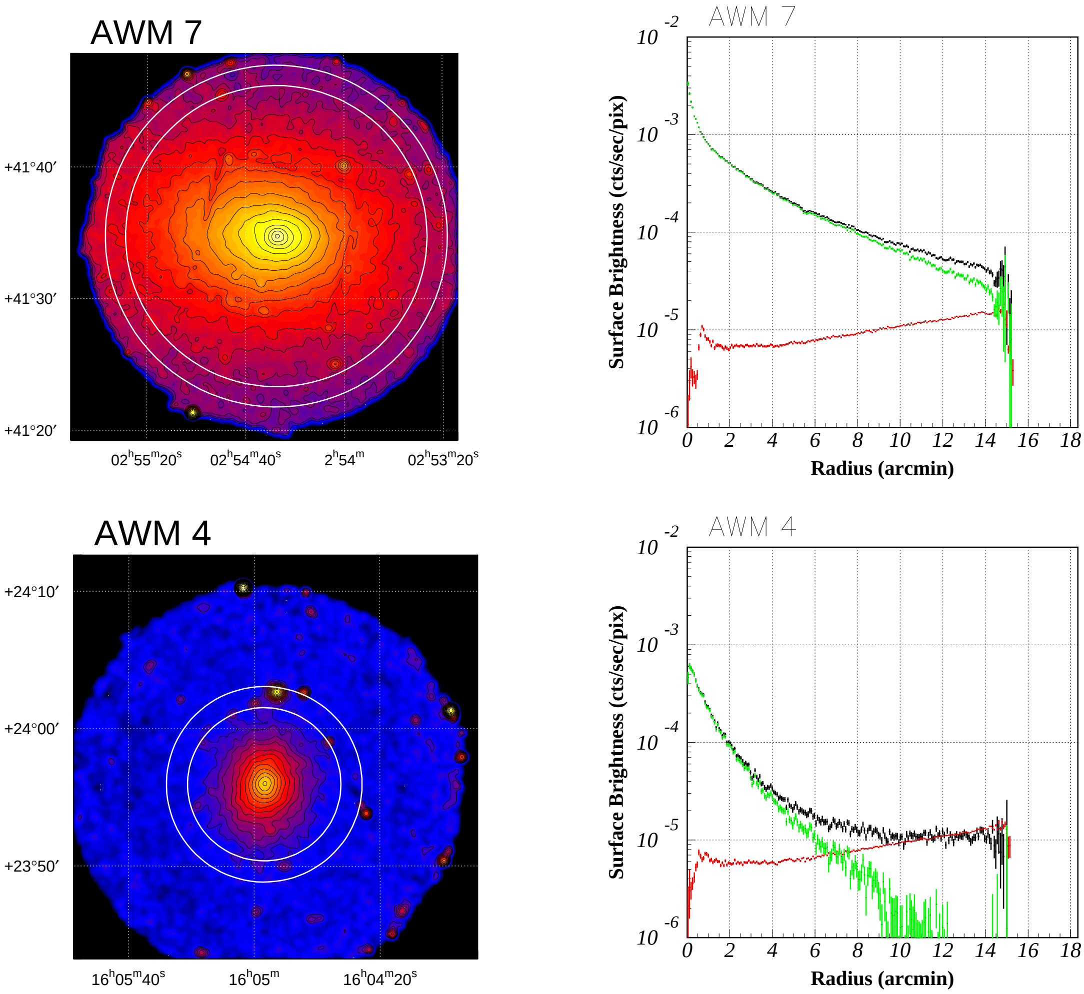

Figure 4.6: X-ray image (left) and radial brightness profile (right) of all our sample cluster. Left: The X-ray image was extracted in the energy range of 0.8-3.0 keV for MOS 1 & 2 detectors. We smoothed these images by a Gaussian filter with $\sigma = 3.0$ pixels (1 pixel $= 4.4''$). The background and exposure are subtracted and corrected. The contours were logarithmic scaled and divided into 20 region between 3×10^{-5} and 5×10^{-3} counts sec^{-1}. The annulus of each clusters represent the selected region which was used to analyze the definition of spherical symmetry in §4.1.1. The resultant intensity profile was summarized in fig 4.12-4.13. Right: Radial surface brightness profile of each clusters centerd on the luminosity peak. Te black, red and green points show the source profile, background profile and background subtracted profile of source, respectively. The background profile was estimated based on the brank sky data.

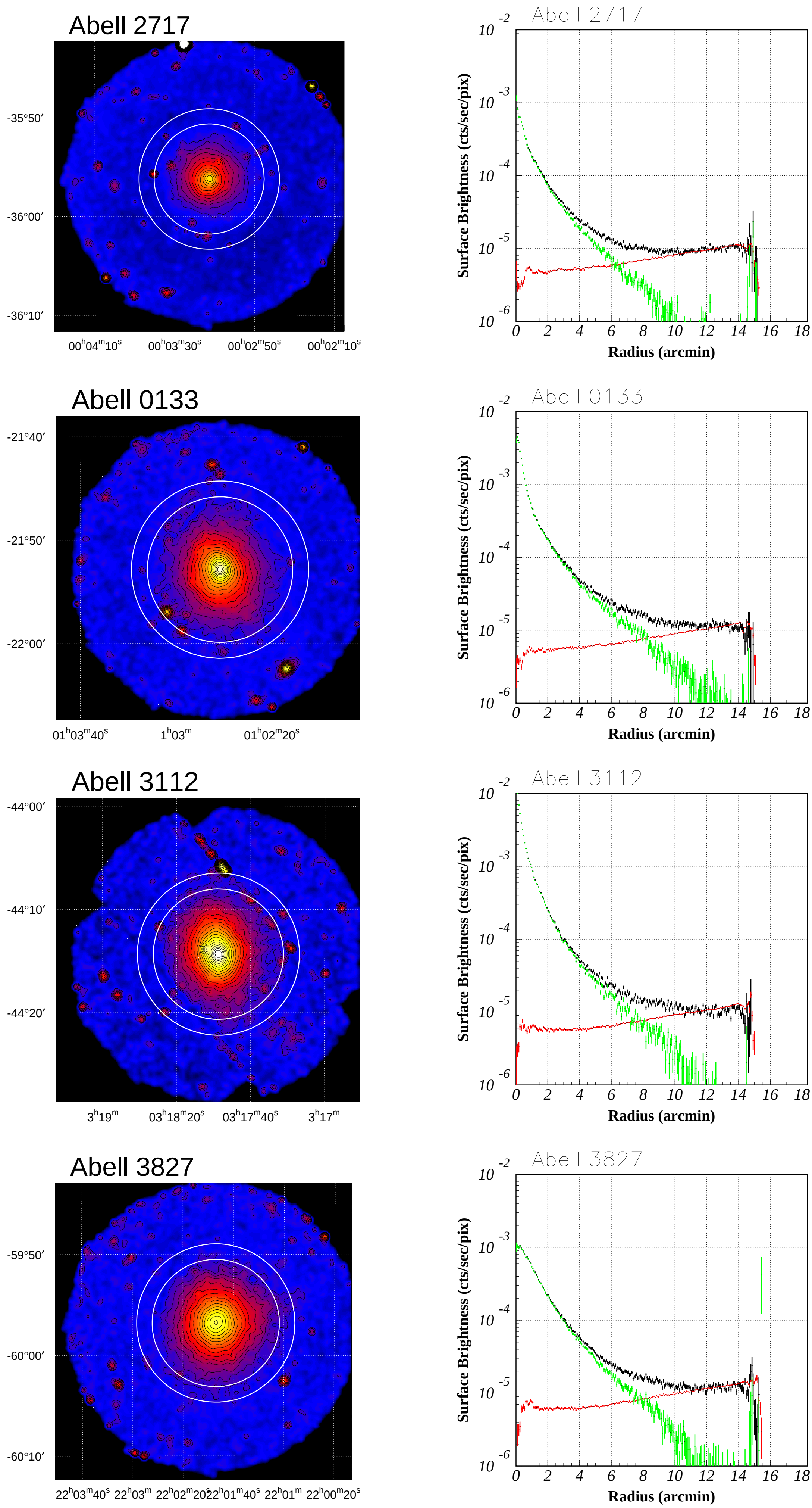

Figure 4.7: Continued

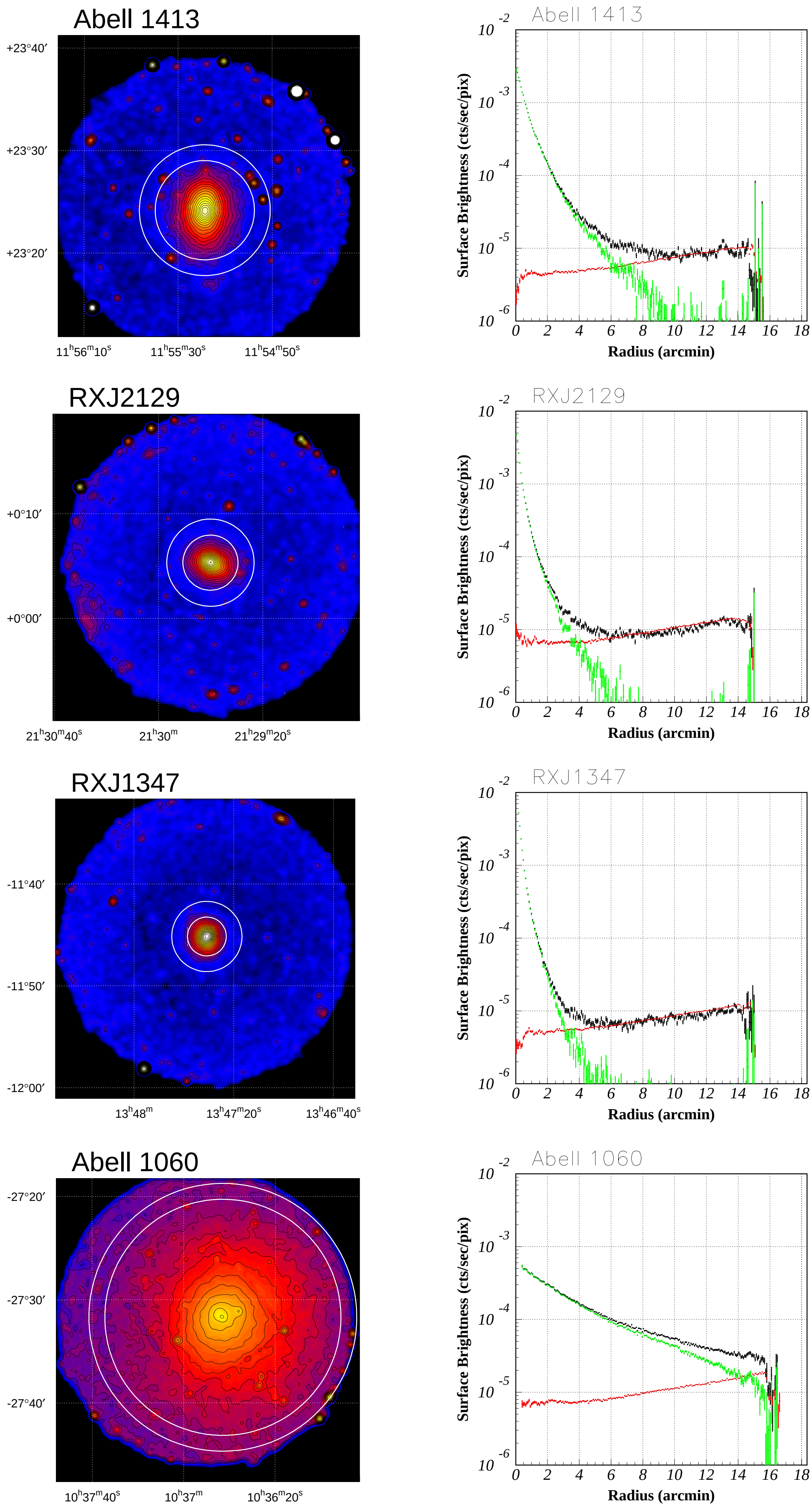

Figure 4.8: Continued

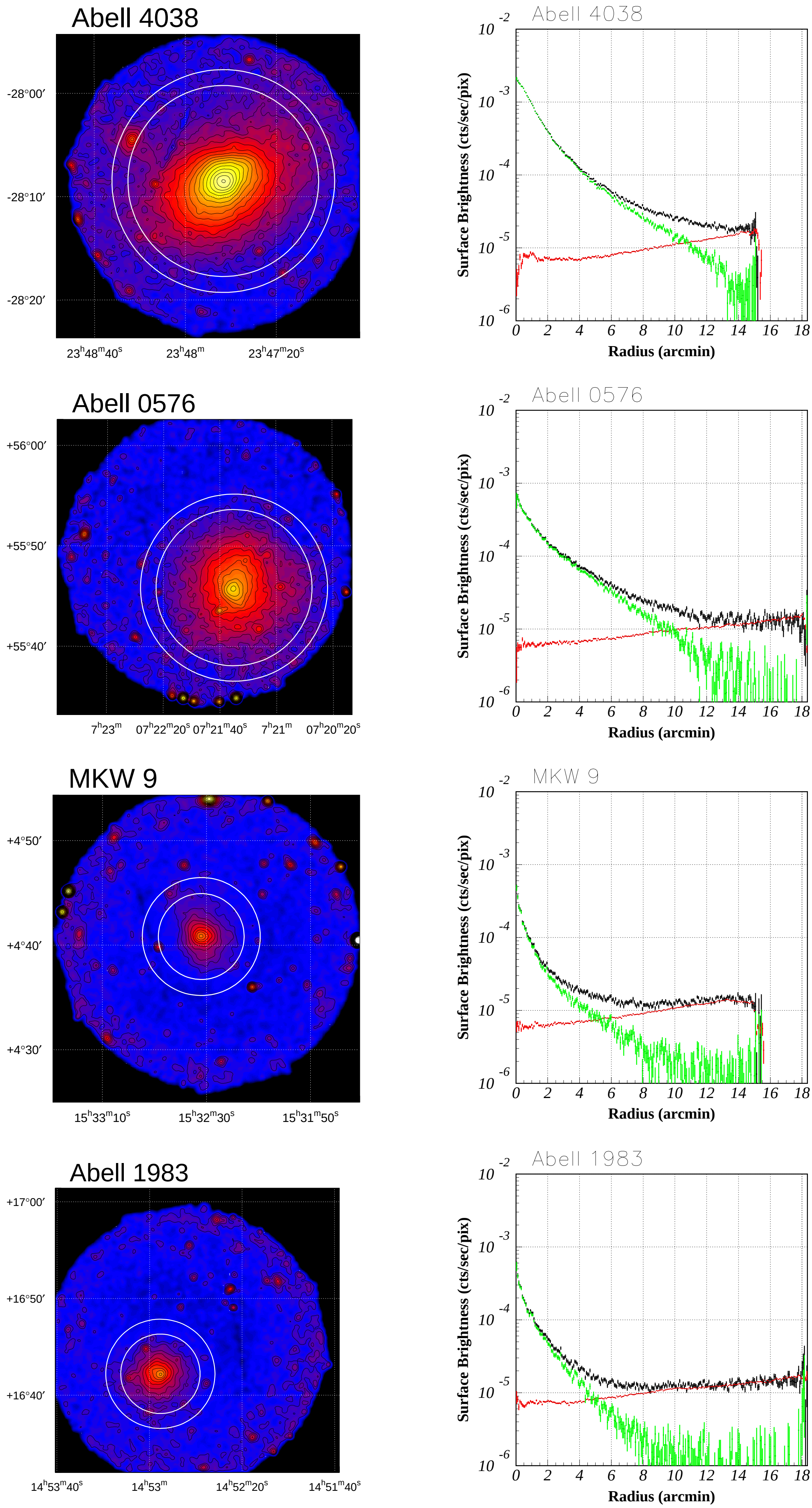

Figure 4.9: Continued.

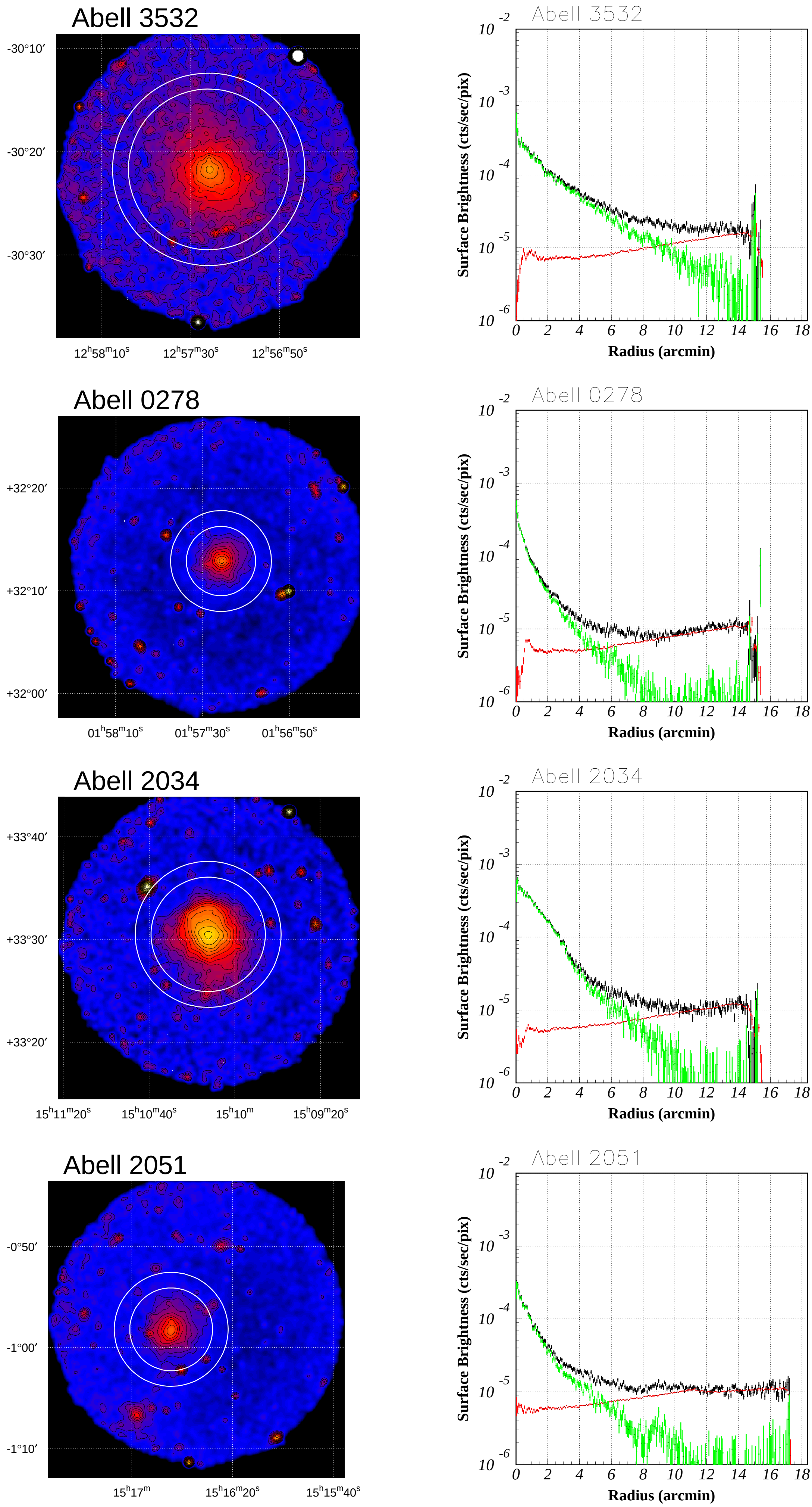

Figure 4.10: Continued

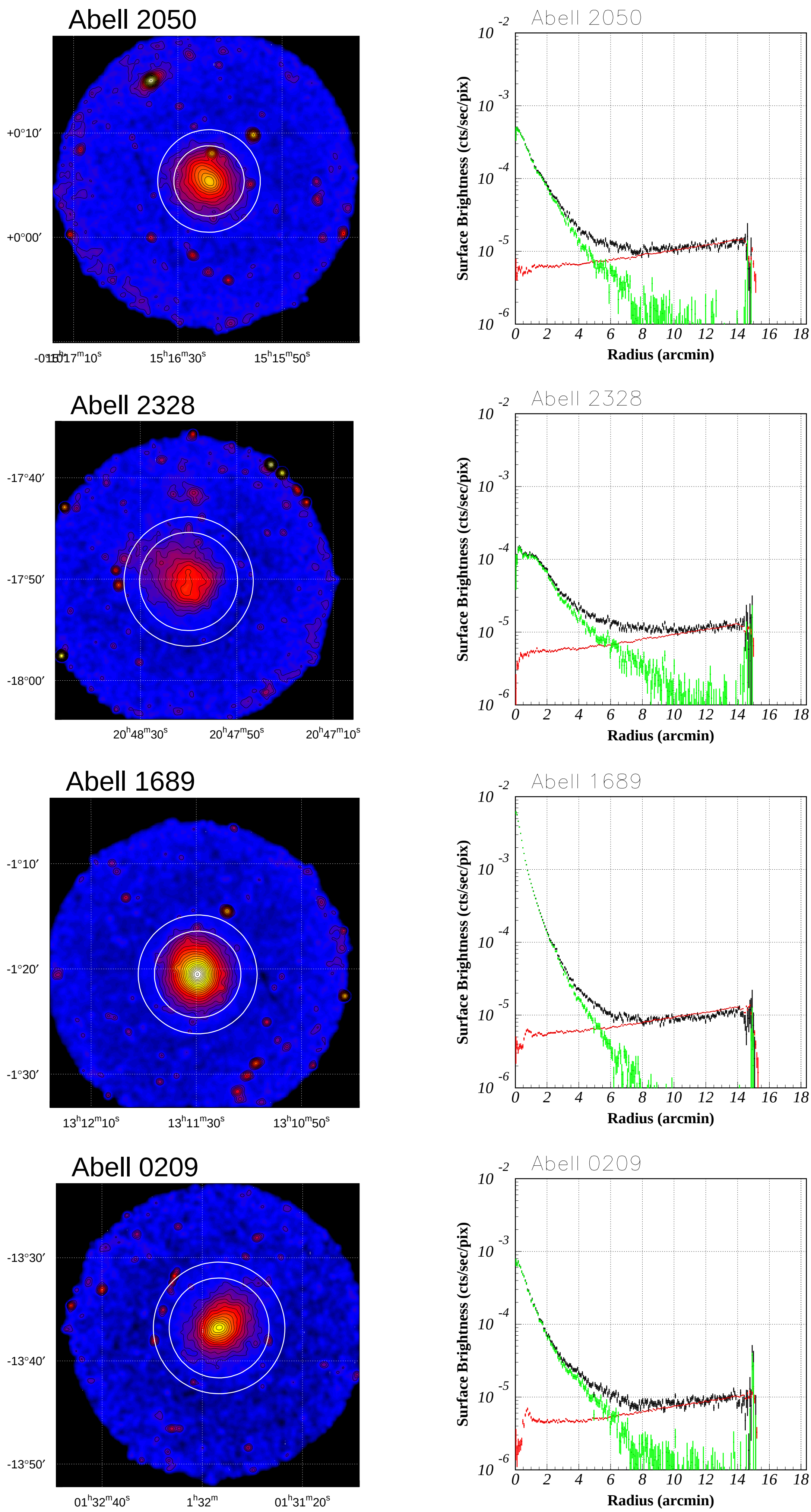

Figure 4.11: Continued

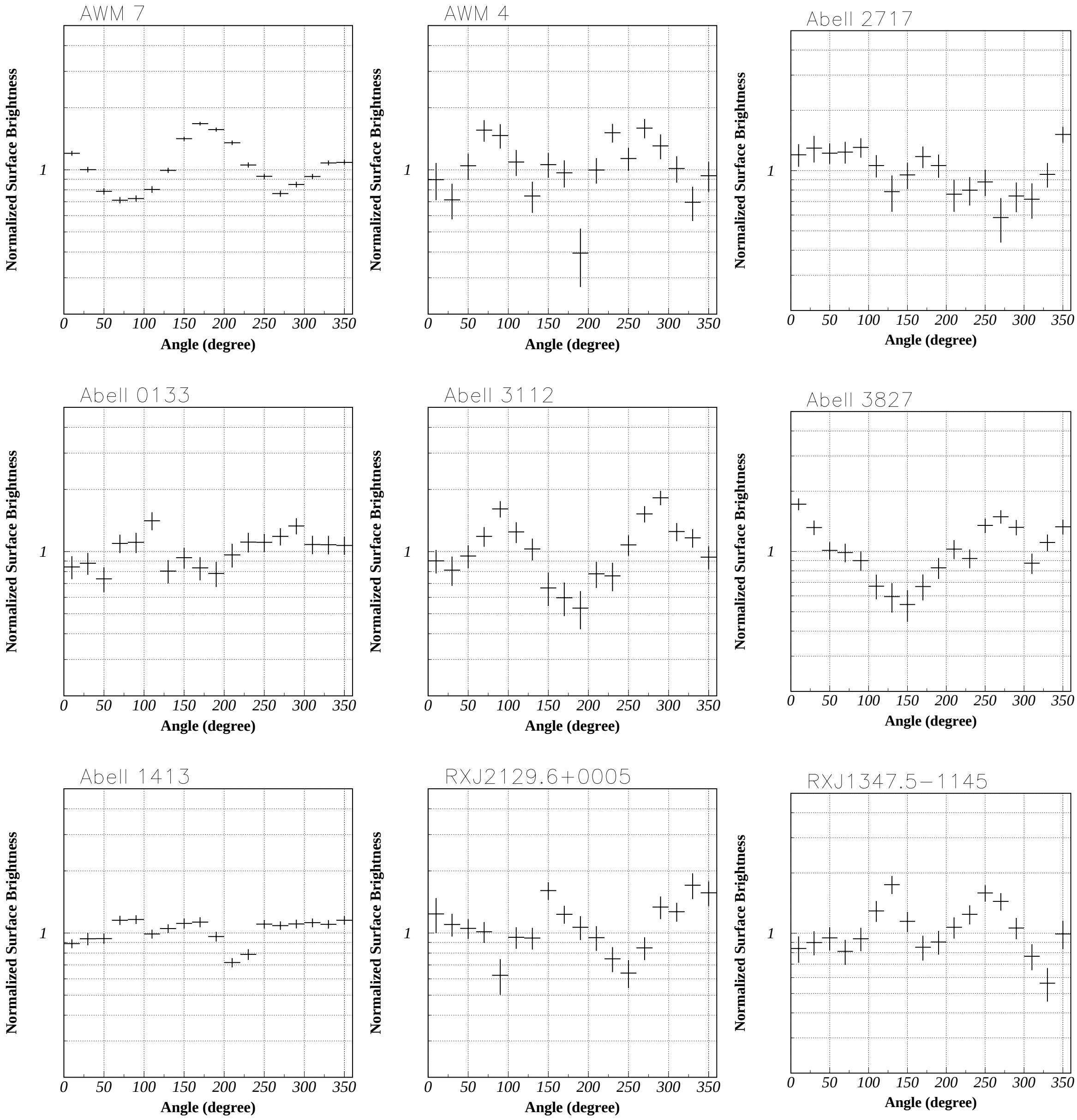

Figure 4.12: The azimuthal intensity distribution in the anulus which was described in fig. 4.6-4.11 (left) of all our clusters.

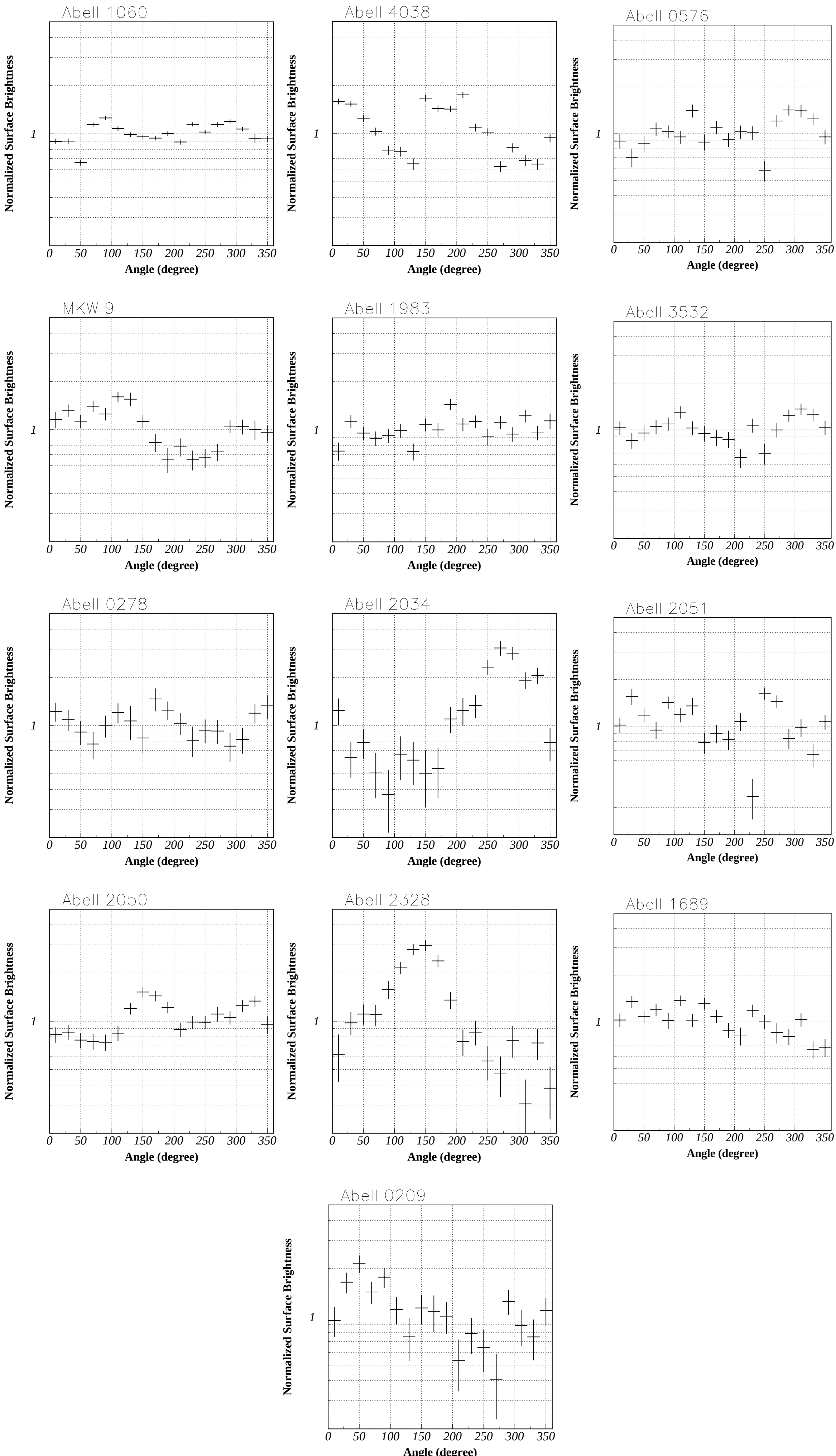

Figure 4.13: Continued.

Chapter 5

Spectral Analysis

5.1 Analysis of the Spatially-Averaged Spectrum

5.1.1 Derivation of the spatically-averaged spectrum

Based on the X-ray images in the 0.8-8 keV band for the MOS 1 & 2 after the point source elimination (§4.3) we made a radial surface brightness profile centered at the X-ray emission peak position. We accumulate spectra from a circular region centered at the peak out to the radius where the signal to noise ratio becomes equal to unity. profile. We then subtract background spectra that were obtained from the blank sky data (§4.2.2). The instrument response can be split up into two parts: a Redistribution Matrix File (RMF), which specifies the channel probability distribution for a photon of given energy, and an Ancillary Response File (ARF) which specifies the telescope area and window absorption. We built the RMF and ARF with the SAS tasks rmfgen and arfgen, by referring to conditions of extracting the spectra. In subtracting the background, we renormalize background spectrum by the intensity ratio above 10 keV (§4.2.2). Even after this, some sources show structures at the energies of Ni, Cu and Zn K lines for the pn detector around 8 keV. Accordingly, we ignore the energy above 7.5 keV for the pn detector.

5.1.2 Model fitting

We carried out a spectral fitting analysis to measure the average X-ray temperature and abundance of the ICM. We assume a theoretical model spectrum, convolve it with the instrumental responses described above, and fit it to the observed spectrum by adjusting the model parameters, according to the χ^2 statistics. The spectral fittings are performed using the XSPEC version 11.2 analysis software (Arnaud 1996), which is commonly used in X-ray astrophysics community.

We fitted the spectra from all detectors simultaneousrly with an absorbed thin-thermal plasma emission model (MEKAL + wabs). We adopt for the metal abundance standard the solar photospheric value tabulated in Anders and Grevesse (1989), in which $(\mathrm{Fe/H})_\odot = 4.68 \times 10^{-5}$ for iron, for example. There are five parameters in the MEKAL model, the temperature kT, the metallicity relative to the solar abundance Z, the redshift z, the normalization factor N, and the thickness of the galactic absorber N_H. The redsift and the galactic absorption of each object was fixed at the cataloged value in the NED database (NASA/IPAC Extragalactic Database) and the value of 21 cm measurement (Dickey & Lockman 1990), respectively. We rebinned the spectral channels so that each bin contains at least 100 photons. In figure 5.1, we show a result of spectral fitting with the absorbed MEKAL model for A 1060 as an example.

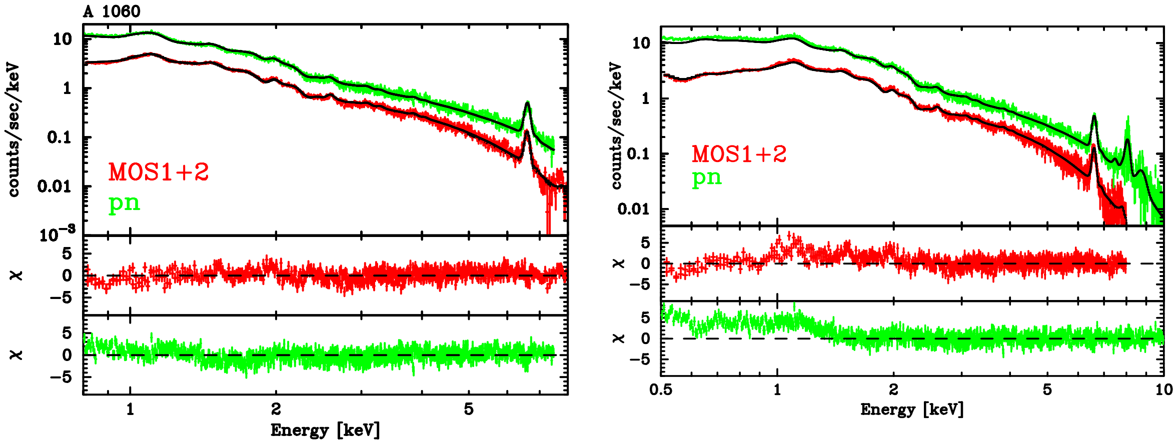

Figure 5.1: MOS1+2 and pn spectra extracted from the $< 13'$ region. The left (right) panel show the result of the absorbed MEKAL model fitting in the 0.8-8.0 keV (2.0-8.0 keV) and 0.8-7.5 keV (2.0-10.0 keV) for MOS1+2 and pn, respectively. In the right panel, the energy range below 2.0 keV is simply retrieved after the model fitting in the band 2.0-8.0 (2.0-10.0) keV for MOS 1+2 and pn.

5.1.3 Gain adjustment of pn spectra

In the course of analysis of the pn spectra, we found remarkable gain shift at around the energy of Fe-K lines in the 3 clusters, A 0133, A 0576 and RXJ2129+0005. In order to demonstrate this, we first show the A0133 spectra from MOS 1+2 and pn detectors simultaneously with the absorbed MEKAL model in the bands 0.8-8.0 keV for MOS1+2 and 0.8-7.5 keV for pn, where the redshift was fixed at the cataloged value of z =0.0566 in the NED database. The result of the model fit is shown in Figure 5.2 (left). The fit residual in the 6-7 keV band is obvious only in the pn spectrum, whereas that there is no such structure in the MOS spectra when we used the cataloged redshift value. Note that the gain shift in the pn detector disappears if we adopt a different value of $z = 0.0470$ for the redshift, as displayed in Fig. 5.2. Accordingly, we decided to rescale the energy of the pn spectra using the XSPEC 'gain' command. We estimate the gain value. As for the XSPEC 'gain' command, we can use the 2 parameters: slope and offset. We only change the slope parameter with offset paramater being untouched. Figure 5.3 shows the dependece of the $\chi^2/d.o.f$ value on the slope parameter. The three in the figure indicate the locations providing the minimum $\chi^2/d.o.f.$ value for each cluster. The redshift, the slope parameter and $\chi^2/d.o.f.$ values are summarized in Table 5.1. The best fit gain slope parameters of the three clusters are slightly different with each other. We therefore use the best-fit slope parameter separately for the three clusters. The gain parameters are not changed for the other clusters. Figure 5.4 shows, for example, the result of model fitting of the pn spectrum of A0113 before and after the gain correction. When we use slope=1.009 and offset=0, the feature around the Fe-K line almost disappears.

5.1.4 Soft excess of pn detector

Spectra of the clusters show excess above the single temperature MEKAL model at the energy below ~ 1.5 keV especially in the pn specta. As an example, figure 5.1 shows the result of a combined fit of the absorbed MEKAL model to the MOS1+2 and pn spectra of the $r < 13'$ region in the band 2.0-8.0 keV (2.0-10.0 keV) for MOS 1+2 (pn). In this

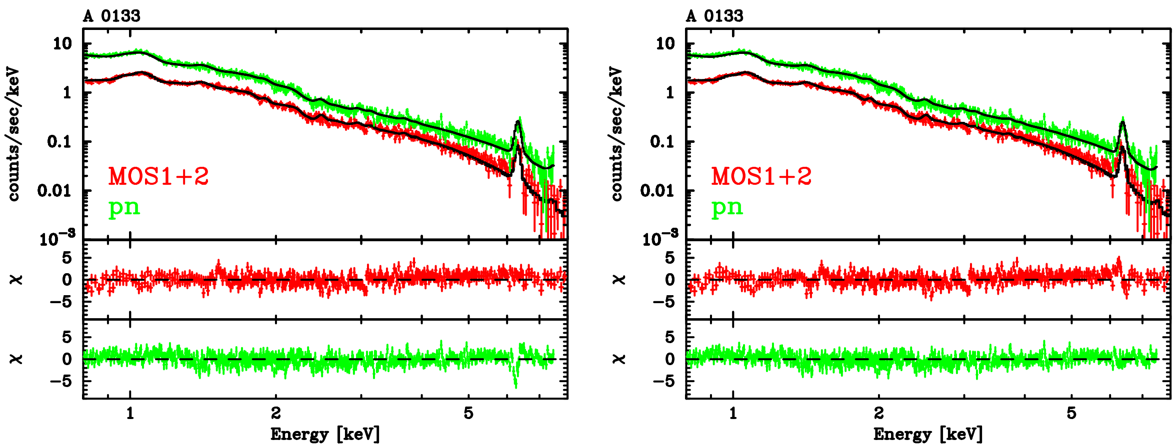

Figure 5.2: MOS1+2 and pn spectra extracted from the $<^1 1'$ region. The left panel show the result of the absorbed MEKAL model fitting when we adopt the the cataloged redshift value, $z = 0.0566$, based on the NED database. The right pannel spectra are fitted when we use the new redshift value of $z = 0.0470$, which was estimated by the independent fit of pn spectrum under the condition of redshift free.

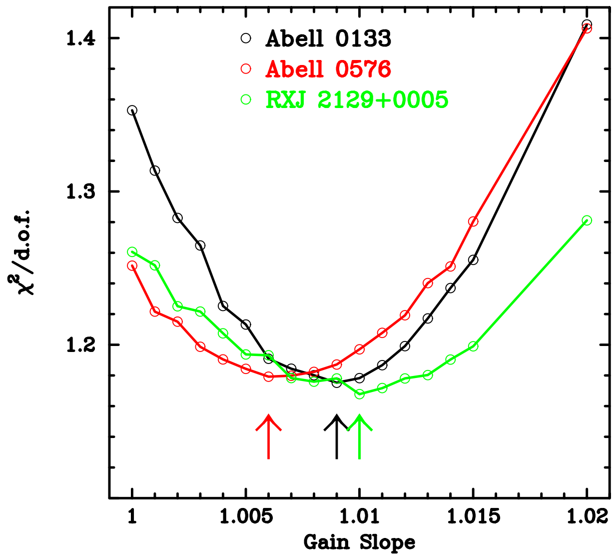

Figure 5.3: Dependence of $\chi^2/d.o.f.$ value on the slope parameter of the XSPEC gain command for the three clusters, A 0133, A0576, and RXJ2129. The arrows indicate the best-fit slope parameters.

plot, we carried out the fit in the band 2-10 keV, and then simply retrieve the data points below 2 keV. This apparent soft excess, however cannot be a real emission component because it is incompatible with previous observation (Tamura et al. 2000). Accordingly, we decided to neglect the energy channels below 1.5 keV of pn spectra of clusters if they show apparent soft excess that is incompatible with the MOS detectors.

5.1.5 Results of spectral fit to the spatial average spectra

After the considerations on the pn spectrum above, we carried out a spectral fitting to examine the spatially averaged ICM temperature and abundance. We summarize the

Table 5.1: Gain value

Cluster	z		gain	$\chi^2/d.o.f.$		
	nominal	shift	slope	default	z shift	gain shift
A 0133	0.0566	0.0470	1.009	1.353	1.174	1.175
A 0576	0.0389	0.0313	1.006	1.222	1.174	1.179
RXJ2129+0005	0.2350	0.2220	1.010	1.252	1.152	1.168

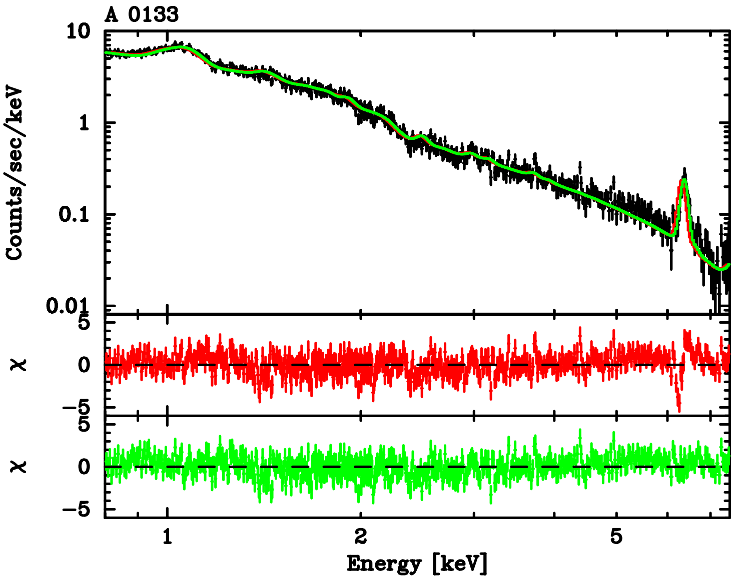

Figure 5.4: The results of the absorbed MEKAL model fit to the pn spectrum of A 0133 before and after with red and green colors, respectively. The middle and bottom panel show the fit residuals in a unit of σ. The redshift is fixed at the cataloged value $z = 0.0566$.

resultant best-fit parameters in Table 5.2, and the fitted spectra of all our samples were summarized in figure 5.5-5.7. The temperature of these samples distribute uniformly from 1 keV to 10 keV.

Table 5.2: Summary of the Spectral Analysis

Cluster	T	Z	R$_{max}$		L^X	$\chi^2/d.o.f.$
	[keV]	[solar]	[arcmin]	[kpc]	[erg/s]	
AWM7	$3.68^{+0.02}_{-0.02}$	$0.519^{+0.014}_{-0.014}$	14.0	271.8	3.94×10^{43}	1.456
AWM4	$2.43^{+0.07}_{-0.07}$	$0.313^{+0.040}_{-0.037}$	9.0	315.0	1.28×10^{43}	1.312
A2717	$2.17^{+0.03}_{-0.04}$	$0.375^{+0.029}_{-0.027}$	9.5	497.8	2.23×10^{43}	1.501
A0133	$3.37^{+0.05}_{-0.05}$	$0.495^{+0.033}_{-0.032}$	11.0	646.8	8.53×10^{43}	1.318
A3112	$3.99^{+0.05}_{-0.05}$	$0.429^{+0.023}_{-0.022}$	9.5	729.9	2.23×10^{44}	1.592
A3827	$6.90^{+0.16}_{-0.16}$	$0.297^{+0.035}_{-0.034}$	9.5	922.1	2.86×10^{44}	1.341
A1413	$6.94^{+0.18}_{-0.19}$	$0.298^{+0.038}_{-0.037}$	9.0	1181.8	3.98×10^{44}	1.176
RXJ2129+0005	$6.27^{+0.20}_{-0.20}$	$0.361^{+0.042}_{-0.041}$	6.0	1131.6	5.02×10^{44}	1.133
RXJ1347-1145	$11.17^{+0.40}_{-0.40}$	$0.303^{+0.046}_{-0.046}$	5.0	1360.9	2.40×10^{45}	1.274
A1060	$3.25^{+0.03}_{-0.03}$	$0.407^{+0.014}_{-0.014}$	13.0	168.9	8.05×10^{42}	1.436
A4038	$2.90^{+0.02}_{-0.02}$	$0.352^{+0.015}_{-0.015}$	13.0	430.6	5.60×10^{43}	1.393
A0576	$3.89^{+0.10}_{-0.10}$	$0.364^{+0.038}_{-0.037}$	11.0	465.4	4.43×10^{43}	1.281
MKW9	$1.57^{+0.06}_{-0.06}$	$0.152^{+0.030}_{-0.026}$	9.5	409.6	8.74×10^{42}	1.274
A1983	$1.93^{+0.07}_{-0.07}$	$0.284^{+0.042}_{-0.038}$	7.0	333.5	9.82×10^{42}	1.627
A3532	$5.65^{+0.20}_{-0.20}$	$0.366^{+0.072}_{-0.069}$	11.0	644.7	7.20×10^{43}	1.078
A0278	$2.78^{+0.14}_{-0.14}$	$0.173^{+0.064}_{-0.055}$	7.0	624.4	3.02×10^{43}	1.178
A2034	$7.37^{+0.43}_{-0.31}$	$0.324^{+0.073}_{-0.071}$	9.0	994.3	2.46×10^{44}	1.065
A2051	$2.85^{+0.15}_{-0.12}$	$0.157^{+0.055}_{-0.049}$	7.0	845.0	6.17×10^{43}	1.284
A2050	$4.51^{+0.14}_{-0.14}$	$0.275^{+0.053}_{-0.051}$	7.0	1109.9	1.44×10^{44}	1.408
A2328	$4.54^{+0.17}_{-0.17}$	$0.218^{+0.056}_{-0.054}$	9.0	980.1	1.72×10^{44}	1.557
A1689	$8.75^{+0.19}_{-0.19}$	$0.245^{+0.029}_{-0.029}$	7.0	1109.9	7.84×10^{44}	1.281
A0209	$7.08^{+0.31}_{-0.31}$	$0.238^{+0.060}_{-0.059}$	7.0	1206.7	4.21×10^{44}	1.062

Table 5.3: Results of Spectral fit (PN)

Cluster	kT [keV]	Z [solar]	$\chi/d.o.f.$	Ratio*
A0133	$3.04^{+0.11}_{-0.05}$	$0.443^{+0.029}_{-0.028}$	1.174	0.90
	$3.56^{+0.31}_{-0.15}$	$0.381^{+0.051}_{-0.049}$	1.052	1.06
A0209	$6.42^{+0.66}_{-0.33}$	$0.275^{+0.063}_{-0.060}$	1.197	0.91
	$7.89^{+1.78}_{-0.80}$	$0.304^{+0.086}_{-0.078}$	1.226	1.05
A0278	$2.69^{+0.28}_{-0.14}$	$0.171^{+0.058}_{-0.052}$	1.197	0.969
	$4.46^{+1.79}_{-0.69}$	$0.037^{+0.109}_{-0.037}$	1.142	1.604
A0576	$3.59^{+0.13}_{-0.07}$	$0.346^{+0.033}_{-0.032}$	1.174	0.92
	$3.98^{+0.41}_{-0.20}$	$0.348^{+0.049}_{-0.048}$	1.138	1.02
A1060	$3.09^{+0.05}_{-0.03}$	$0.363^{+0.013}_{-0.012}$	1.501	0.95
	$3.40^{+0.12}_{-0.06}$	$0.322^{+0.021}_{-0.020}$	1.117	1.05
A1413	$7.03^{+0.34}_{-0.17}$	$0.313^{+0.033}_{-0.033}$	1.179	1.01
	$8.92^{+0.94}_{-0.46}$	$0.332^{+0.043}_{-0.044}$	0.994	1.29
A1689	$8.70^{+0.37}_{-0.18}$	$0.251^{+0.026}_{-0.026}$	1.261	0.99
	$10.50^{+1.00}_{-0.50}$	$0.265^{+0.033}_{-0.032}$	1.030	1.20
A2034	$6.61^{+0.64}_{-0.32}$	$0.202^{+0.055}_{-0.054}$	1.202	0.897
	$7.27^{+1.46}_{-0.64}$	$0.174^{+0.060}_{-0.060}$	1.249	0.986
A2050	$4.09^{+0.27}_{-0.13}$	$0.268^{+0.046}_{-0.044}$	1.224	0.907
	$4.92^{+0.85}_{-0.43}$	$0.291^{+0.060}_{-0.058}$	1.136	1.091
A2051	$2.68^{+0.23}_{-0.12}$	$0.230^{+0.057}_{-0.051}$	1.317	0.941
	$3.37^{+0.81}_{-0.36}$	$0.313^{+0.132}_{-0.117}$	1.231	1.184
A2328	$3.68^{+0.36}_{-0.13}$	$0.180^{+0.047}_{-0.045}$	1.104	0.811
	$4.64^{+1.03}_{-0.42}$	$0.109^{+0.061}_{-0.059}$	1.173	1.023
A2717	$2.19^{+0.06}_{-0.03}$	$0.411^{+0.027}_{-0.026}$	1.343	1.01
	$2.53^{+0.25}_{-0.12}$	$0.360^{+0.077}_{-0.072}$	1.130	1.17
A3112	$3.97^{+0.10}_{-0.05}$	$0.455^{+0.022}_{-0.022}$	1.524	0.99
	$4.82^{+0.31}_{-0.16}$	$0.397^{+0.028}_{-0.027}$	1.141	1.21
A3532	$5.13^{+0.48}_{-0.24}$	$0.294^{+0.060}_{-0.059}$	1.002	0.91
	$5.62^{+1.19}_{-0.51}$	$0.238^{+0.070}_{-0.068}$	1.197	0.99
A3827	$6.94^{+0.34}_{-0.17}$	$0.282^{+0.032}_{-0.031}$	1.064	1.01
	$8.09^{+0.91}_{-0.45}$	$0.294^{+0.039}_{-0.038}$	1.044	1.17
A4038	$2.85^{+0.04}_{-0.02}$	$0.337^{+0.013}_{-0.012}$	1.375	0.983
	$3.24^{+0.13}_{-0.07}$	$0.318^{+0.024}_{-0.023}$	1.021	1.13
AWM4	$2.42^{+0.14}_{-0.07}$	$0.324^{+0.038}_{-0.035}$	0.980	1.00
	$2.76^{+0.42}_{-0.19}$	$0.178^{+0.084}_{-0.078}$	0.941	1.14
AWM7	$3.48^{+0.05}_{-0.02}$	$0.473^{+0.015}_{-0.015}$	1.381	0.952
	$3.87^{+0.15}_{-0.07}$	$0.428^{+0.021}_{-0.021}$	1.010	1.05
MKW9	$1.34^{+0.08}_{-0.04}$	$0.087^{+0.018}_{-0.017}$	1.696	0.85
	$1.94^{+0.54}_{-0.26}$	$0.560^{+0.398}_{-0.288}$	0.922	1.24
RXJ1347	$10.51^{+0.72}_{-0.36}$	$0.269^{+0.042}_{-0.042}$	1.311	0.94
	$14.4^{+1.97}_{-0.94}$	$0.305^{+0.061}_{-0.060}$	0.985	1.29
RXJ2129	$5.46^{+0.28}_{-0.14}$	$0.398^{+0.043}_{-0.042}$	1.152	0.87
	$6.70^{+0.80}_{-0.39}$	$0.392^{+0.053}_{-0.052}$	1.038	1.07

* Temperature ratio (pn/MOS 1+2)

5.2 Radial Distribution

In studying cluster of galaxies, we usually use spatial distribution of the temperature and the metal abundance of the ICM, because these spatial distributions give us a lot of information (see §2 Review of Cluster Structure). The temperature and abundance distributions depend upon whether the cD galaxy exists or not in the cluster. The cD galaxy is thought to raise the abundance concentration at the center and to prevent the cluster central cooling (De Grandi et al 2002). In addition, the radial temperature profile is of essential importance in calculating the gravitational mass distribution based on hydrostatic equilibrium (eq. 2.31). We thus carry out spatially resolved spectral analysis for concentric annuli centered on the surface brightness peak, and evaluate their radial temperature and abundance for all our samples by fitting an absorbed MEAKL model to the observed spectra.

We first removed galaxies and point sources. The annuli are segmented from inner to outer radii so that they include at least 10000 photons for all the detectors. For A 1060, A 4038 and AWM 7, which have sufficient photons and good statistics, we use the photon threshold 20000 photons instead of 10000 photons. The MOS and pn spectra were fitted simultaneously with an absorbed MEKAL model. The absorber's hydrogen column density was fixed at the each Galactic values. The energy scale of the spectra are adjusted according to § 5.1.3. In fitting the spectra, we adopt the 0.8-8.0 keV band for MOS1+2 and the 0.8-7.5 keV band for pn detector.

In figure 5.8-5.10, the resultant temperature and metal abundance distributions were summarized. We also showed the temperature distribution when we fixed the metal abundance as $0.3Z_{\odot}$. When the temperature of sample cluster is lower than $\sim$3 keV, the temperature is estimated as lower value than the ture temperature at the detectors outer region. In that case, the metal abundance has reached to almost zero. This is obviously wrong. To check it, we produced a radial temperature profile as in the case of the fixed value 0.3 solar for metal abundance. These results were ploted on the same figure (fig. 5.8-5.10).

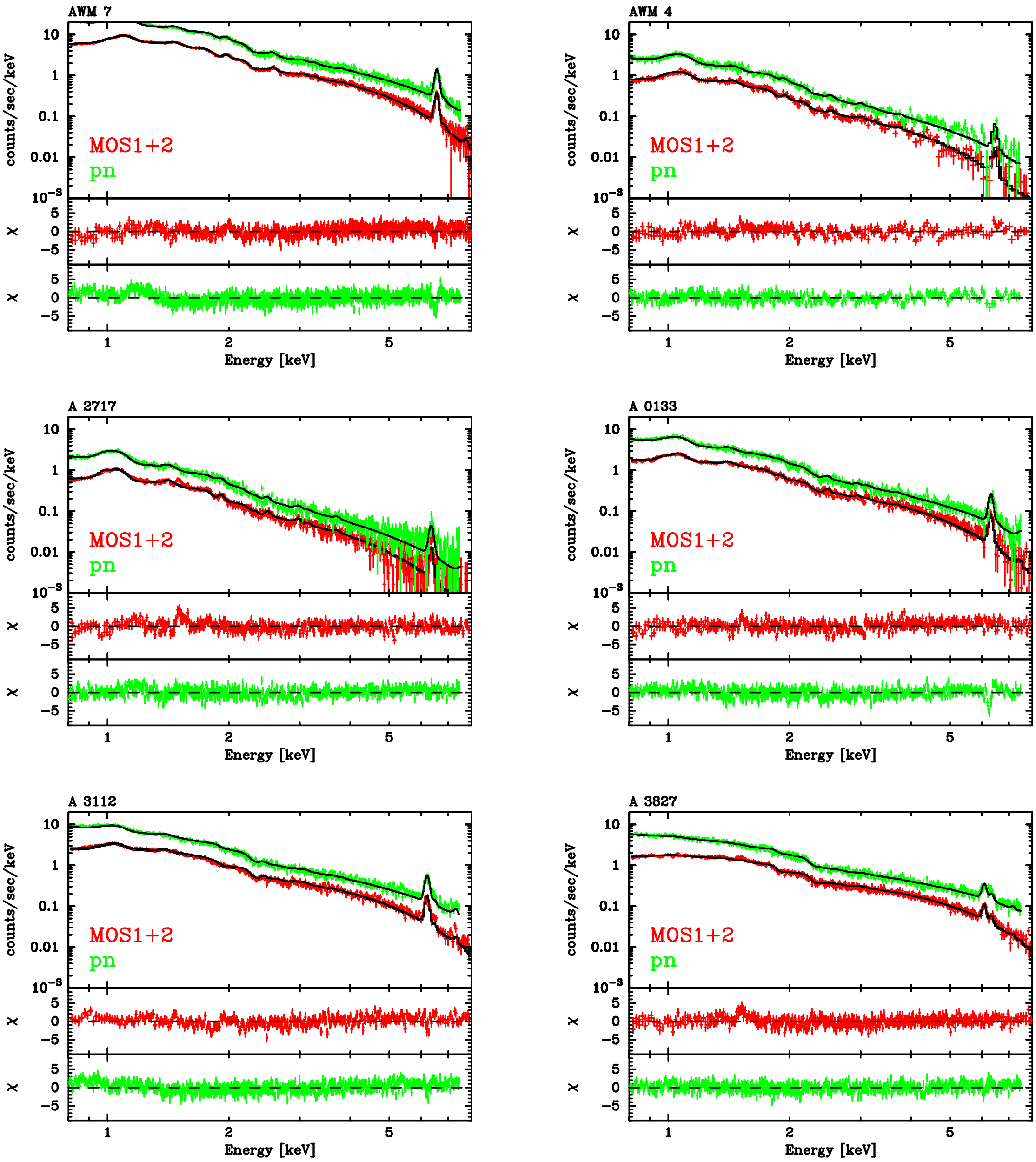

Figure 5.5: MOS1+2 & pn spectra of all our sample clusters. For each cluster, the spectra fitted simultaneously with the absorbed MEKAL model in the 0.8-8.0 keV and 0.8-7.5 keV for MOS1+2 and pn, respectively. For the three clusters, A 0133, A 0576 and RXJ2129+0005, we made the gain correction for the pn spectrum (§ 5.1.3). The values of the slope parameter of the XSPEC gain command are summarized in tab. 5.1.

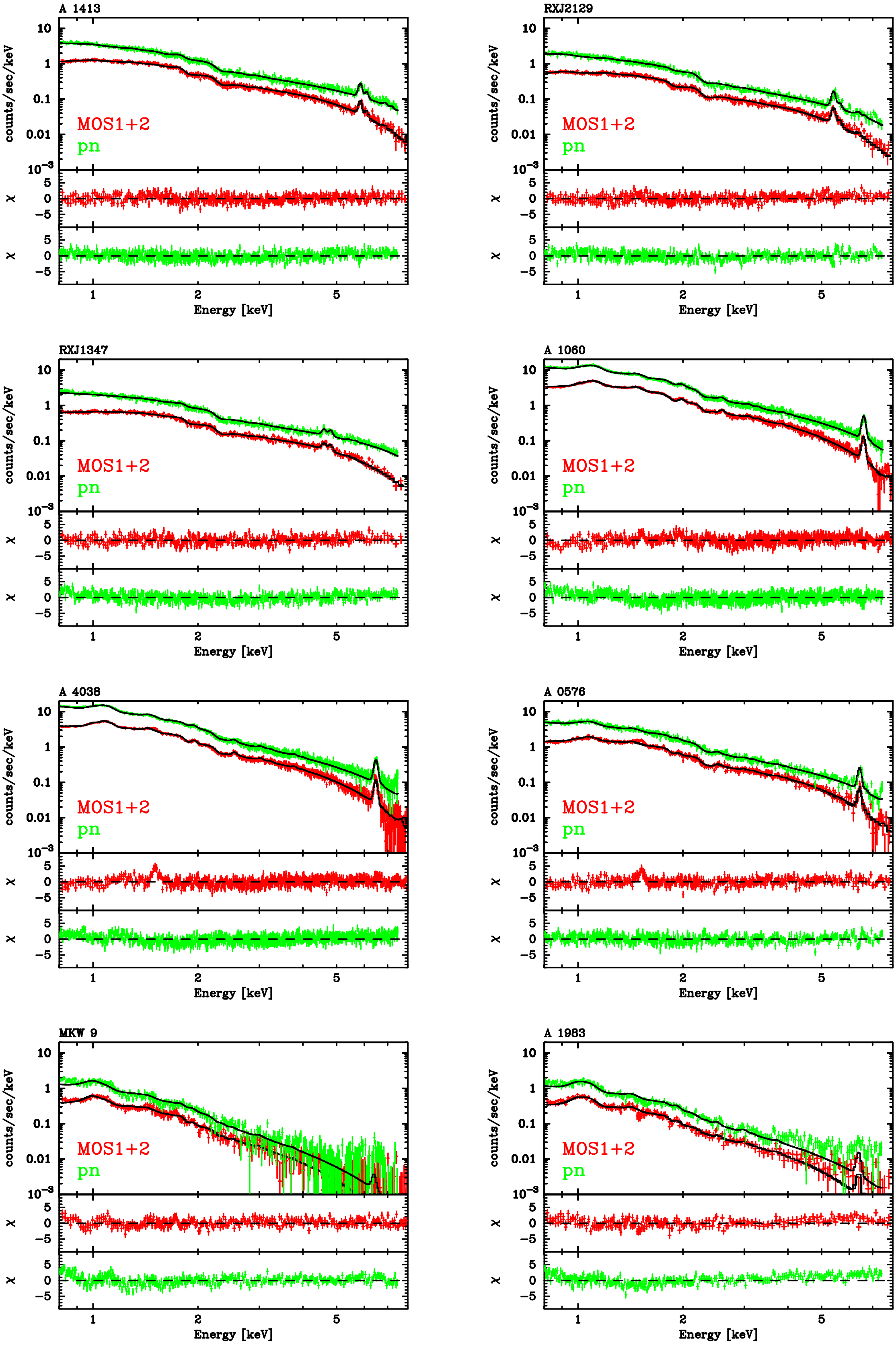

Figure 5.6: Continued.

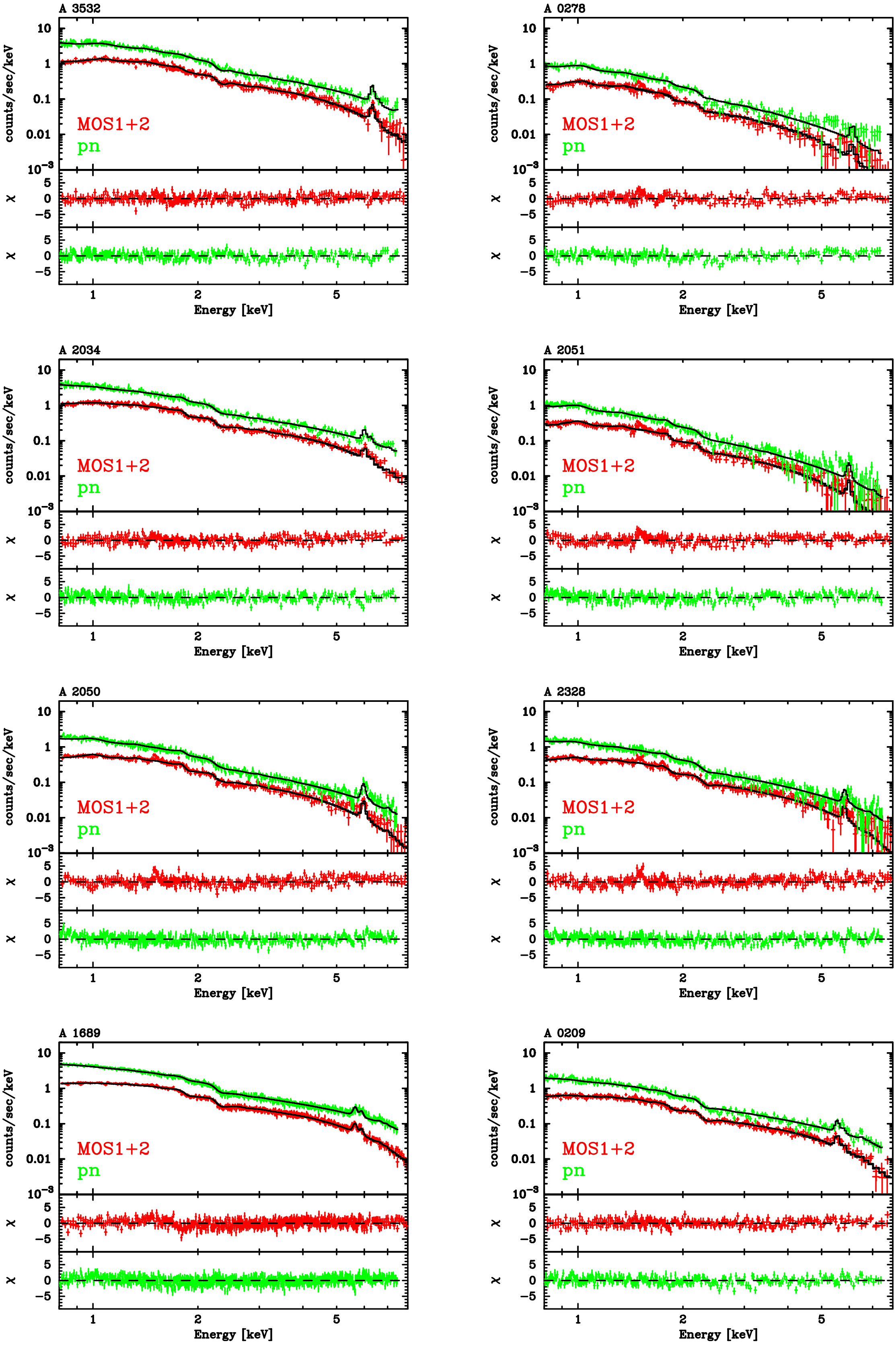

Figure 5.7: Continued.

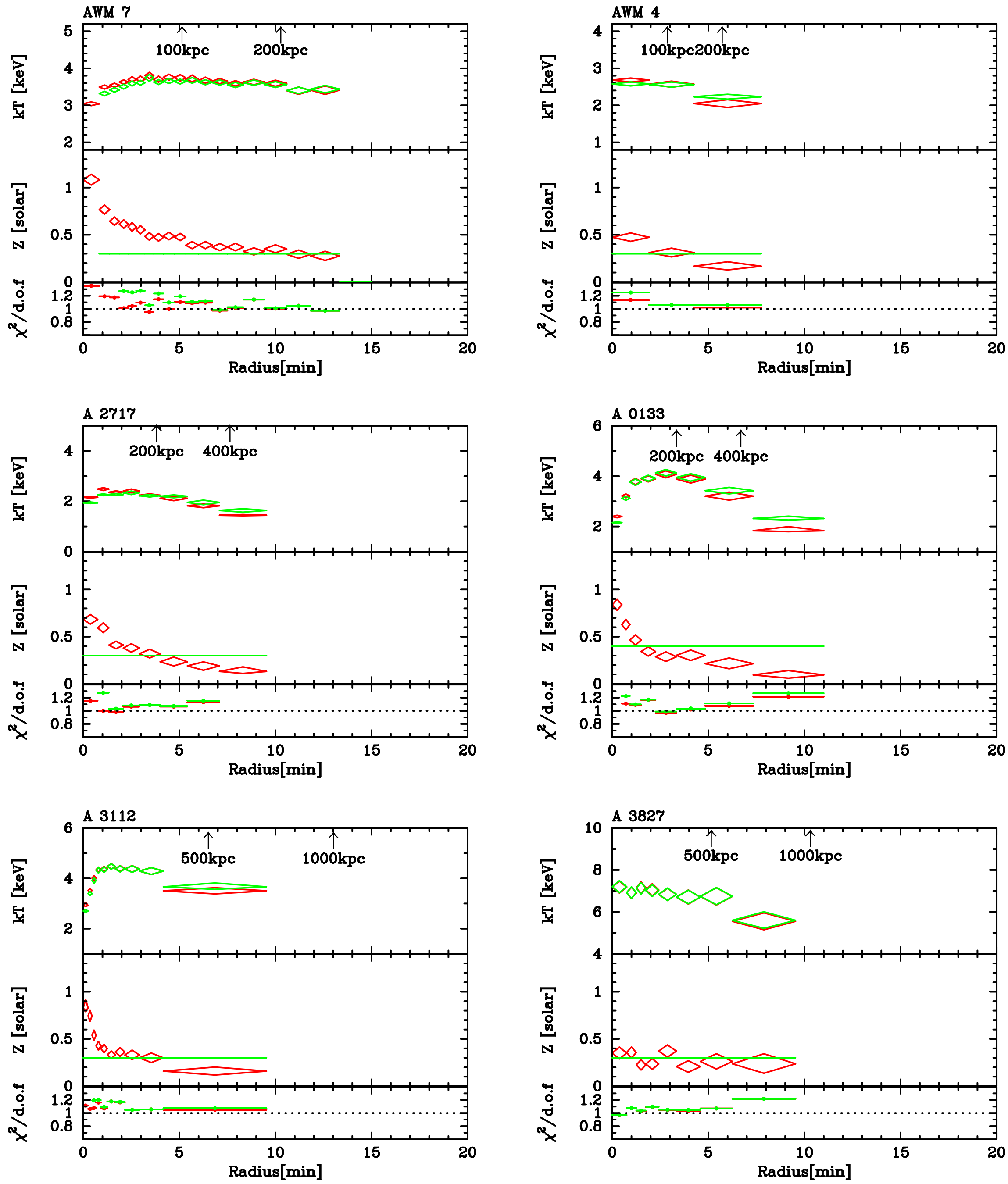

Figure 5.8: Radial distributions of the temperature (top), the metal abundance (middle), and reduced χ^2 value (bottom) of the spectral fits to the concentric annular regions. Each spectrum is fitted with the absorbed MEKAL model in the 0.8-8.0 keV and 0.8-7.5 keV bands for MOS1+2 and pn, respectively. The red and green diamonds show the results with the abundance being set free to vary, and being and fixed at $Z_{\odot}$, respectively.

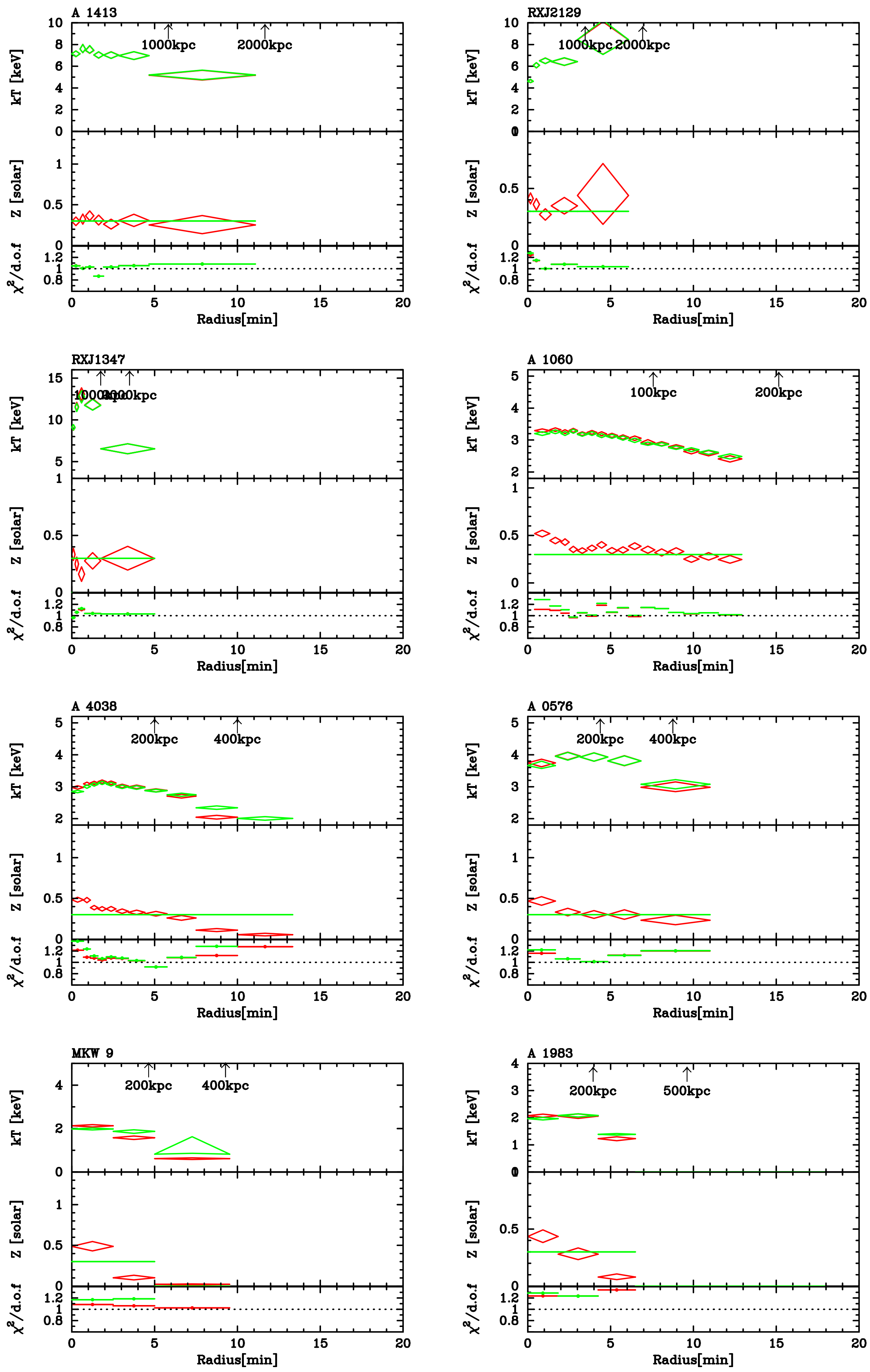

Figure 5.9: Continued.

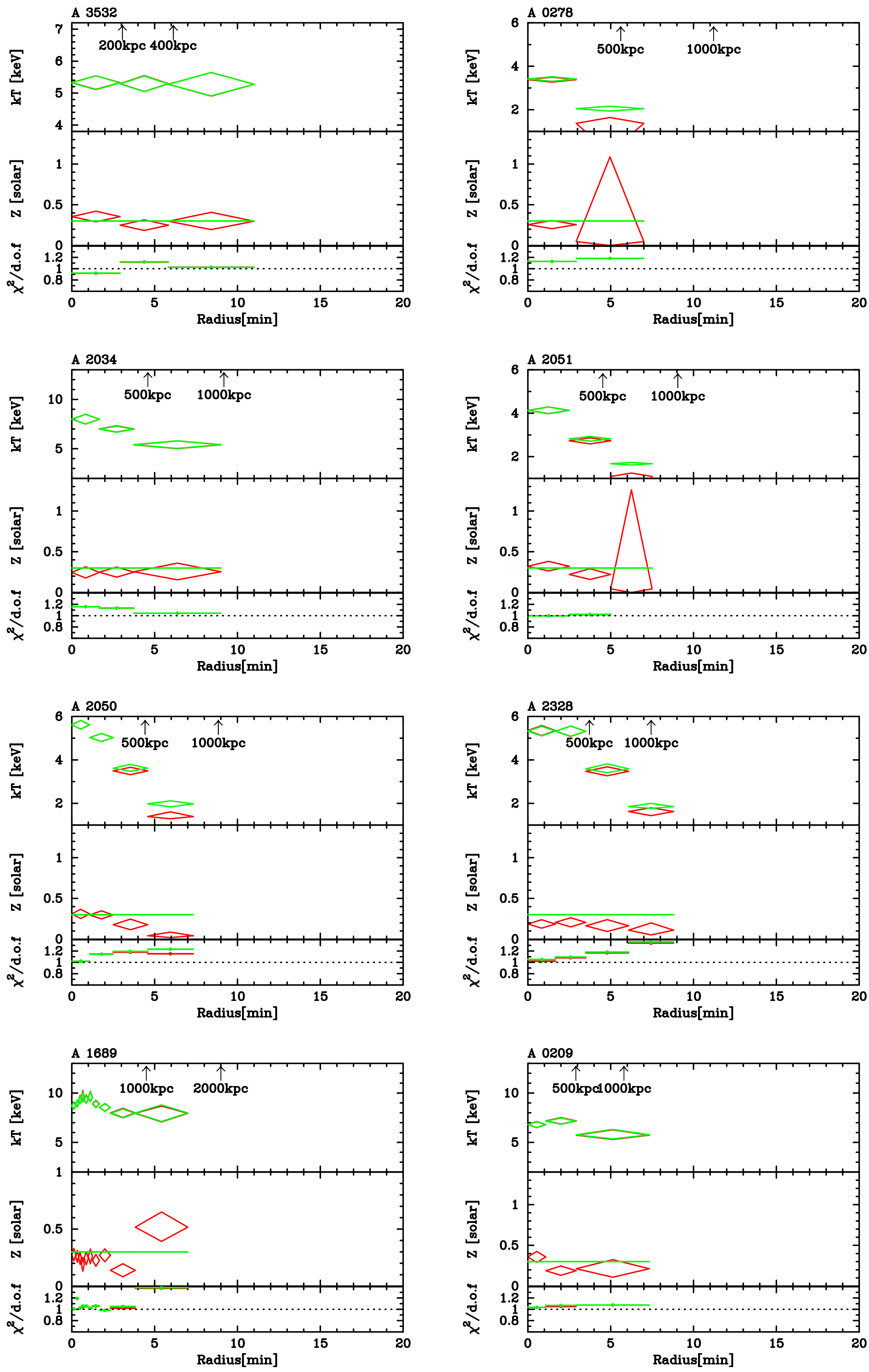

Figure 5.10: Continued.

Chapter 6

Surface Brightness Profile

In §4.4, we derived the background-subtracted and exposure-corected radial surface brightness profile in the energy range of 0.8-3.0 keV for MOS1+2 detectors. In this chapter, we estimate the 3-dimensional density profile based on the radial surface brightness profile assuming spherical symmetry, and then we calculate the gravitational mass profile based on the equation 2.31. We also try to calculate the gravitatinal mass profile through fitting the SSM-model to the radial density profiile.

6.1 Temperature and abundance dependence

First of all, we explain why we utilize the energy range 0.8-3.0 keV to create the radial surface brightness profile. As discussed in §2.3, the X-ray emission from an ionized plasma of ICM, which is described with a combination of thermal bremsstrahlung emission and line emission from heavy elements, depends on the ICM density, the temperature, and the abundance. Study of the hot gas density through the ICM brightness profile is generally carried out under the assumption of uniformity of the temperature and the abundance. In other words, we assumed that the surface brightness is dependent only on the square of electron density (see §2.3). However, the actual galaxy clsuters have radial dipendence on these parameters.

The *ROSAT* observatory had allowed us to study the diffuse X-ray emission from the cluster systematically. However, *ROSAT* could not measure the ICM temperature accurately, because it is only sensitive to the soft 0.1 keV-2 keV band. Figure 6.1 (top) shows the temperature dependence of the source flux estimated by simulations using XSPEC software with the absorbed MEKAL model in the various energy ranges. We adopted the parameter values of A 1060 for the emssion measure, the metal abundance ($= 0.41 Z_\odot$), and $N_\mathrm{H} (= 4.9 \times 10^{20} \mathrm{cm}^{-2}$. Even if the temperature changes, the flux is almost constant if the temperature exceeds 2 keV, which condition is satisfied for all of our cluster samples (table 5.2), when we adopt the energy bands 0.8-3.0 keV. To demostrate this, we plot the energy spectrum of the absorbed MEKAL model with a common abundance and emission measure against the various temperature in figure 6.1 (bottom). When the temperature rised, the spectrum becomes flat gradually. Especially, the change is large in the band above 3.0 keV. Thus, as long as we limit the energy range to 0.8-3.0 keV, the surface brightness is certainly constant, irrespective of the ICM temperature.

In addition, we check the metal abundance dependence of the source flux. Figure 6.2 shows the metal abundance dependence against the various temperature samples in the energy band 0.8-3.0 keV. The steep dependence of the flux againt the metal abundance is remarkable for the plasma with $kT = 1$ keV. As recognized from figure 6.1 (bottom), this

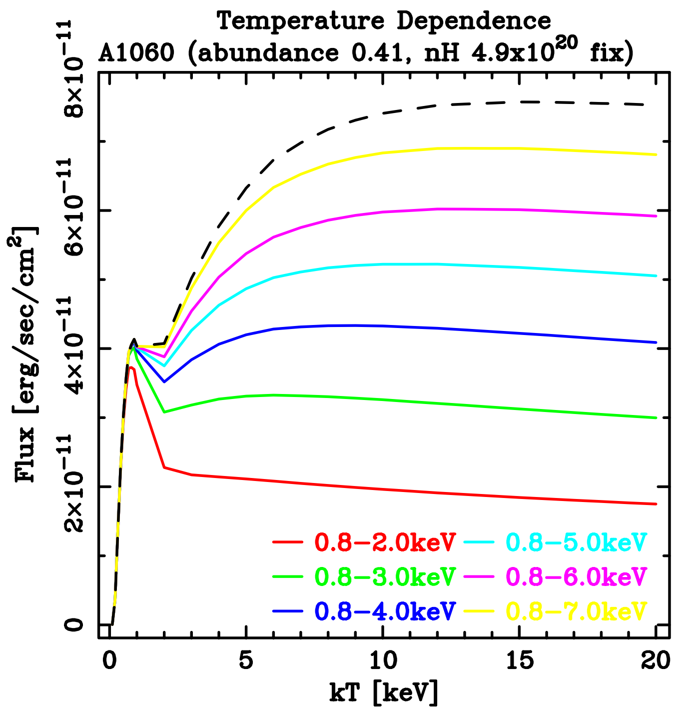

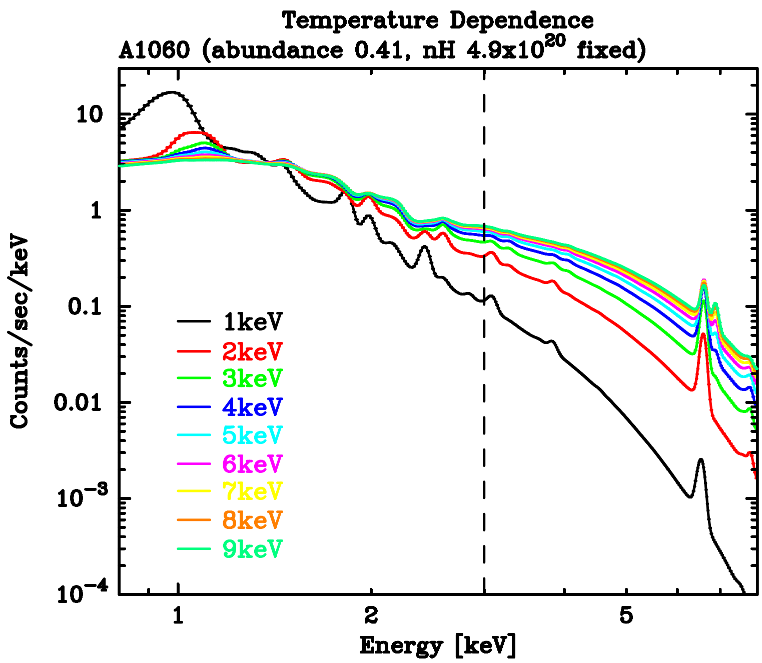

Figure 6.1: The top figure shows the temperature dependence of the source flux in various energy ranges. The flux was simulated by the XSPEC software with the absorbed MEKAL model by adopting the parameter values of A 1060. The bottom figure shows the source spectrum for the various temperatures. The dashed line represents the X-ray energy 3.0 keV.

is due to the Fe-L line emissions which dominates the spectrum in a temperature range of $kT < 2$ keV. Since the temperature of our sample clusters are almost higher than 2 keV, we can ignore the effect of abundance variation.

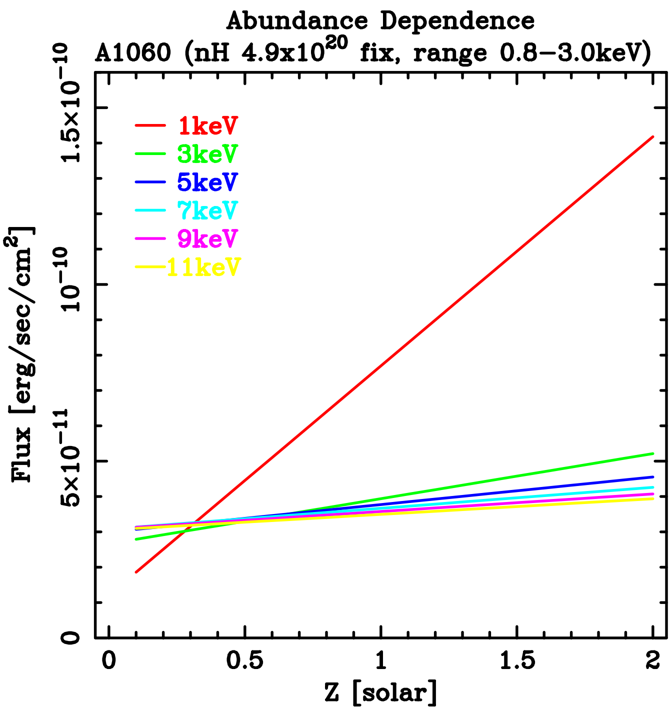

Figure 6.2: The metal abundance dependence of the source flux in the energy range of 0.8-3.0 keV. The spectral parameters other than the temperature are those of A 1060. The flux was simulated by using the XSPEC software with the absorbed MEKAL model.

6.2 β-model fitting

In this section, we analize the X-ray radial profile derived in § 4.4 with the isothermal β-model. The β-model function is written as

$$S(r) = S_0 \left[1 + \left(\frac{r}{r_c} \right)^2 \right]^{-3\beta+1/2}, \tag{6.1}$$

where S_0, r_c and β are the central surface brightness, core radius and the outer slope, respectively. First of all, we tried to fit the β-model to the radial surface brightness distribution (§ 4.4) in the radius range from the center ($r = 0$) to R_{out} where the signal to noise ratio is reduced to 1. The results of the β-model fits were summarized in figure 6.9-6.11. Table 6.1 shows the R_{out} and the resultant $\chi^2/d.o.f.$ value of the β-model fit. It is clear that the β-model fitting were not accepted by any cluster of our sample.

6.3 Iteration method

It is clear from figure 6.9-6.11 that such unacceptable fits is caused by discrepancey between the model and the data in the central region. The observed surface brightness show excess over the β-model in the central regions. To resolve this problem, a double β-model, the superposition of 2 separate emission components with different β values, is often used. This model is, however, physically difficult to interpret. Therefore, we introduce a new method to estimate the radial brightness and density profile. We explored a solution of a 3-dimensional density structure with a single emission component based on the assumption that the temperature and metallicity are constant with radius, and also

Table 6.1: Summary of the model fit of the surface brightness profile

Cluster	R_{in}	R_{out}	$\chi^2/d.o.f$			
			β-model		SSM-model	
	[$'$] ([kpc])	[$'$] ([kpc])	$0 - R_{out}$	$R_{in} - R_{out}$	$\alpha = 1$	$\alpha = 1.5$
AWM7	5.5 (106.8)	14.0 (271.8)	27.970	1.123	14.648	5.765
AWM4	2.0 (70.0)	9.0 (315.0)	2.131	1.116	2.147	1.150
A2717	2.0 (104.8)	9.5 (497.8)	8.496	1.032	7.903	2.860
A0133	2.5 (147.0)	11.0 (646.8)	11.340	1.532	11.297	7.397
A3112	1.5 (115.2)	9.5 (729.9)	23.696	2.472	17.386	7.081
A3827	2.0 (194.1)	9.5 (922.1)	1.721	0.868	1.893	1.913
A1413	1.5 (197.0)	9.0 (1181.8)	5.828	1.196	5.074	1.264
RXJ2129+0005	1.0 (188.6)	6.0 (1131.6)	6.987	1.604	4.942	1.767
RXJ1347-1145	1.0 (272.2)	5.0 (1360.9)	10.148	1.133	5.061	1.938
A1060	5.0 (65.0)	13.0 (168.9)	3.664	1.737	3.909	1.679
A4038	4.0 (132.5)	13.0 (430.6)	5.827	1.620	6.071	2.572
A0576	3.0 (126.9)	11.0 (465.4)	4.596	0.956	4.594	1.438
MKW9	2.0 (86.2)	9.5 (409.6)	1.916	1.080	1.607	2.145
A1983	2.0 (95.3)	7.0 (333.5)	3.149	1.304	2.748	1.622
A3532	3.0 (175.8)	11.0 (644.7)	1.808	0.829	1.781	1.088
A0278	1.5 (133.8)	7.0 (624.4)	1.591	0.868	1.405	0.898
A2051	1.5 (181.1)	7.0 (845.0)	1.996	1.326	1.338	1.365
A2050	1.5 (237.8)	7.0 (1109.9)	2.664	1.080	2.781	1.541
A1689	2.0 (317.1)	7.0 (1109.9)	49.641	1.473	15.832	2.706
A0209	0 (0)	7.0 (1206.7)	1.499	-	-	-

that the clusters are spherically symmetric, which seem to be a reasonable approximation of the observed features.

In our new method, the outer region is fitted using the β-model, and then the inner region which shows the disagreement is corrected by comparing the observed surface brightness profile with the model profile that is modified iteratively. This procedure is summarized as follows.

1. We first calculate the radial surface brightness profile from the MOS1+2 image in the band 0.8-3.0 keV, after application of the SAS task "evigweight" in order to eliminate the telescope vignetting effect.

2. Under the assumption of constant temperature and spherically symmetric distribution of the ICM, we fit the radial surface brightness profile at an outer region with a single β-model. The fitted range and parameters are summarized in table 6.2.

3. The best-fit β-model is Extrapolated to the center, and the ratio of the data to the model is calculated as a function of the radius. In this process, we employed an Exponential function in approximating the radial profile of the surface brightness ratio.

4. The density of the plasma $\rho(r)$ is enhanced by multiplying the square root of the above ratio, and the new radial profile of the brightness is calculated.

5. The procedures 3 and 4 are repeated until the residual between the data and the model practically vanishes.

These procedure are described in the following subsections in detail.

6.3.1 β-model fitting in the outer region

We fit the radial surface brightness profile at the outer region with a single β-model (eq. 6.1) We define the R_{in} as the minimum inner radius that gives acceptable fit at the range between R_{in} to R_{out}. In doing this, we fitted the β-model to the radial surface brightness profile in various ranges of $R_{in} - R_{out}$, where R_{in} is stepped by $0.5'$, and plotted the $\chi^2/d.o.f.$ values against R_{in}. We adopted the smallest R_{in} that gives acceptable fit to the radial profile as the final value for R_{in}. The R_{in} thus determined and R_{out} are summarized in table 6.1, and the β-model parameters (r_c, β & n_0) which were estimated by the $R_{in} - R_{out}$ range fit are summarized in table 6.2. The resultant profile of β-model fit for all our sample clusters were summarized in figures 6.9-6.11.

Note that a simple β-model gives an acceptable fit to the entire brightness profile of A0209. Accordingly, we do not carry out the following iteration process to A 0209.

Since we do not know how extended the cluster emission is and also the slope parameter,β, and the core radius, r_c, are strongly coupled (fig B.1), the background level and the cluster parameter depend on the outer radius of the fitting area, R_{out}, if the fitting radius is too small. If R_{out} is too small, the background level determined from the fit tends to be over-ore underestimated and results in uncertain r_c and β. Thus we plot the β against the r_c/R_{out} in figure 6.3 to check this effect. As shown in this figure, the β value againset the r_c/R_{out} was not shown the significant correlation. Thus we conclude that the β value is appropriately obtained for all our samples.

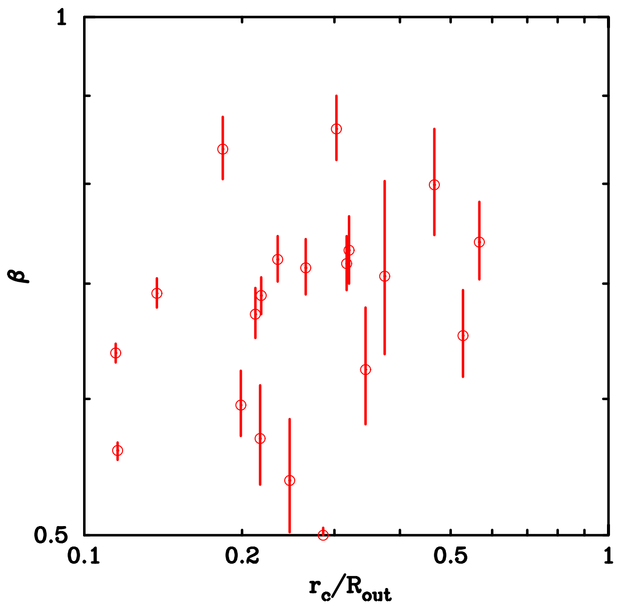

Figure 6.3: β value against the r_c/R_{out}.

Table 6.2: Parameters from the β-model fit at outer region

Cluster	r_c		β	n_0(before)	n_0(after)
	[$'$]	[kpc]		[cm^{-3}]	[cm^{-3}]
AWM7	$7.94^{+0.62}_{-0.58}$	($154.1^{+12.0}_{-11.2}$)	$0.740^{+0.041}_{-0.036}$	$3.60^{+0.14}_{-0.13} \times 10^{-3}$	$1.95^{+0.16}_{-0.08} \times 10^{-2}$
AWM4	$1.79^{+0.30}_{-0.30}$	($62.6^{+10.5}_{-10.6}$)	$0.595^{+0.028}_{-0.024}$	$5.18^{+0.99}_{-0.65} \times 10^{-3}$	$1.75^{+0.75}_{-0.37} \times 10^{-2}$
A2717	$2.51^{+0.21}_{-0.21}$	($131.6^{+11.1}_{-10.8}$)	$0.715^{+0.028}_{-0.025}$	$2.92^{+0.20}_{-0.17} \times 10^{-3}$	$1.83^{+0.34}_{-0.18} \times 10^{-2}$
A0133	$2.33^{+0.26}_{-0.26}$	($137.1^{+15.2}_{-15.1}$)	$0.672^{+0.024}_{-0.021}$	$4.50^{+0.52}_{-0.40} \times 10^{-3}$	$5.74^{+0.59}_{-0.31} \times 10^{-2}$
A3112	$1.09^{+0.08}_{-0.08}$	($83.8^{+6.1}_{-6.3}$)	$0.638^{+0.008}_{-0.008}$	$14.05^{+0.13}_{-1.05} \times 10^{-3}$	$12.01^{+1.17}_{-0.53} \times 10^{-2}$
A3827	$2.07^{+0.15}_{-0.15}$	($200.5^{+14.8}_{-14.9}$)	$0.689^{+0.017}_{-0.017}$	$5.33^{+0.38}_{-0.33} \times 10^{-3}$	$1.12^{+0.24}_{-0.12} \times 10^{-2}$
A1413	$1.24^{+0.11}_{-0.11}$	($162.5^{+13.9}_{-14.0}$)	$0.691^{+0.014}_{-0.013}$	$8.77^{+0.87}_{-0.70} \times 10^{-3}$	$3.15^{+0.81}_{-0.20} \times 10^{-2}$
RXJ2129+0005	$0.94^{+0.10}_{-0.10}$	($176.4^{+18.1}_{-17.9}$)	$0.723^{+0.023}_{-0.021}$	$9.43^{+1.04}_{-0.81} \times 10^{-3}$	$6.66^{+1.90}_{-0.71} \times 10^{-2}$
RXJ1347-1145	$0.92^{+0.11}_{-0.11}$	($250.0^{+30.1}_{-29.6}$)	$0.838^{+0.037}_{-0.033}$	$17.09^{+2.29}_{-1.71} \times 10^{-3}$	$41.32^{+7.26}_{-0.72} \times 10^{-2}$
A1060	$6.86^{+0.67}_{-0.62}$	($89.2^{+8.7}_{-8.1}$)	$0.653^{+0.041}_{-0.035}$	$3.20^{+0.16}_{-0.14} \times 10^{-3}$	$1.08^{+0.14}_{-0.06} \times 10^{-2}$
A4038	$4.12^{+0.35}_{-0.34}$	($136.3^{+11.6}_{-11.4}$)	$0.719^{+0.027}_{-0.025}$	$4.17^{+0.30}_{-0.25} \times 10^{-3}$	$2.40^{+0.12}_{-0.06} \times 10^{-2}$
A0576	$5.12^{+0.55}_{-0.50}$	($216.6^{+23.2}_{-21.1}$)	$0.799^{+0.062}_{-0.052}$	$2.48^{+0.14}_{-0.12} \times 10^{-3}$	$1.31^{+0.37}_{-0.18} \times 10^{-2}$
MKW9	$2.34^{+0.55}_{-0.51}$	($101.0^{+23.5}_{-22.0}$)	$0.538^{+0.046}_{-0.036}$	$2.04^{+0.42}_{-0.27} \times 10^{-3}$	$1.45^{+0.34}_{-0.17} \times 10^{-2}$
A1983	$2.62^{+0.61}_{-0.55}$	($124.8^{+28.9}_{-26.1}$)	$0.707^{+0.096}_{-0.070}$	$2.32^{+0.42}_{-0.26} \times 10^{-3}$	$1.23^{+0.36}_{-0.17} \times 10^{-2}$
A3532	$3.78^{+0.66}_{-0.61}$	($221.8^{+38.6}_{-35.7}$)	$0.624^{+0.054}_{-0.044}$	$2.15^{+0.27}_{-0.20} \times 10^{-3}$	$0.75^{+0.32}_{-0.16} \times 10^{-2}$
A0278	$1.52^{+0.33}_{-0.34}$	($135.2^{+29.4}_{-29.9}$)	$0.569^{+0.042}_{-0.034}$	$2.48^{+0.60}_{-0.33} \times 10^{-3}$	$1.09^{+0.21}_{-0.24} \times 10^{-2}$
A2051	$1.33^{+0.13}_{-0.10}$	($160.8^{+15.4}_{-12.5}$)	$0.500^{+0.005}_{0}$	$2.86^{+0.30}_{-0.25} \times 10^{-3}$	$0.71^{+0.17}_{-0.19} \times 10^{-2}$
A2050	$1.83^{+0.19}_{-0.19}$	($290.1^{+30.8}_{-29.9}$)	$0.732^{+0.034}_{-0.032}$	$4.18^{+0.37}_{-0.31} \times 10^{-3}$	$1.10^{+0.26}_{-0.17} \times 10^{-2}$
A1689	$1.71^{+0.21}_{-0.21}$	($270.4^{+32.9}_{-32.8}$)	$0.861^{+0.039}_{-0.035}$	$7.47^{+1.04}_{-0.76} \times 10^{-3}$	$5.13^{+0.17}_{-0.09} \times 10^{-2}$
A0209	$0.81^{+0.03}_{-0.03}$	($139.6^{+5.5}_{-5.3}$)	$0.560^{+0.006}_{-0.007}$	$8.67^{+0.25}_{-0.25} \times 10^{-3}$	-

6.3.2 Iteration process

In the previous subsection we could fit the β-model to the radial surface brightness profile in the outer range. In this subsection, we estimate the profile of the inner region which was ignored by the β-model fit based on the iteration process. Here, we explain the iteration process , using the case of A 1060 as an example. Figure 4.5 show the projected radial surface brightness and deprojected radial density profiles of A 1060.

We took the ratio between the surface brightness (Σ) data and the single β-model. which is adout 1.8 at the center, and drops to unity at $r = 4'$. Since the emissivity scales as the square of the density, we took the square root of the brightness ratio, i.e. $\mu = \sqrt{\Sigma_{data}/\Sigma_{\beta}}$, which varies as a function of the radius, and used it as a correction factor to the β-model density. The β-model density profile was calculated by eq. 2.43. The β-model density profile was multiplied by μ, and the predicted brightness profile was compared with the data. In this process, the ratio as a function of the radius was approximated by the sum of an exponential function and a constant, which was found to give a good fit to the observed profile. The brightness and density profiles at this stage are shown by the 1st dashed curves from the bottom (solid line) of figure 4.5. The resultant brightness profiles became steeper than the pure β case, but not as sharp as the data, because our correction factor is "diluted" by the emission in the cluster outskirts superposed in the line of sight. This corrected β-model was substituted for the previous β-model, and we took the ratio of the surface brightness again and calculated further correction factors in the same manner for each radius. This iteration process was continued until the brightness profile gives an acceptable χ^2 value to fit the data. This took 6 iteration steps. The resultant profile is shown in the top curve (green line) of figure 4.5. The 3-dimensional density profile now shows a fairly sharp peak in the center, with a density about twice as much as that of the β-model (top green solid curve in the right panel of figure 4.5). We use this density profile to estimate the physical parameters in the core region in the later section. Each iterated stage for the surface brightness and the radial density profile of all our samples were summarinzed in figure 6.12-6.16.

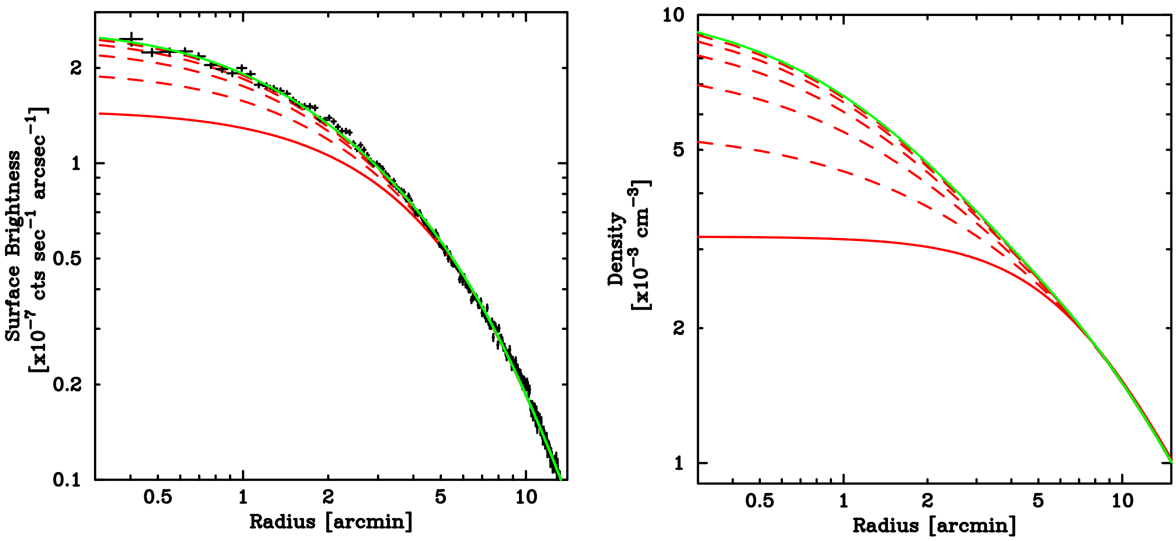

Figure 6.4: Radial distribution of the surface brightness (left) and density (right) in the case of A 1060. The data points are indicated by crosses, The model approaches the observed data by iteratively enhancing the central density. The solid red (green) line corresponds to the initial (6th iterations) profile. The dashed lines represent the iteration between the second and the 5th process.

In figure 6.5, we plot the resultant central electron density n_0 (after) against the initial electron density n_0 (before) for all our samples. This figure shows that the central density was grown by a factor of about $\sim$5.4 after the iteration process.

6.3.3 Decision of the central position

As discussed in §4.4, we estimate the radial surface brightness assuming that the morphological center coincides with the luminosity peak. Since our sample clusters show good spherical symmetry and a clear core at the center, this assumption seems reasonable. We, however, try to make sure the coincidence of the luminosity peak and the contour center, where the contour center was chosen as the central position of the contour at $r = 5'$. As a result, these two positions show good agreement except for the two clusters, AWM 7 and A 3532. We thus study the effect of the choice of the center on the resultant of radial profile fits, by comparing the profiles calculated based on these two center positions for

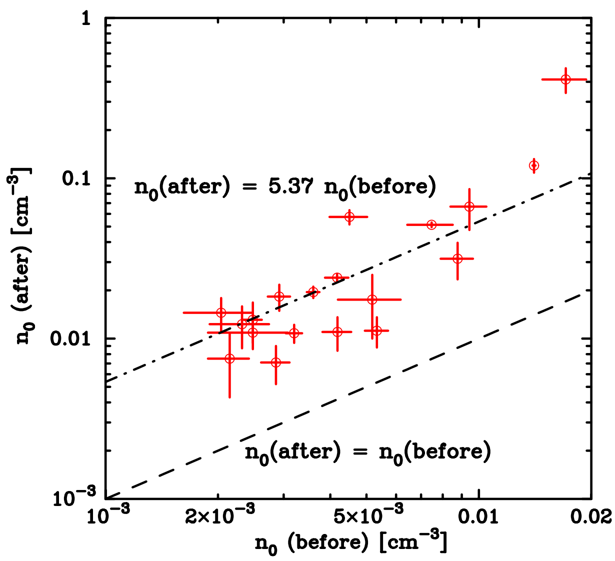

Figure 6.5: The final electron density at the cluster center against the inital density which was obtained by the β-model. The dashed line shows the line of n_0 (before) being equal to n_0 (after).

AWM 7 and A 3532. Figure 6.6 shows the results. Both profiles show disagreement at the central region ($r < 1^{'}$), but the profile in the outer region is almost consistent. In addition, we fit the β-model to these profiles. Table 6.3 shows the resultant parameters. We found the β-model parameters are consistent with each other within the statistical errors for both clusters.

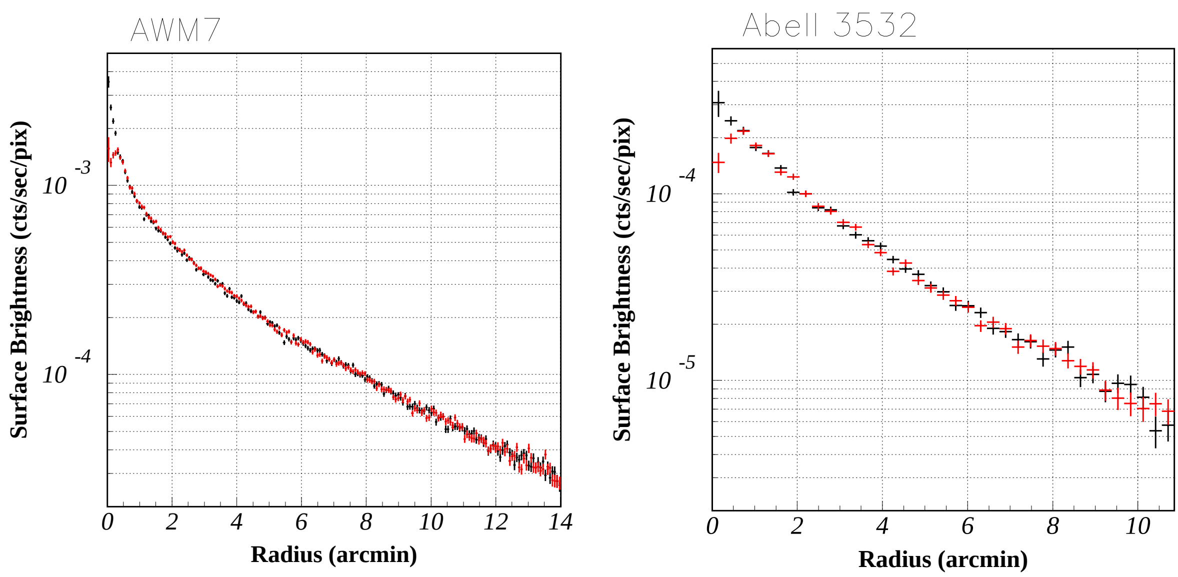

Figure 6.6: Radial surface brightness profile of AWM 7 (left) and A 3531 (right) using two different center positions. The black and red crosses represent the the radial profile centered on the luminosity peak and contour center, respectively.

Table 6.3: The β-model parameter estimated by the peak shifted radial profiles

			peak		contour center	
Cluster	offset	region	r_c [$'$]	β	r_c [$'$]	β
AWM 7	$\sim 20''$	all	$1.83^{+0.05}_{-0.04}$	$0.438^{+0.003}_{-0.03}$	$1.90^{+0.04}_{-0.04}$	$0.444^{+0.003}_{-0.003}$
		outer	$7.62^{+0.86}_{-0.78}$	$0.717^{+0.056}_{-0.046}$	$7.10^{+0.82}_{-0.76}$	$0.689^{+0.051}_{-0.043}$
A 3532	$\sim 54''$	all	$2.05^{+0.20}_{-0.18}$	$0.501^{+0.018}_{-0.016}$	$2.30^{+0.18}_{-0.17}$	$0.524^{+0.019}_{-0.017}$
		outer	$3.95^{+1.03}_{-0.90}$	$0.636^{+0.092}_{-0.067}$	$2.76^{+0.95}_{-0.88}$	$0.553^{+0.065}_{-0.049}$

6.3.4 Mass distribution

Based on an approximation of constant temperature and metalicity as well as spherical symmetry, we have derived the density distribution in a model-independent way. Compared with the single β-model that can fit the data at the outer region for each clusters, the central gas density is ~5.6 times higher (figure 6.5). If the ICM is in hydrostatic equilibrium, the observed high density of the gas simply indicates a concentation of the gravitational mass. Assuming an isothermality for simplicity, we have derived a gravitaional mass profile within a given radius based on the eq. 2.31. The resultant mass profile of A 1060 as an example is shown along with the gas mass profile in figure 6.7a (all mass profile of our samples are summarized in the panel (a) of figure 6.20-6.24). The corresponding mass density profiles are also shown in figure 6.7 and figure 6.20-6.24. In these figures, the mass profiles for a single β-model are plotted for comparision. Since this feature may have resulted from the neglection of the temperature variation, we also plot a mass curve reflecting the temerature varitation. The results are shown by diamonds in the same figures.

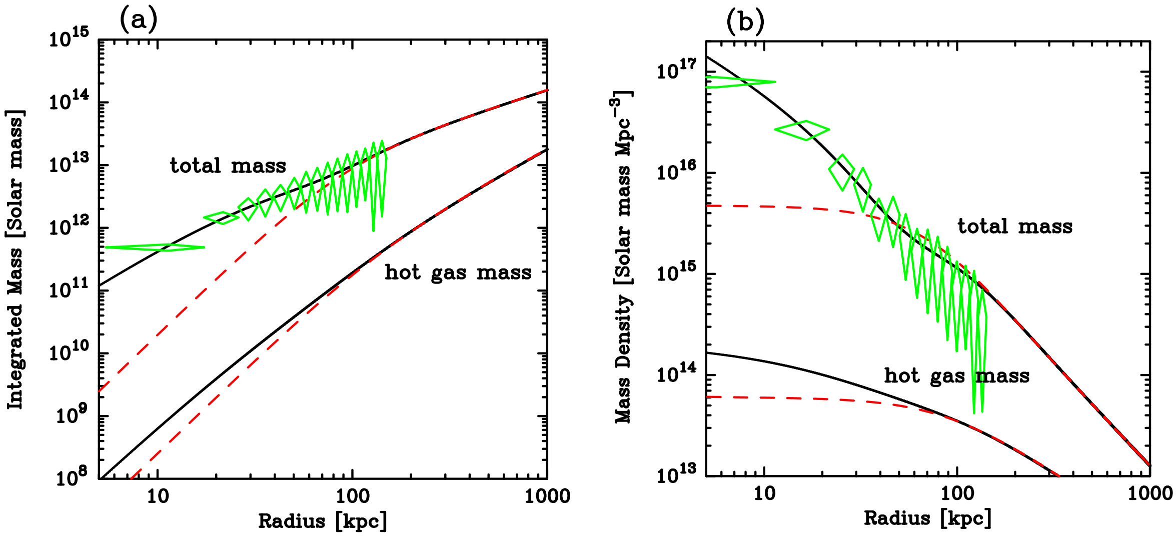

Figure 6.7: (a) Gravitational mass profile estimated from the single β-model (upper dashed line) and the density profile shown in figure 6.4 right (upper solid line). The lower lines represent the ICM mass based on the β-model and the density profile in figure 6.4 right, respectively. The diamonds show the results when the temperature variation is considered. (b) Same as (a), but for the differential mass density profiles.

As shown in 6.7(b), the mass density profile drops slightly around $r = 60 - 100$ kpc. This feature is confirmed in many of our samples, especially for A 133, A 576 and A 3112. Since our sample clusters are already well relaxed this dent feature does not seem real. Since the dent always appears at the boundary between the central excess component and the outer β-model component, our density estimated method (iteration method) does not seem to work correctly around the boundary radius. Except for this region, however, we consider that the overall profile of the mass density is almost correct.

6.4 Universal profile

6.4.1 SSM-model fitting

In this subsection, we fit the SSM-model to the X-ray radial brightness profile. The SSM model is a model representing radial mass distribution of dark matter in a non-equilibrium state, which is suggested by the deviation of the X-ray surface brightness distribution from β-mode. (§6.3). The SSM-model function is written as,

$$S(r) = S_0 \left[1 + \left(\frac{r}{r_s \phi_c} \right)^{\zeta} \right]^{-\eta},$$

for $1 < \alpha < 2$, ,where ϕ_c, ζ and η are expressed as,

$$\begin{aligned} \phi_c &= 0.3(2/\alpha - 1) \\ \zeta &= 0.41 - 5.4(2-\alpha)^6 + (0.585 + 6.47\alpha^{-5.18}) B^{\alpha^6/30} \\ \eta &= -0.68 - 5.09(\alpha - 1)^2 + (0.202 + 0.0206\alpha^8) B^{1.1} \end{aligned}$$

respectively. We use the full detected region ($r = 0 - R_{out}$) in the model fit. Although the SSM-model has 4 free parameters, we first fixed the α with 1, which correspond to the basic NFW profile (Navvarro, Frenk & White (1996)). In the case of the basic NFW profile, the mass density slope become -1 if $r \ll r_s$, and become -3 in the range $r \gg r_s$. Figure 6.8 (left) shows the resultant slope of the fit of A 1060. According to the Moore et al. (1999), central slope of the mass profile became -1.5 based on the detailed numerical simulation. Accodingly, we fixed the α with 1.5 next. In this model, the mass density slope become -1.5 in the radius range $r \ll r_s$, and become -3 where $r \gg r_s$. The slope is steeper than the NFW model only the central region. Figure 6.8 (right) shows the resultant slope of the fit of A 1060. It seems that the SSM-model with $\alpha = 1.5$ describes the observed brightness profile better than that with $\alpha = 1$. The $\chi^2/d.o.f$ values are 3.909 and 1.679, respectively. The resultant $\chi^2/d.o.f.$ values of the SSM-model fitting for all our sample clusters were summarized in table 6.1. Most of the clusters of our samples show the best-fit when we adopt the SSM-model with $\alpha = 1.5$. The resultant profile of the fits with the three models in table 6.1 were summarized in figure 6.17-6.19.

6.4.2 Mass profile estimated from the SSM-model

In the previous subsection, we found that the SSM-model with $\alpha = 1.5$ discribe best the observed radial surface brigntness profiles of all our samples. Here we estimate the corresponding mass density profile based on the resultant parameter, B and r_s. In the range $1 \leq \alpha \leq 2$, the universal mass density profile is described as follows.

$$\rho_{mass}(x) = \frac{\delta_c \rho_{crit}}{x^\alpha (1+x)^{3-\alpha}}, \quad x \equiv \frac{r}{r_s},$$

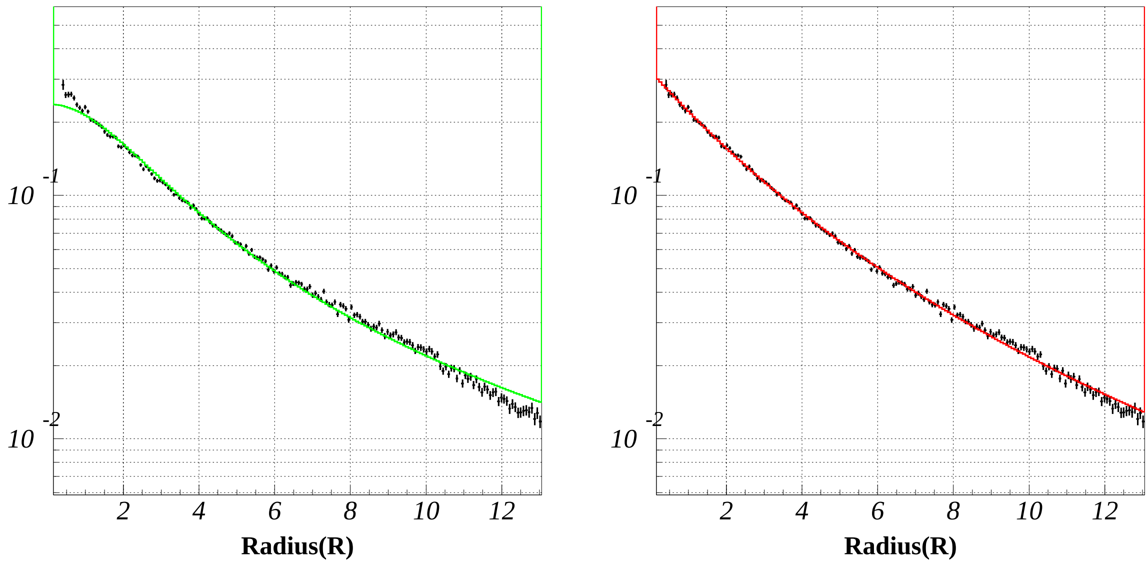

Figure 6.8: Results of SSM-model fitting in case the of A 1060. Left and right figure shows the SSM-model with $\alpha = 1$ and $\alpha = 1.5$ respectively.

where ρ_{crit} is the critical density of the universe at $z = 0$, and δ_c and r_s are the concentration parameter and the scaled radius. Here the δ_c is represented as follows.

$$B = \frac{4\pi G\mu m_p \delta_c \rho_{crit} r_s^2}{kT}$$

where all the symbols are used as their ordinary meanings. The values of δ_c and r_s were already estimated. We use the temperature kT which was obtained by the spectral analysis (§5.1). Hence, we can calculate B immediately, and then we can plot the corresponding NFW mass density profile. All of the evaluated parameters of the SSM-model were summarized in table 6.4. We compare the mass density profiles the SSM-model with the profiles of which were derived from the iteration process as discussed in §6.3, in order to check mutual consistency. We plot these mass density profile in figure 6.25-6.27. The profile from the iteration process shows good agreement with the SSM-model with $\alpha = 1.5$ rather than with $\alpha = 1.0$, except for the radius around $r = 0.1\ r_{180}$ and $r > 0.5\ r_{180}$. We will discuss the discrepancy in the inner region in §6.3.4. That in the outer region, on the other hand, caused by the difference of the slope of the mass density models. For $r > 0.5\ r_{180}$, we cannot confirm the slope, because this radius is out of FOV.

Table 6.4: The best-fit parameters of SSM-model ($\alpha = 1.5$)

Cluster	B	r_s [$'$]	(r_s [kpc])	δ_c
AWM7	$5.11^{+0.06}_{-0.06}$	$43.58^{+1.71}_{-1.71}$	($876.0^{+34.4}_{-34.4}$)	$497.95^{-31.78}_{+35.12}$
AWM4	$5.72^{+0.18}_{-0.17}$	$20.30^{+2.18}_{-1.96}$	($710.5^{+76.3}_{-68.6}$)	$521.47^{-82.87}_{+98.09}$
A2717	$5.76^{+0.10}_{-0.11}$	$16.69^{+1.07}_{-1.03}$	($874.6^{-56.1}_{-54.0}$)	$308.54^{-31.06}_{+35.33}$
A0133	$4.76^{+0.03}_{-0.03}$	$4.90^{+0.22}_{-0.21}$	($288.1^{+12.9}_{-12.3}$)	$3662.40^{-288.24}_{+316.65}$
A3112	$5.48^{+0.04}_{-0.04}$	$7.12^{+0.23}_{-0.22}$	($546.8^{+17.7}_{-16.9}$)	$1384.20^{-75.62}_{+80.39}$
A3827	$8.76^{+0.47}_{-0.40}$	$52.67^{+6.41}_{-5.22}$	($4143.3^{+622.4}_{-506.9}$)	$43.76^{-7.10}_{+7.66}$
A1413	$6.90^{+0.13}_{-0.14}$	$17.11^{+0.98}_{-0.94}$	($2246.5^{+128.7}_{-123.4}$)	$179.70^{-15.80}_{+17.55}$
RXJ2129	$6.02^{+0.09}_{-0.09}$	$5.57^{+0.34}_{-0.32}$	($1050.5^{+64.1}_{-60.4}$)	$646.73^{-63.75}_{+71.14}$
RXJ1347	$6.46^{+0.09}_{-0.09}$	$4.14^{+0.24}_{-0.23}$	($1126.5^{+65.3}_{-62.6}$)	$1069.66^{-99.00}_{+109.89}$
A1060	$5.86^{+0.17}_{-0.16}$	$74.72^{+5.67}_{-5.16}$	($971.4^{+73.7}_{-67.1}$)	$383.17^{-42.71}_{+46.95}$
A4038	$5.76^{+0.05}_{-0.05}$	$23.41^{+0.69}_{-0.68}$	($774.9^{+22.8}_{-22.5}$)	$525.23^{-25.48}_{+27.04}$
A0576	$20.0^{-0.61}_{00.00}$	$558.35^{-31.3}_{00.00}$	($23618.2^{+0}_{-1324.0}$)	$2.64^{0.23}_{+0.06}$
MKW9	$4.27^{+0.07}_{-0.07}$	$6.93^{+0.89}_{-0.80}$	($298.7^{+38.4}_{-34.5}$)	$1422.41^{-285.47}_{+364.49}$
A1983	$6.22^{+0.56}_{-0.43}$	$26.49^{+6.90}_{-4.86}$	($1260.9^{+328.4}_{-231.3}$)	$142.57^{-44.68}_{+56.43}$
A3532	$7.40^{+0.71}_{-1.00}$	$83.38^{+16.62}_{-23.78}$	($4886.1^{+973.9}_{-1393.5}$)	$33.21^{-7.90}_{+23.02}$
A0278	$5.12^{+0.20}_{-0.19}$	$12.45^{+2.04}_{-1.74}$	($1110.5^{+182.0}_{-155.2}$)	$218.51^{-50.96}_{+66.33}$
A2051	$4.71^{+0.15}_{-0.13}$	$11.94^{+1.78}_{-1.52}$	($1319.4^{+196.7}_{-168.0}$)	$146.14^{-31.96}_{+40.10}$
A2050	$12.4^{+2.53}_{-1.90}$	$91.04^{+42.19}_{-26.47}$	($10296.6^{+4771.7}_{-2993.8}$)	$8.74^{-3.82}_{+5.93}$
A1689	$7.24^{+0.10}_{-0.11}$	$12.97^{+0.54}_{-0.54}$	($2057.0^{+85.6}_{-85.6}$)	$283.75^{-18.61}_{+20.37}$
A0209	-	-	-	-

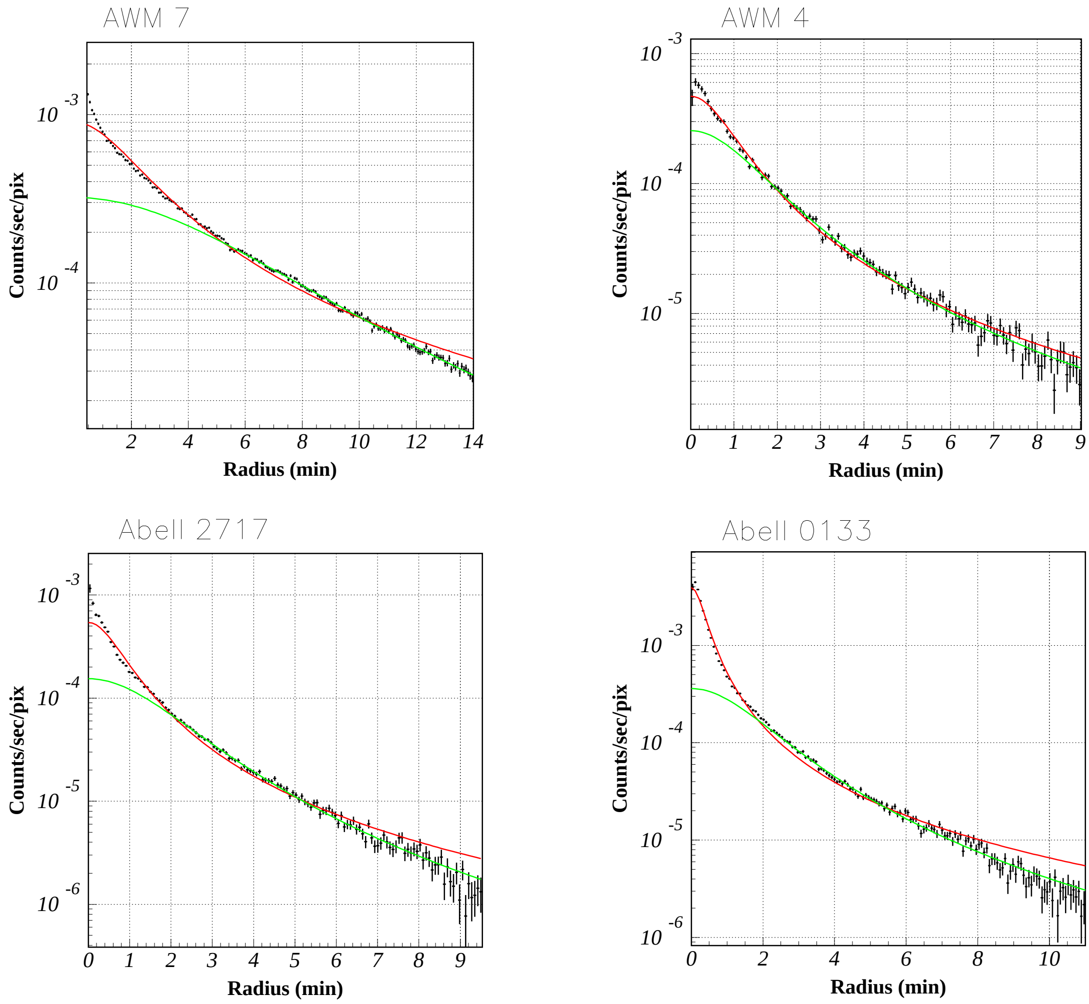

Figure 6.9: Result of isothermal β-model fit of all our sample clusters. We create the surface brightness profile in the energy range 0.8-3.0 keV for MOS1+2 detector within R_{out} centered on the luminosity peak. The R_{out} defines the radius where the signal to noise ratio is reduced to 1. The red and green lines show the results from the β-model fit in the radius 0-R_{out} and R_{in}-R_{out}, respectively. We define the R_{in} as a smallest inner radius when the β-model fit give us an acceptable fit in the range between R_{in} to R_{out}.

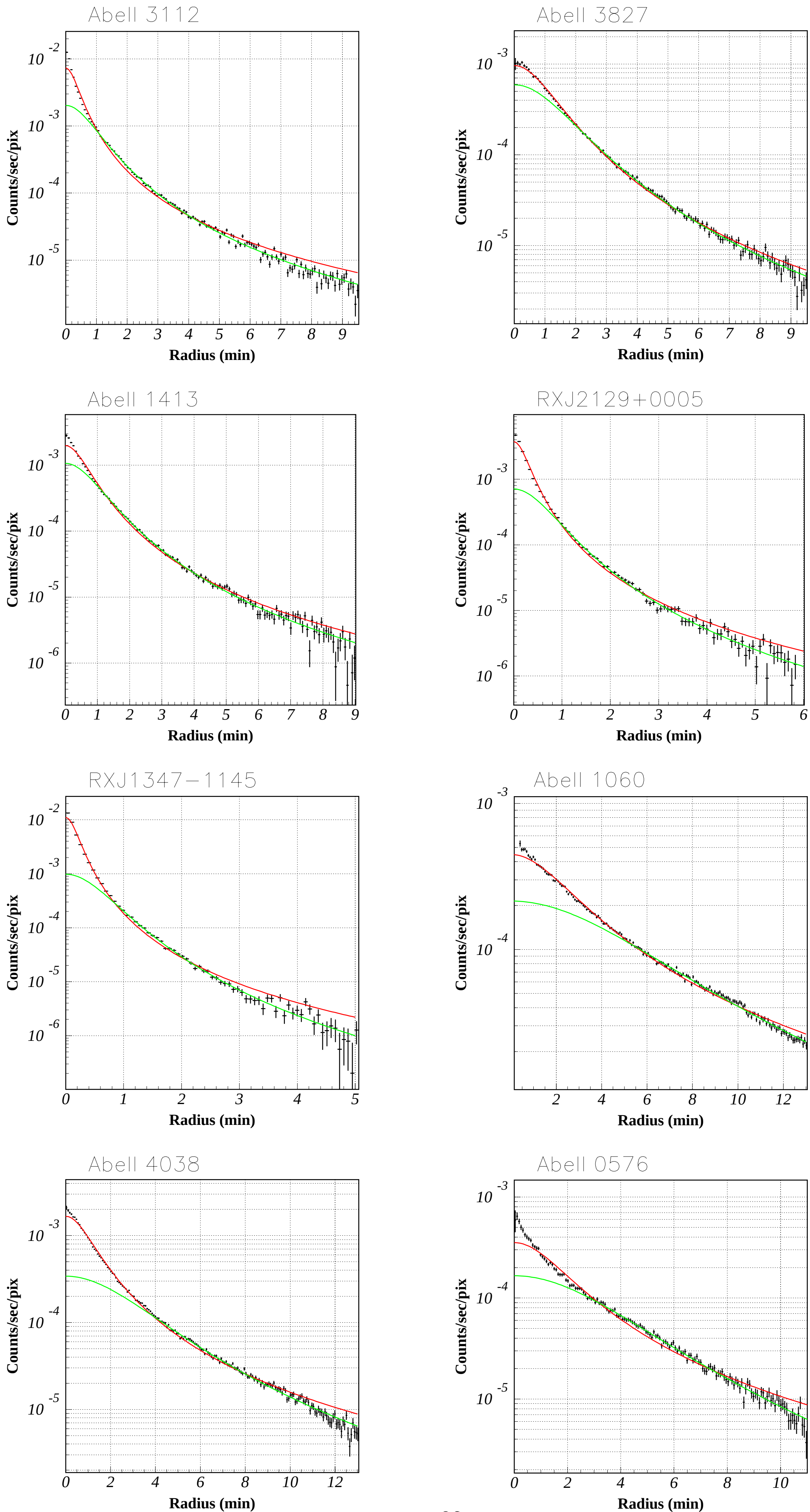

Figure 6.10: Continued.

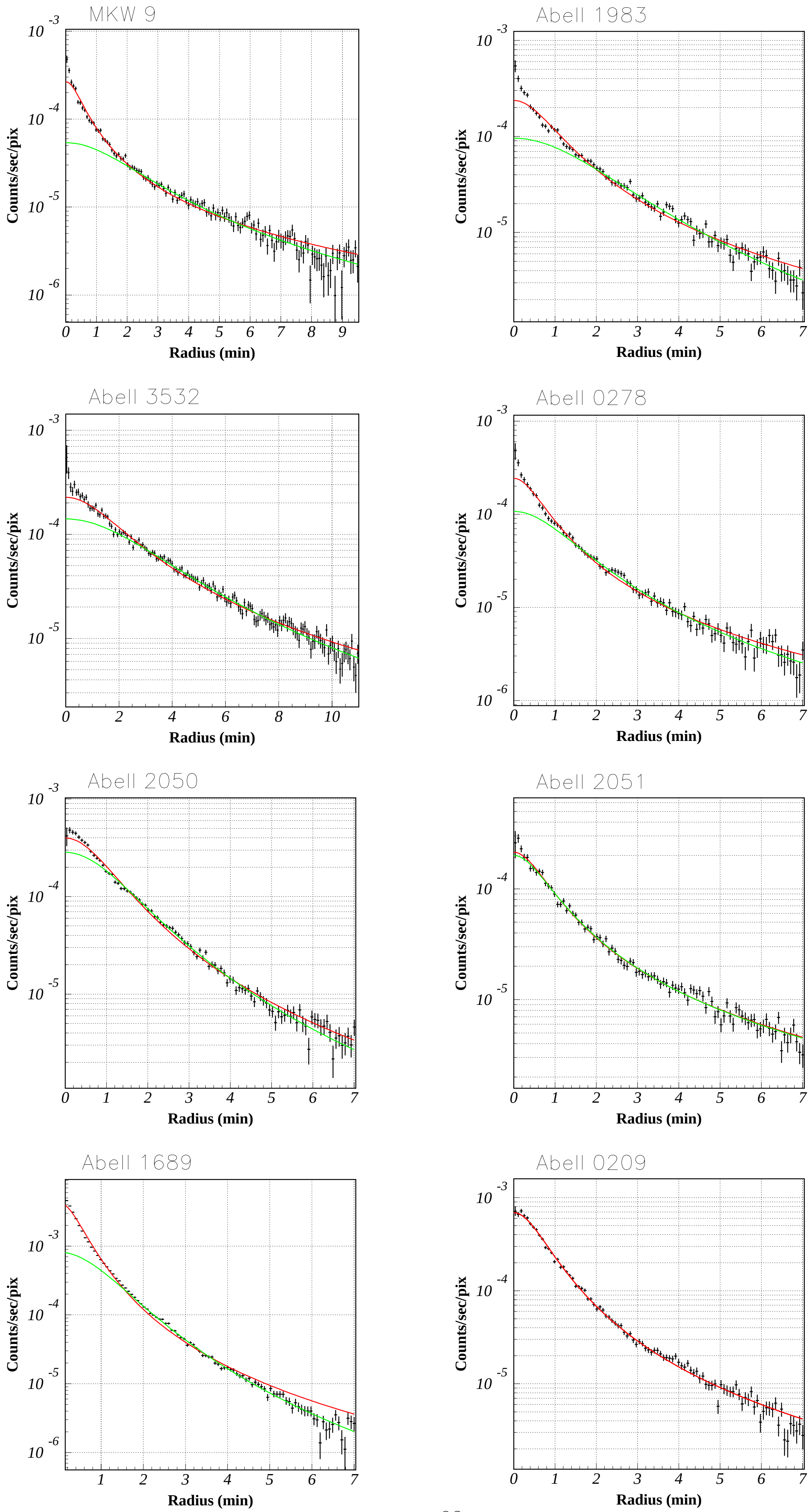

Figure 6.11: Continued.

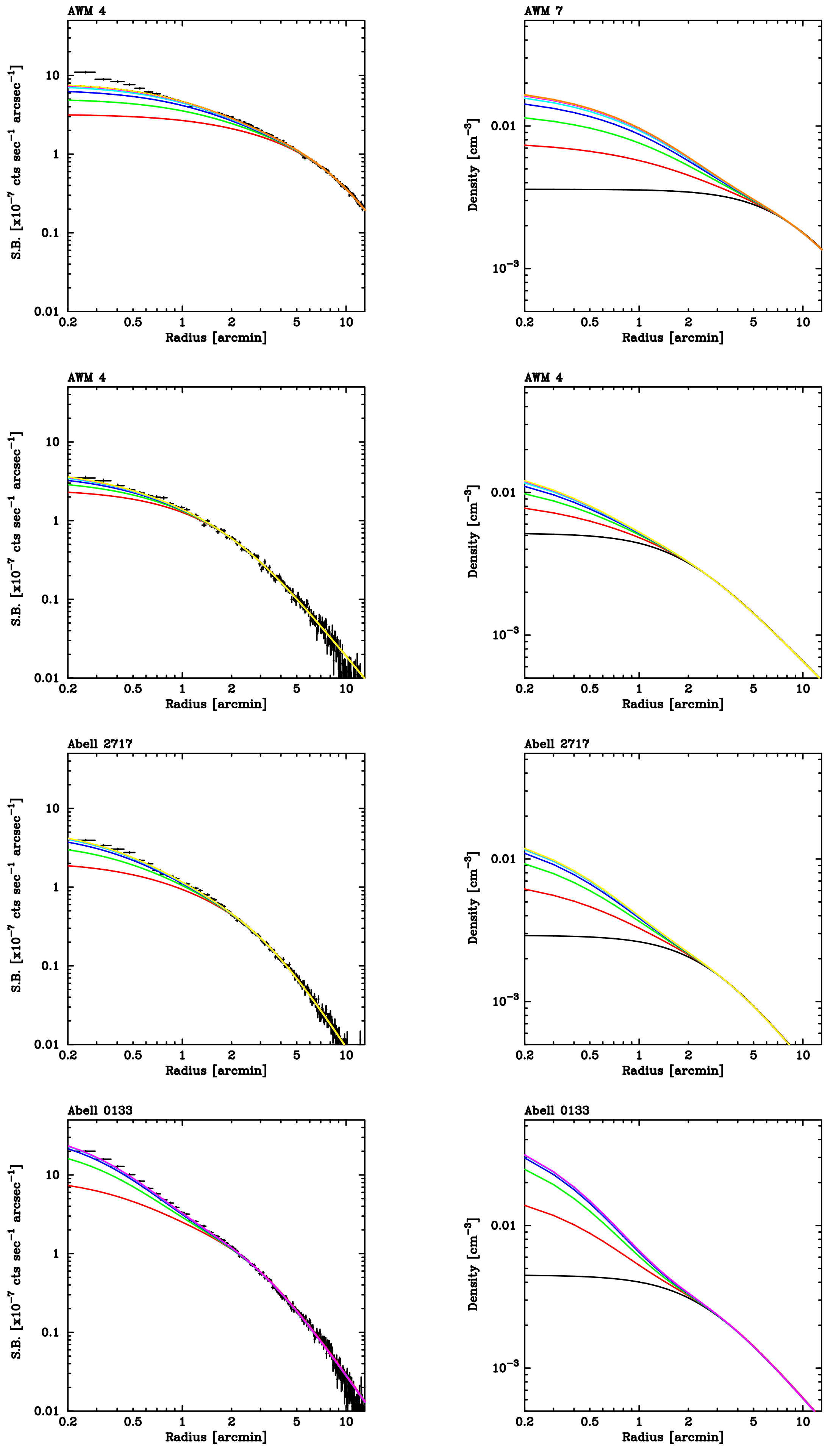

Figure 6.12: Profiles of each iteration stage of the surface brightness (left) and the density (right) for all our sample clusters.

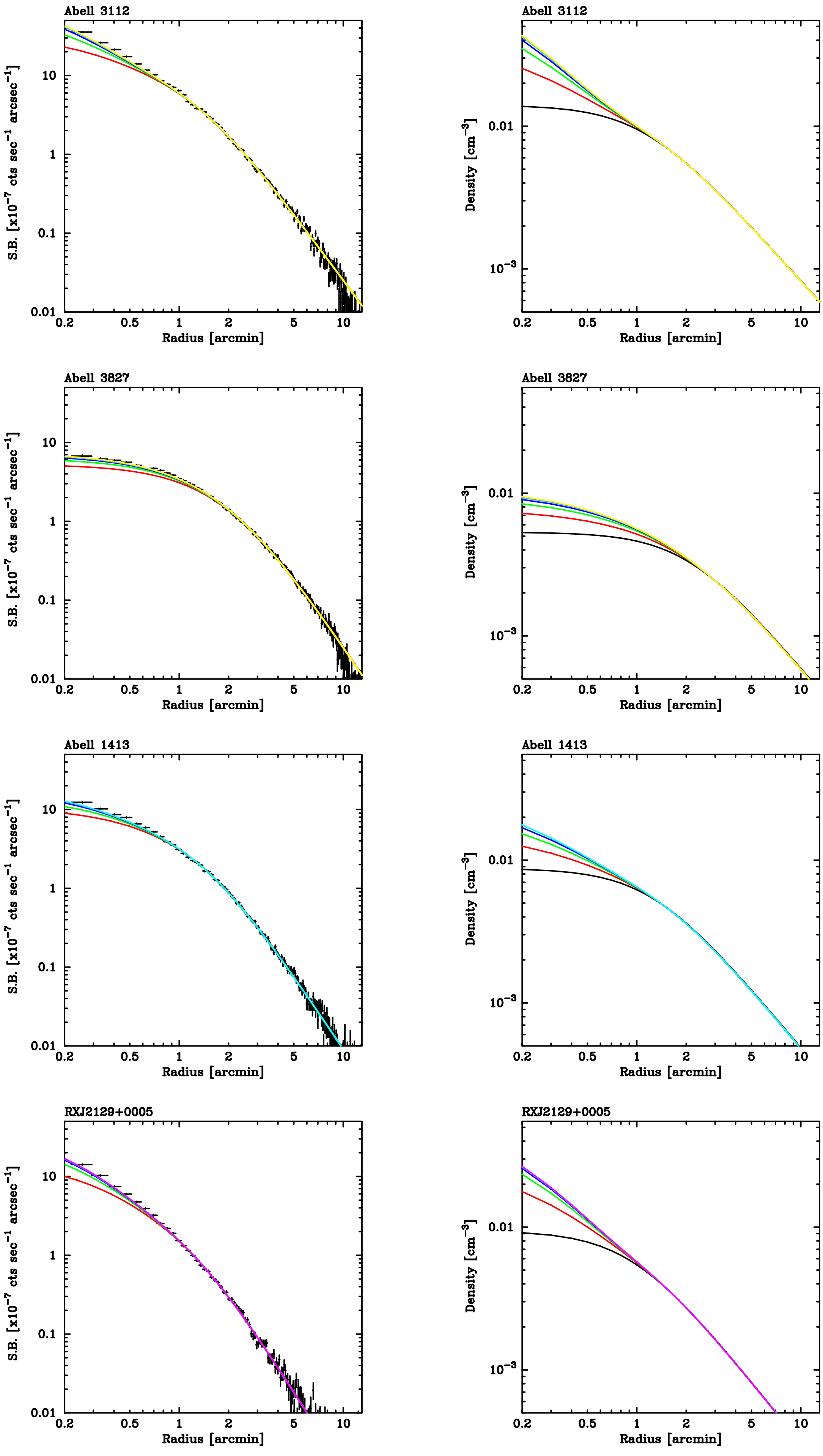

Figure 6.13: Continued.

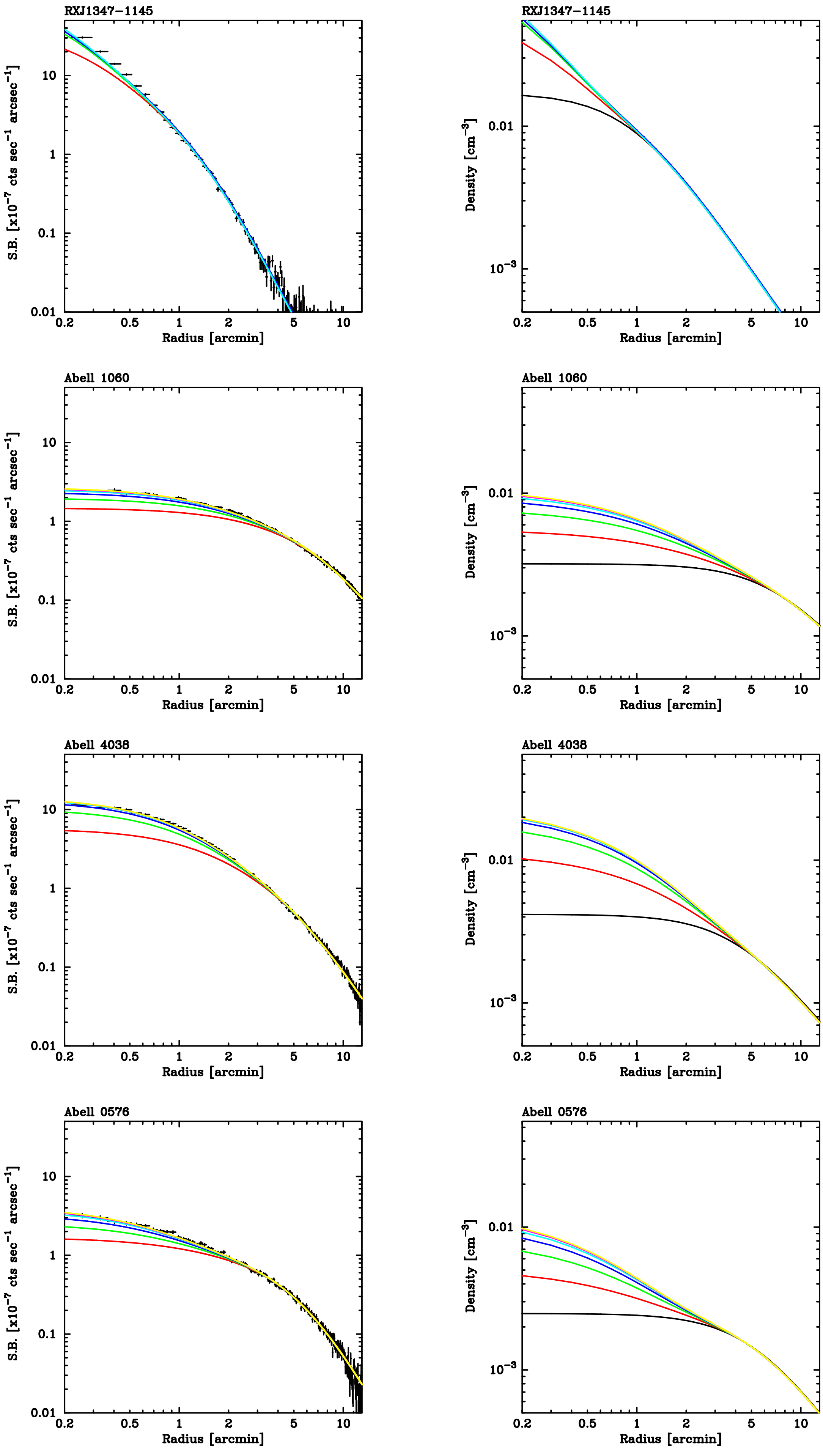

Figure 6.14: Continued.

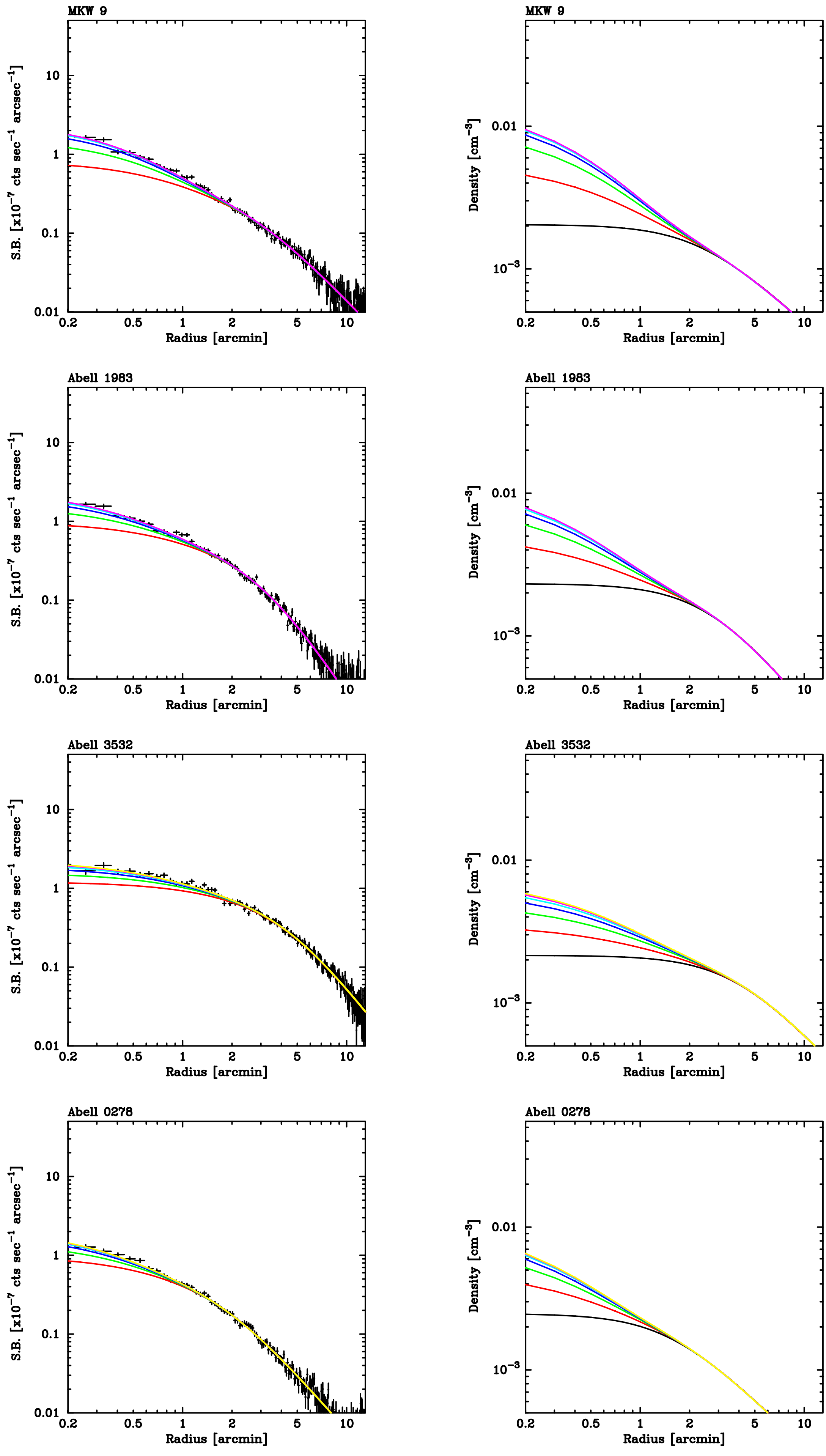

Figure 6.15: Continued.

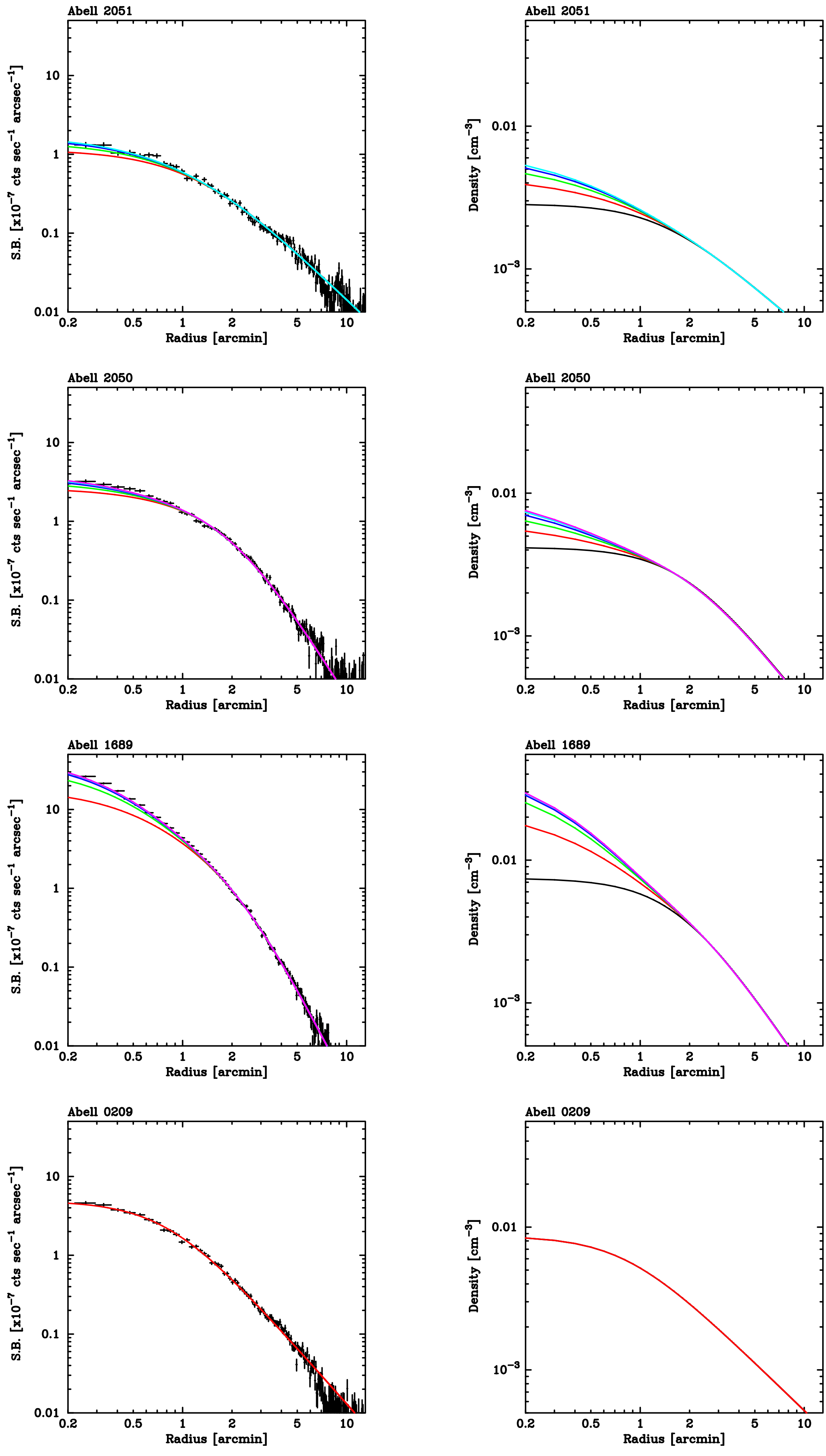

Figure 6.16: Continued.

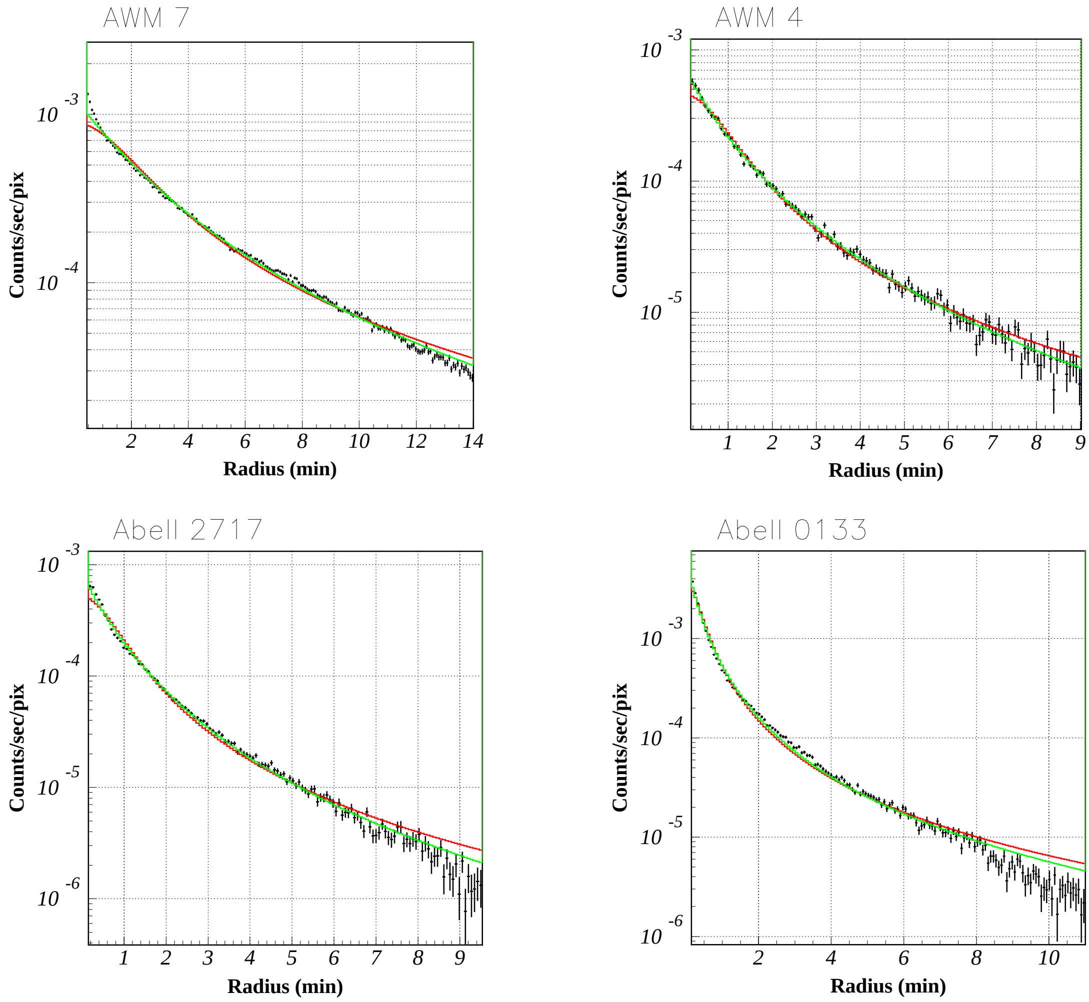

Figure 6.17: Result of the SSM-moedl fit to all our sample clusters. We create the surface brightness profile in the energy range 0.8-3.0 keV for MOS1+2 detectors within R_{out} centered on the luminosity peak. The R_{out} define the radius where the signal to noise ratio is reduced to 1. The red and green lines show the results from the SSM-model fit in the case of $\alpha = 1$ and $\alpha = 1.5$, respectively.

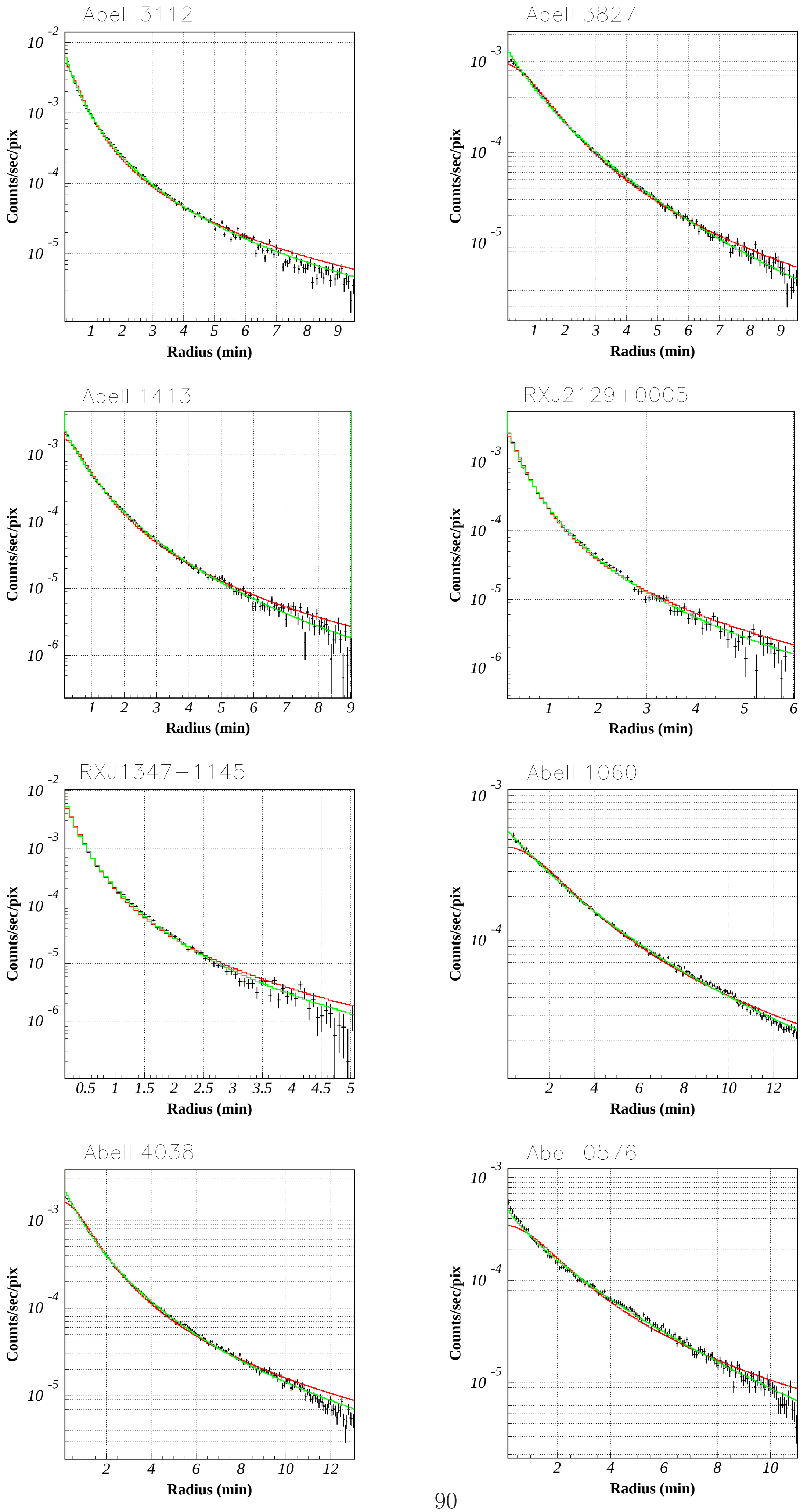

Figure 6.18: Continued.

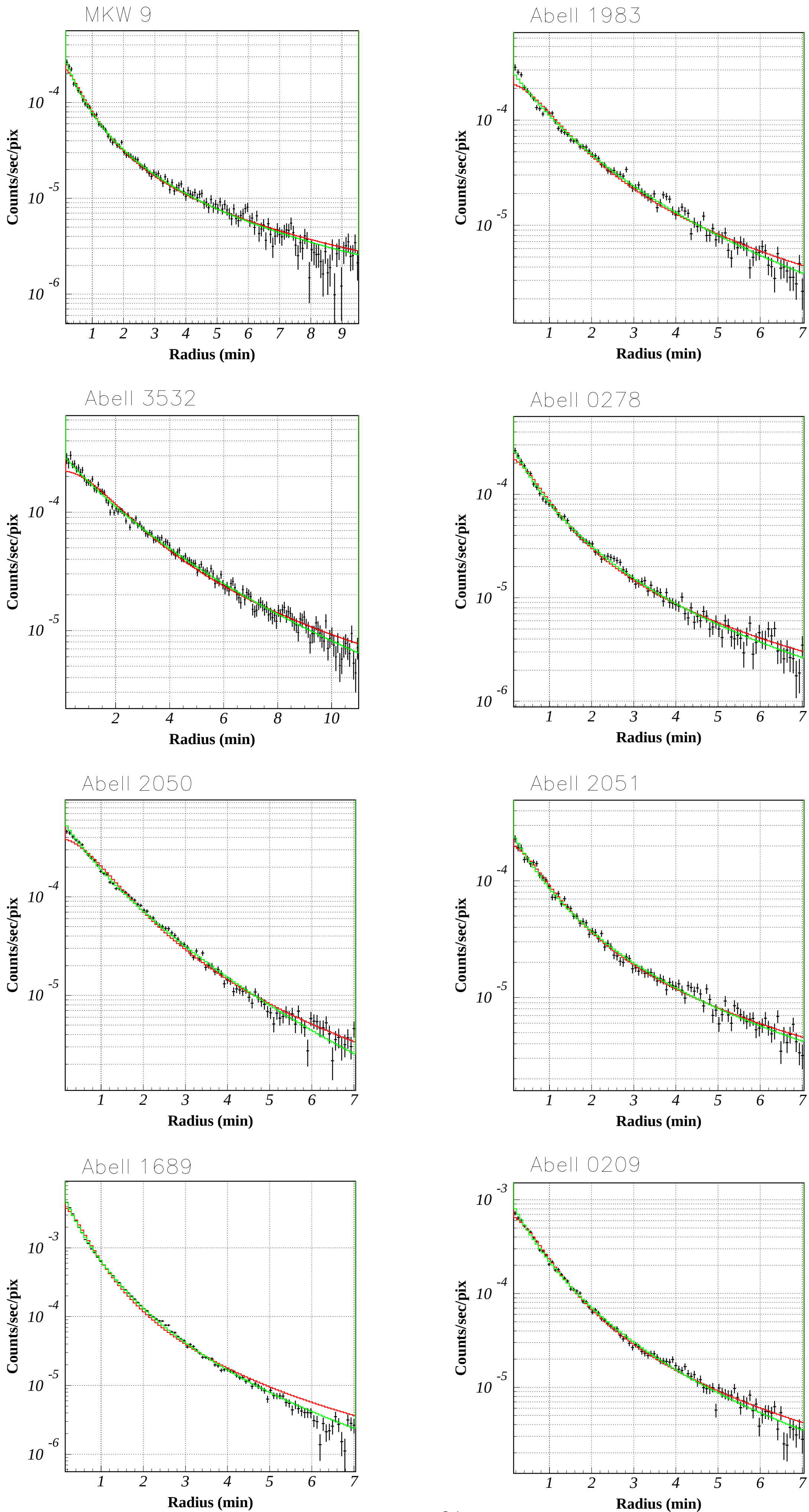

Figure 6.19: Contnued.

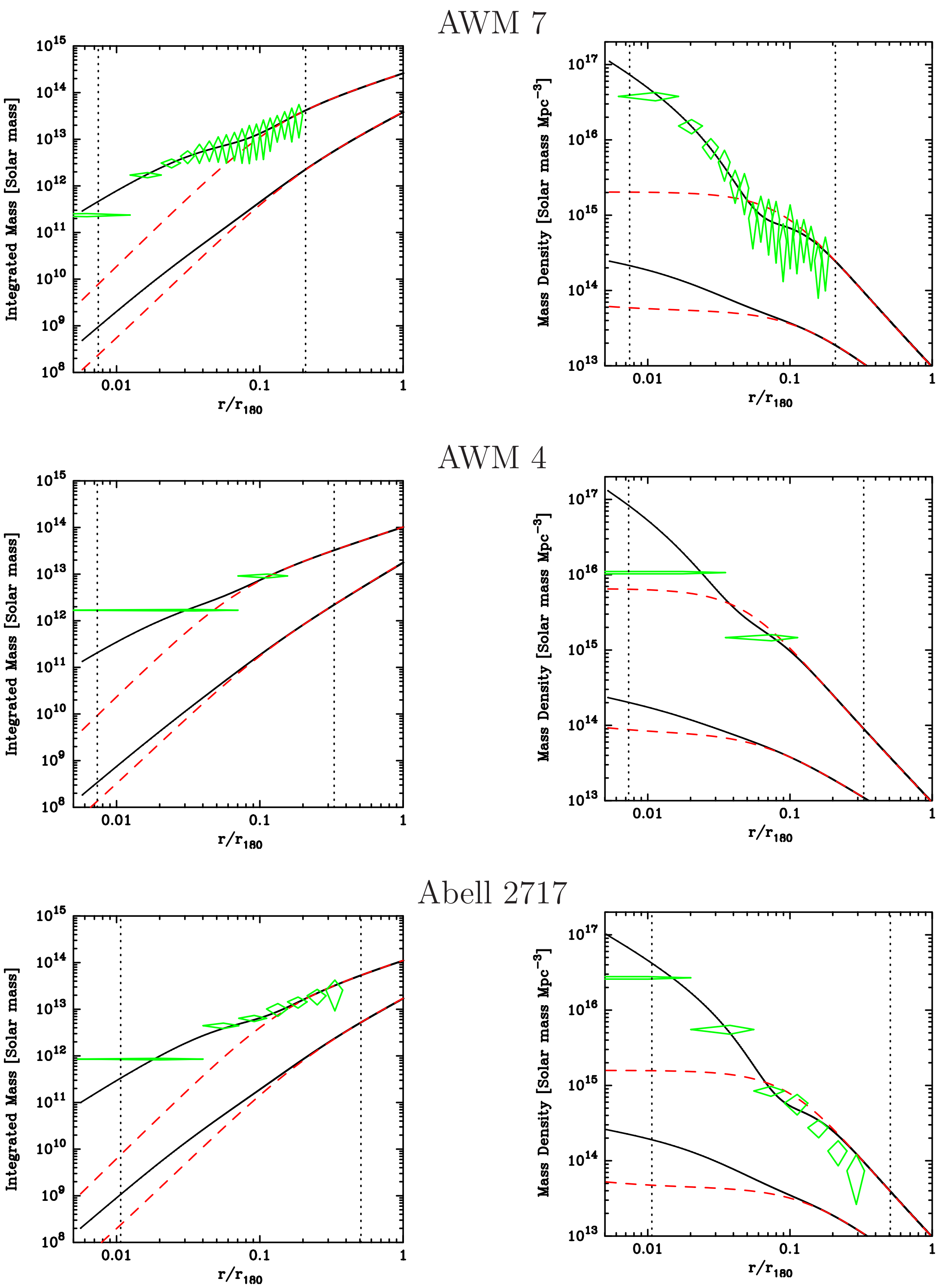

Figure 6.20: Left: Gravitational mass profile estimated from the single β-model (upper dashed line) and the density profile. The lower lines represent the ICM mass based on the β-model and the density profile, respectively. The diamonds show the results when the temperature variation is considered. The dotted regions represent the observed area. Right: Same as the left figure, but for the differential mass density profiles.

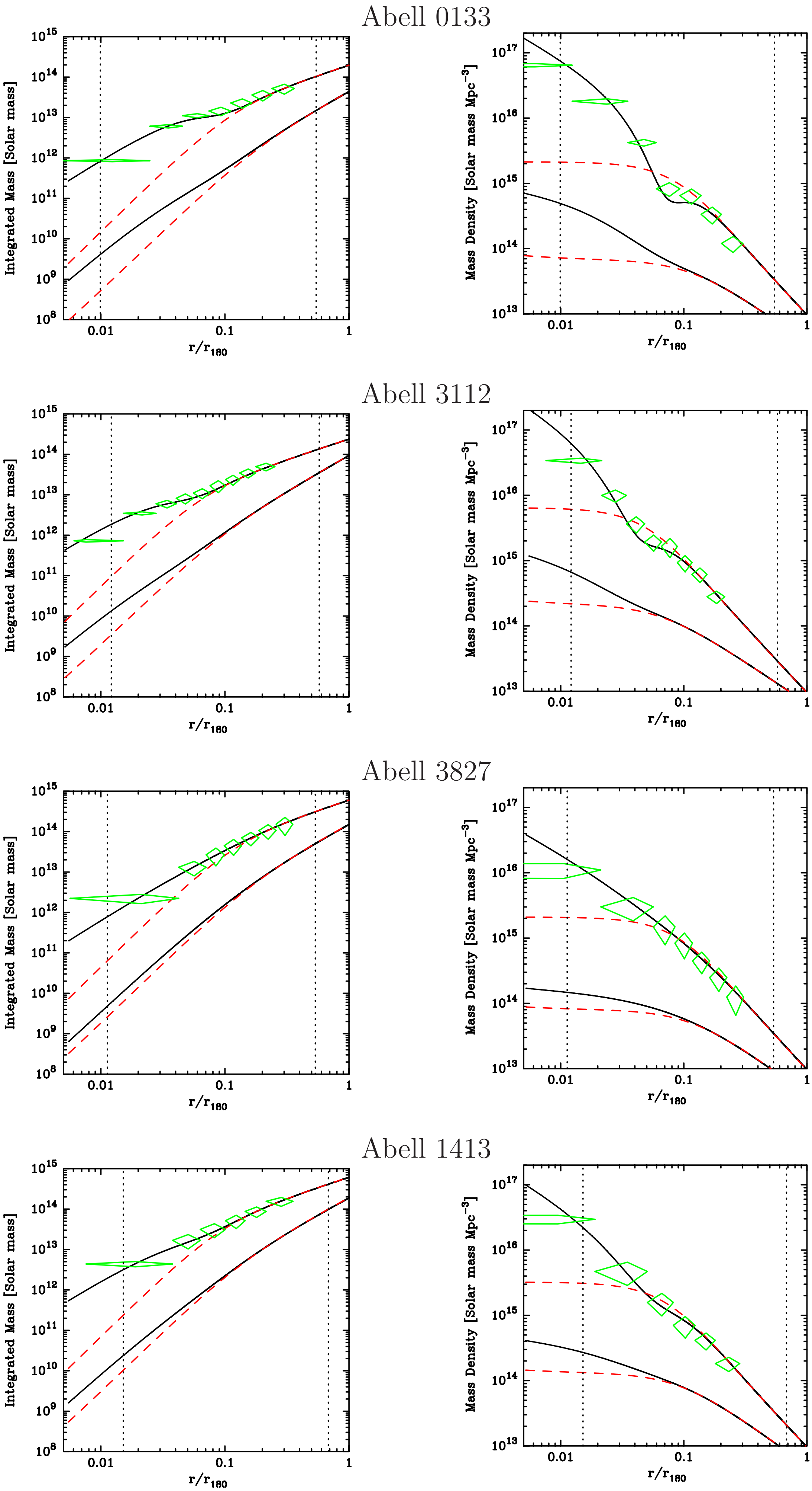

Figure 6.21: Continued.

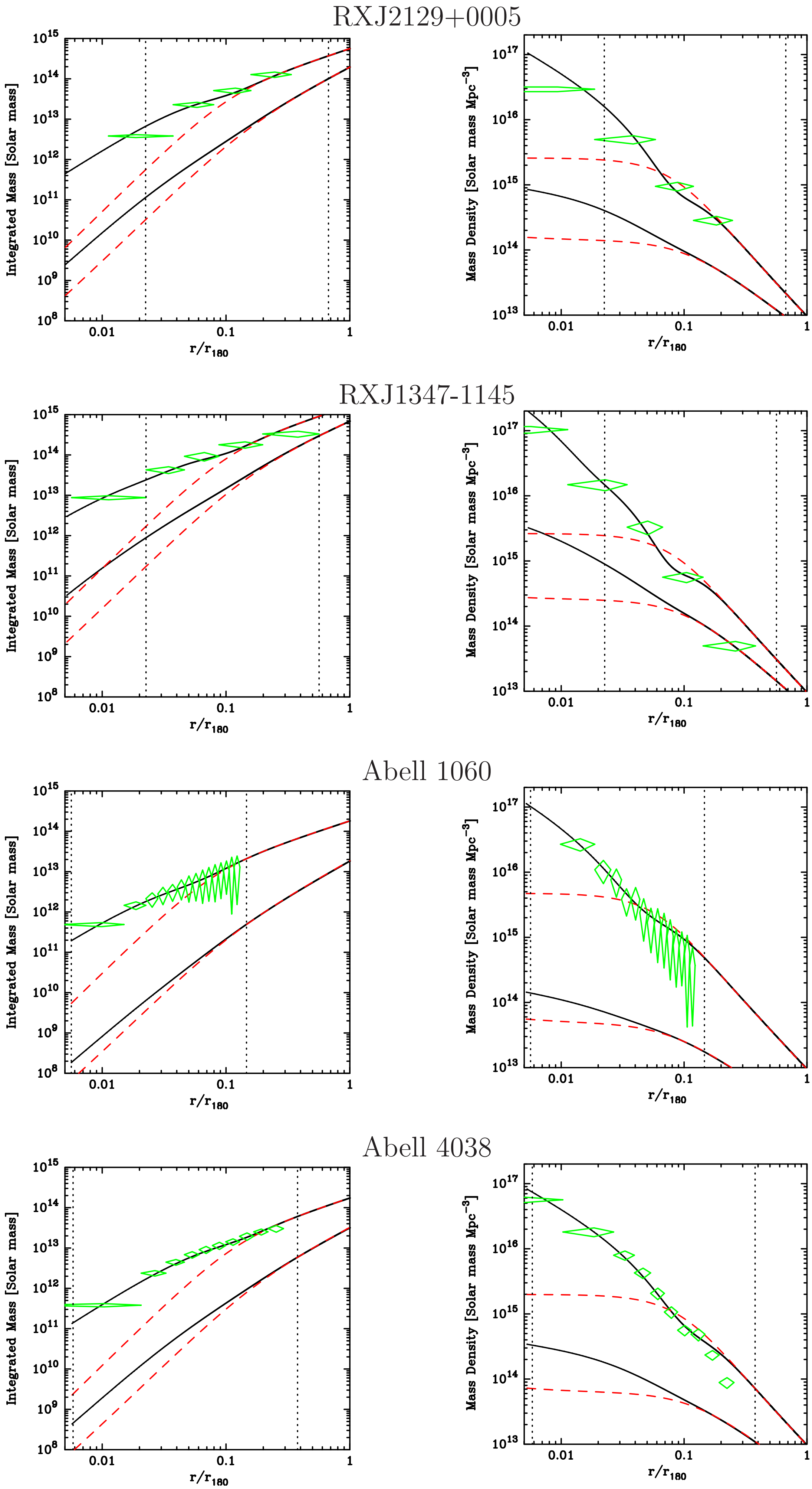

Figure 6.22: Continued.

Abell 0576

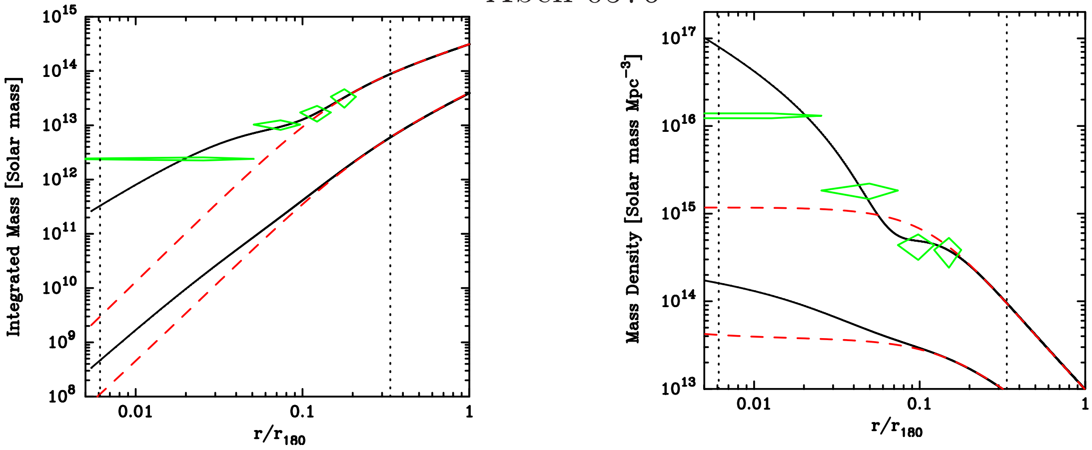

MKW 9

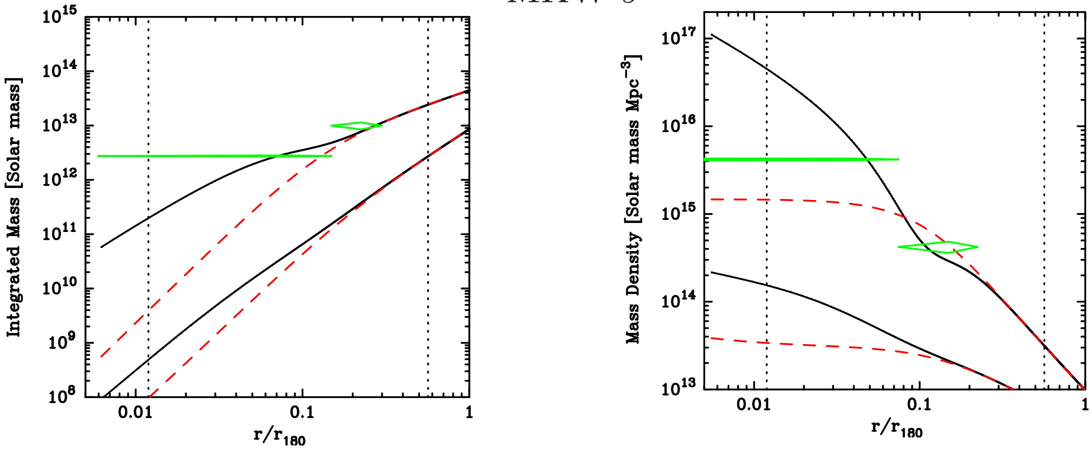

Abell 1983

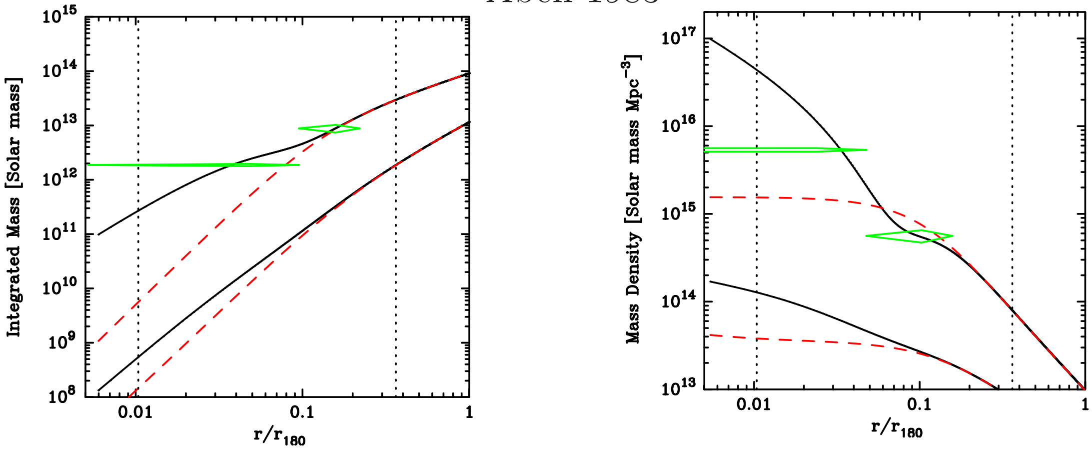

Abell 3532

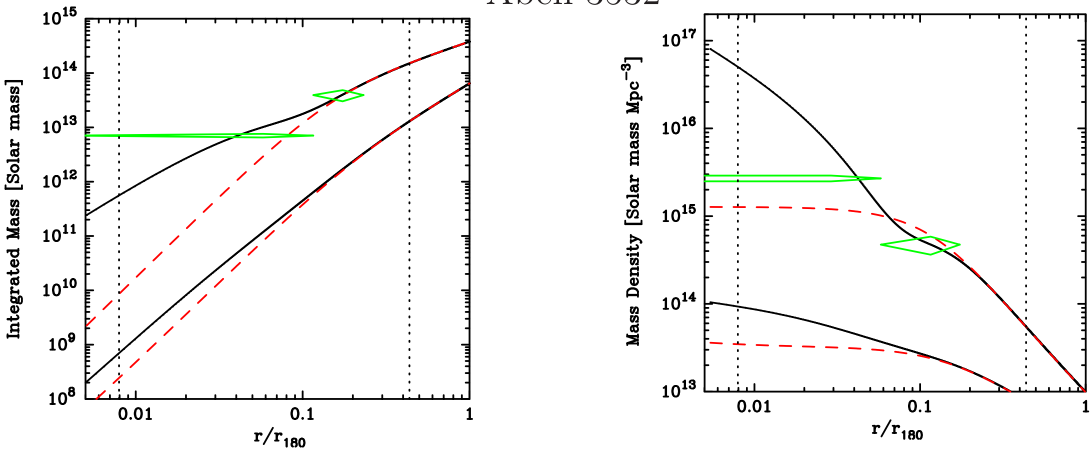

Figure 6.23: Continued.

Abell 0278

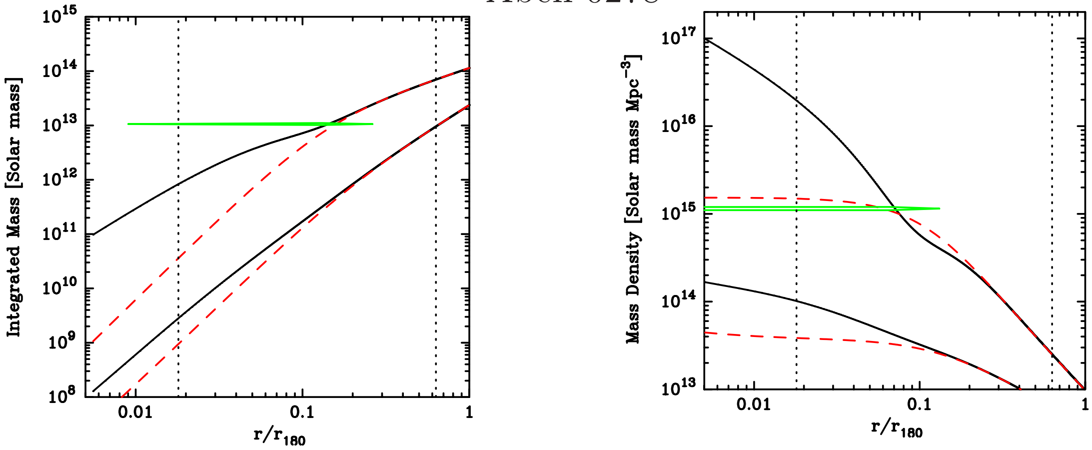

Abell 2051

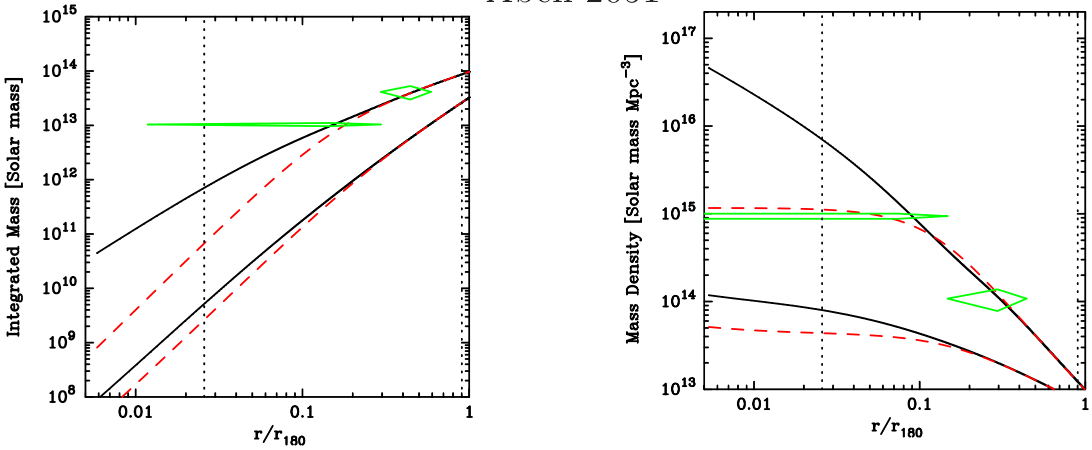

Abell 2050

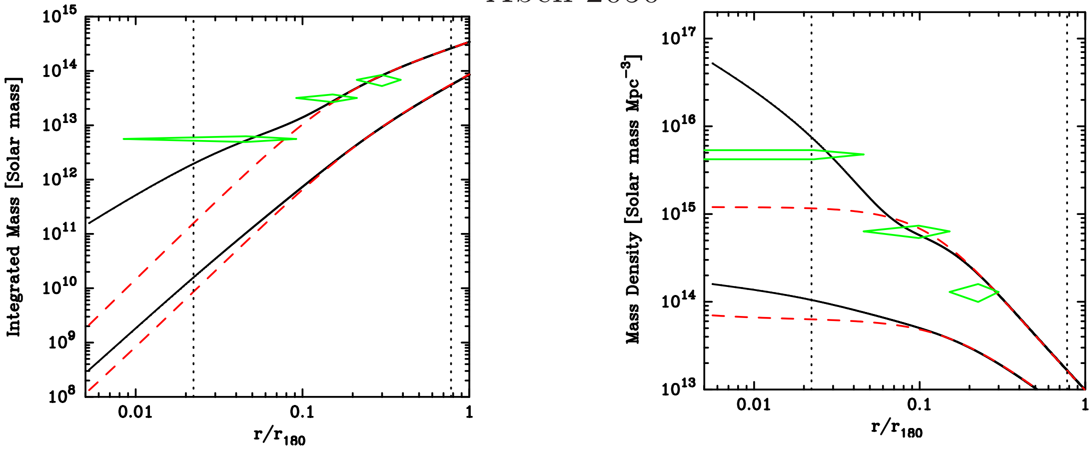

Abell 1689

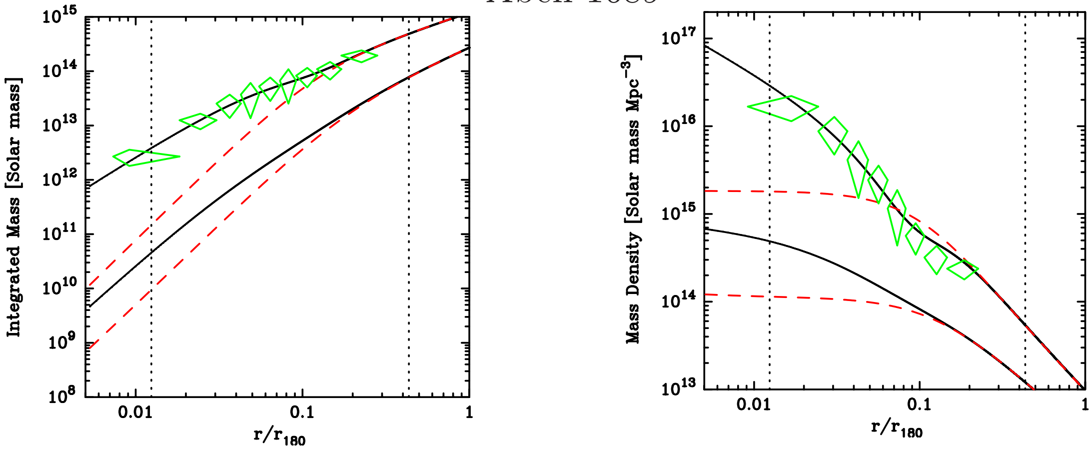

Figure 6.24: Continued.

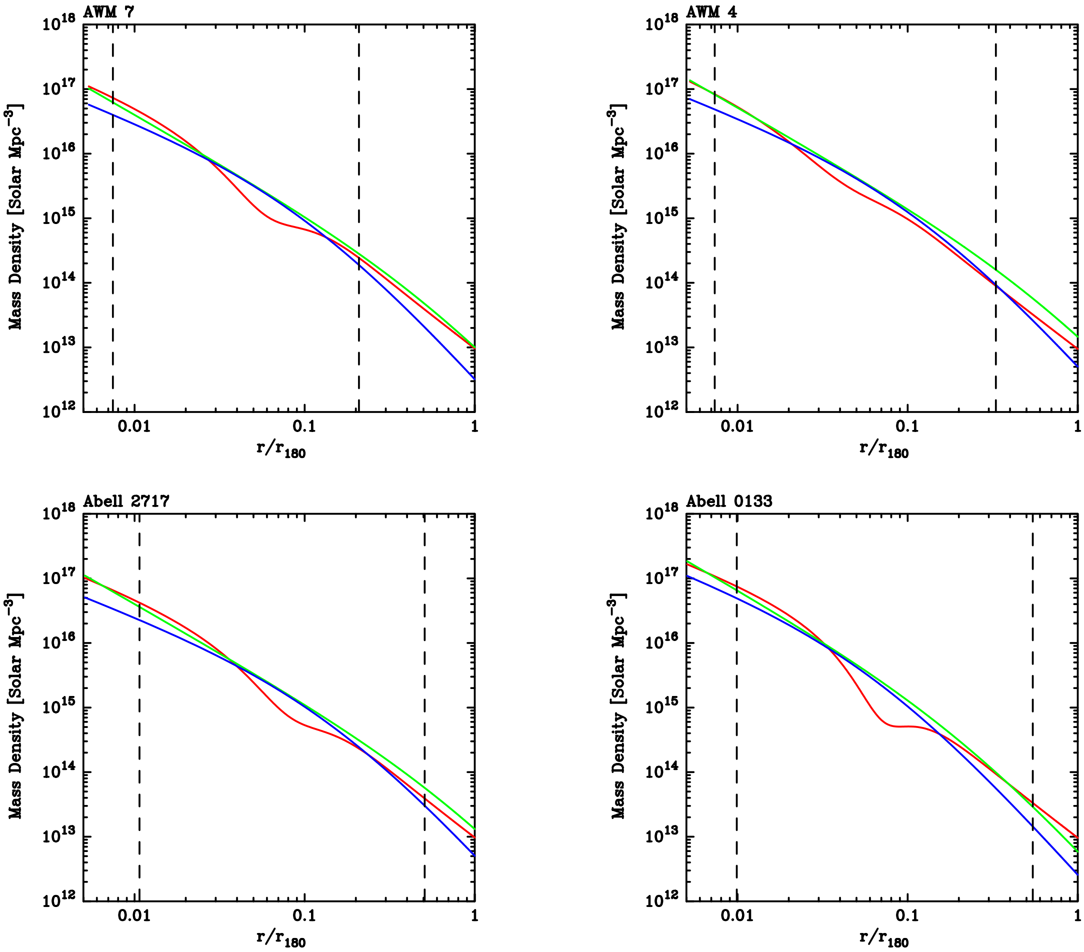

Figure 6.25: Comparison of the mass density profiles estimated from the SSM-model fit and iteration method for all our sample clusters. The red, green and blue lines represent the profiles calculated by the iteration method, the SSM-model fit with $\alpha = 1.5$ and that with $\alpha = 1$, respectively. We assumed the isothermal gas. The dashed regions represent the observed area.

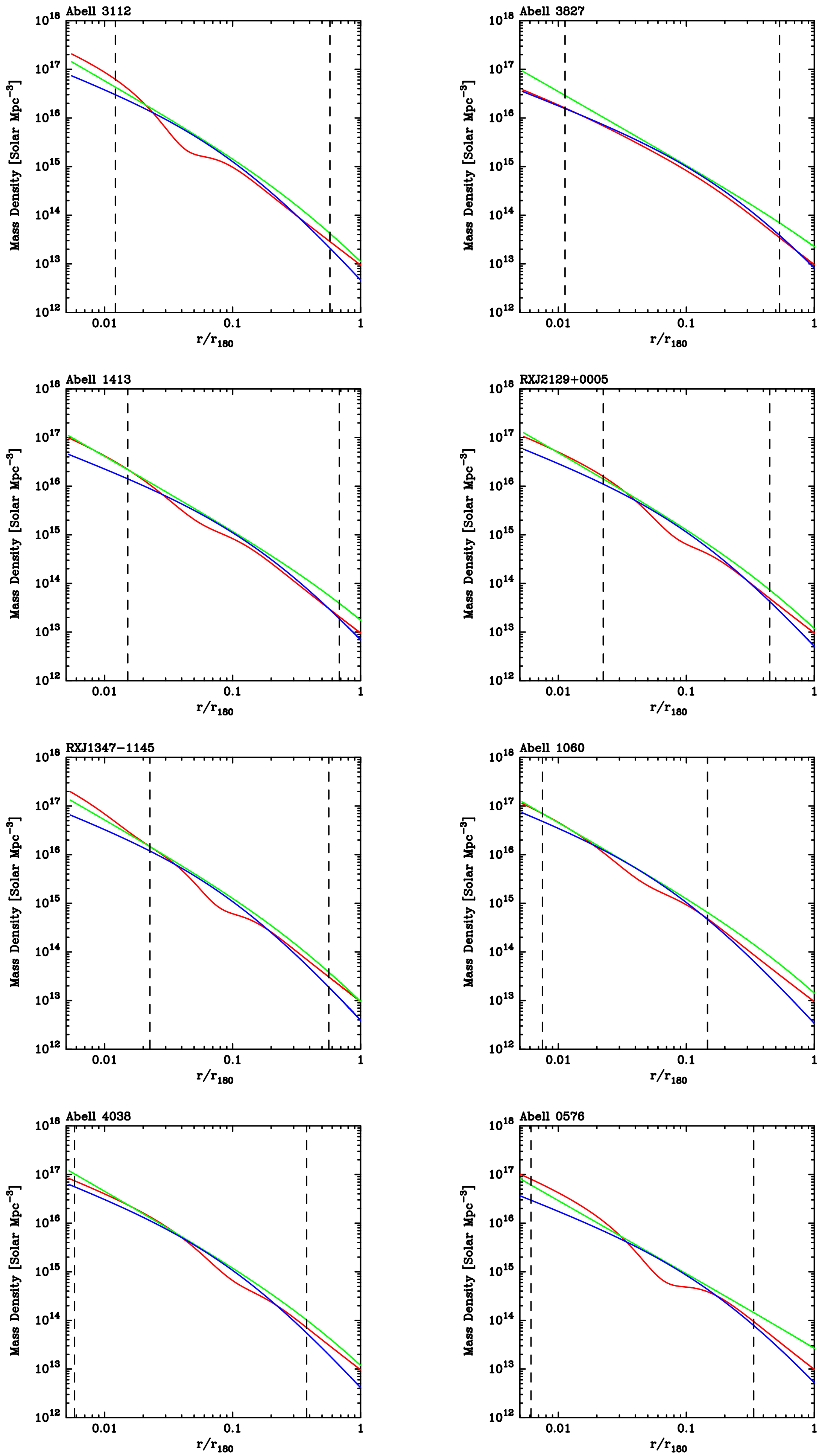

Figure 6.26: Contnued.

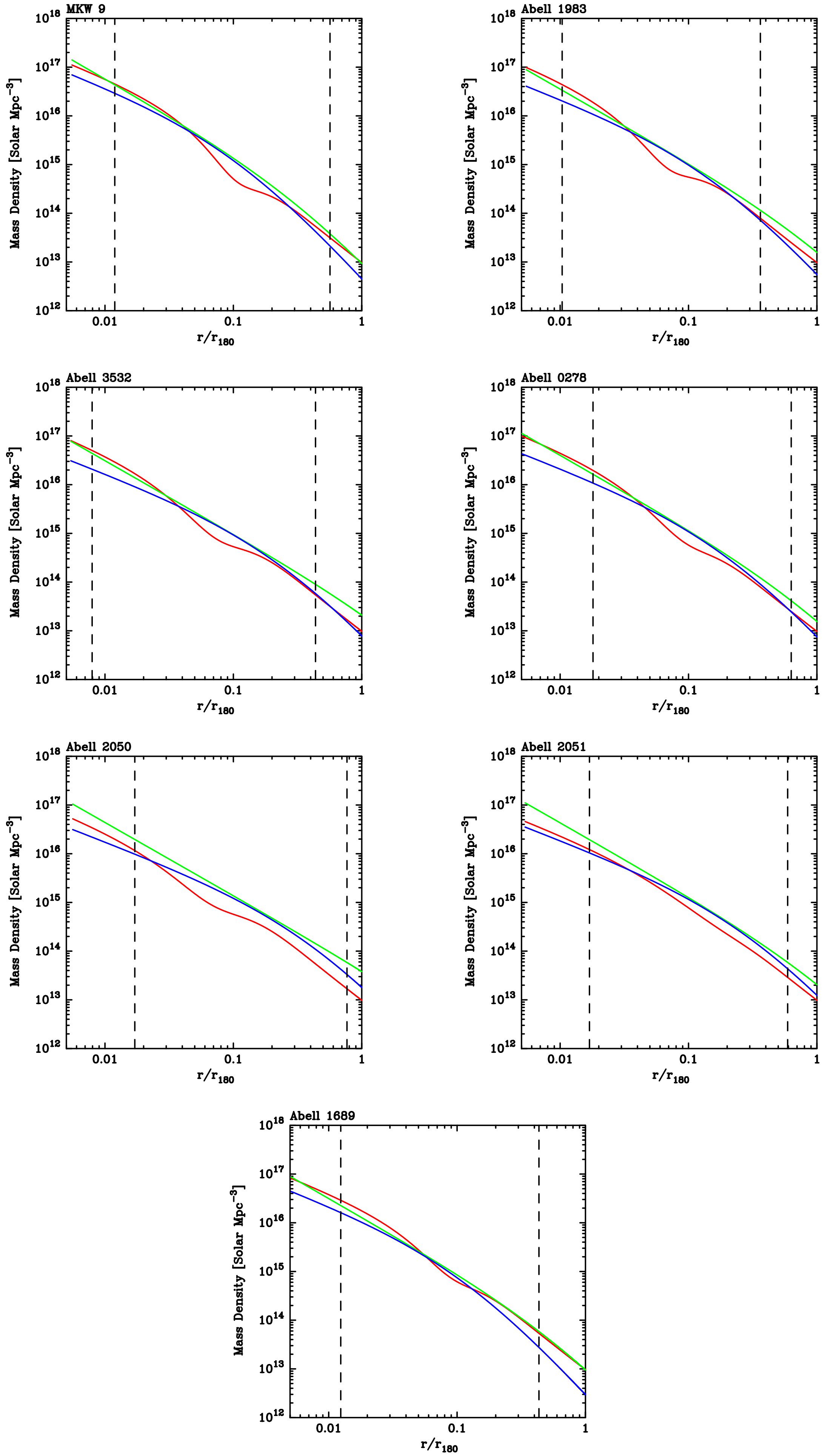

Figure 6.27: Continued.

Chapter 7

Discussion

7.1 r_{180} and total mass within $r180$

As discussed in §2.3.2, r_{180}, which is the radius where the density of matter is 180 times as large as the critical density, correspond to the virial radius. If galaxy clusters have undergone self similar evolution, we can directly compare all of our sample clusters by scaling the radius from the cluster center with r_{180}. In this section, we estimate the value of r_{180} for all our sample clusters based on the gravitational mass distribution which was esitmated by the iteration process in §6.3 together with the total gravitational mass M_{tot}, total gas mass M_{gas} and gas mass fraction f_{gas} within r_{180}. We summarize the resultant values of these parameters in table 7.1. The errors of r_{180} of each clusters are estimated considering the β-model error of the density profile, which is discussed in appendix B. The errors of M_{tot}, M_{gas} and f_{gas} are calculated based on the r_{180} error. In the following subsections, we discussed on these parameter.

7.1.1 r_{180} estimation

Evrard, Metzler, & Navarro (1996) predict that the average cluster temperature strongly correlates with the cluster mass based on their simulations. Markevitch et al. (1998) utilize this correlation to calculate r_{180} in their paper, using their weighted temperatures and the Evrard, Metzler, & Navarro (1996) fit to the simulations,

$$r_{180}\ (T) = 2.6h^{-1} \times (kT/10\ \mathrm{keV})^{0.5}\ \mathrm{Mpc}. \tag{7.1}$$

Hereafter we denote r_{180} estimated based on this relation as $r_{180}\ (T)$. This relation is widely used to calculate r_{180}. First of all, we compare $r_{180}\ (M)$, which was calculated by the density profile based on the iteration method, with $r_{180}\ (T)$. Figure 7.1 (top) shows the result of comparision. As shown in this figure, we found that $r_{180}\ (M)$ is systematically as high as $\sim$ 80 % for the $r_{180}\ (T)$. The same results has been already reported by Sanderson et al. (2003) and Piffaretti et al (2005). We note that this difference depend on the difference of the applied model in outer region. Our $r_{180}\ (M)$ is calculated on the basis of β-model in outer region while $r_{180}\ (T)$ is evaluated with the NFW profile. If we plot the r_{180} based on the NFW profile, it distributes on the dashed line, though it has large scatter. In general, it has been widely accepted that β-model is better than NFW model in the outer region. Consequently, we adopt the $r_{180}\ (M)$ hereafter.

7.1.2 Temperature dependence

Most baryons, i.e., obserbable matter, in clusters are in the form of hot, X-ray-emitting gas. Hence, most of our direct knowledge about the structure of clusters comes from

Table 7.1: central density, r_{180}, and total mass

Cluster	r_{180} [kpc]	M_{gas} [$M_\odot$]	M_{tot} [$M_\odot$]	f_{gas} [M_{gas}/M_{tot}]
AWM7	1302^{+34}_{-31}	$4.82^{+0.07}_{-0.08} \times 10^{13}$	$2.61^{+0.21}_{-0.18} \times 10^{14}$	$0.185^{+0.015}_{-0.013}$
AWM4	954^{+21}_{-19}	$2.22^{+0.08}_{-0.06} \times 10^{13}$	$1.02^{+0.08}_{-0.06} \times 10^{14}$	$0.218^{+0.019}_{-0.014}$
A2717	980^{+17}_{-16}	$2.14^{+0.01}_{-0.01} \times 10^{13}$	$1.11^{+0.06}_{-0.05} \times 10^{14}$	$0.193^{+0.010}_{-0.009}$
A0133	1188^{+19}_{-18}	$5.52^{+0.06}_{-0.04} \times 10^{13}$	$1.98^{+0.10}_{-0.09} \times 10^{14}$	$0.279^{+0.014}_{-0.013}$
A3112	1267^{+7}_{-8}	$11.77^{+0.21}_{-0.12} \times 10^{13}$	$2.39^{+0.04}_{-0.04} \times 10^{14}$	$0.492^{+0.012}_{-0.010}$
A3827	1721^{+18}_{-19}	$19.01^{+0.12}_{-0.10} \times 10^{13}$	$6.01^{+0.20}_{-0.20} \times 10^{14}$	$0.316^{+0.011}_{-0.011}$
A1413	1733^{+17}_{-16}	$23.92^{+0.29}_{-0.22} \times 10^{13}$	$6.13^{+0.18}_{-0.17} \times 10^{14}$	$0.390^{+0.012}_{-0.011}$
RXJ2129+0005	1683^{+25}_{-25}	$24.44^{+0.27}_{-0.24} \times 10^{13}$	$5.61^{+0.25}_{-0.23} \times 10^{14}$	$0.436^{+0.020}_{-0.018}$
RXJ1347-1145	2410^{+49}_{-46}	$86.42^{+1.46}_{-1.44} \times 10^{13}$	$16.49^{+1.04}_{-0.92} \times 10^{14}$	$0.524^{+0.034}_{-0.031}$
A1060	1154^{+35}_{-31}	$2.33^{+0.07}_{-0.08} \times 10^{13}$	$1.81^{+0.17}_{-0.14} \times 10^{14}$	$0.129^{+0.013}_{-0.011}$
A4038	1137^{+20}_{-19}	$4.05^{+0.03}_{-0.03} \times 10^{13}$	$1.74^{+0.09}_{-0.08} \times 10^{14}$	$0.233^{+0.012}_{-0.011}$
A0576	1384^{+50}_{-44}	$4.95^{+0.02}_{-0.04} \times 10^{13}$	$3.12^{+0.35}_{-0.29} \times 10^{14}$	$0.159^{+0.018}_{-0.015}$
MKW9	723^{+27}_{-22}	$1.08^{+0.01}_{-0.02} \times 10^{13}$	$0.45^{+0.05}_{-0.04} \times 10^{14}$	$0.240^{+0.027}_{-0.022}$
A1983	919^{+57}_{-44}	$1.45^{+0.01}_{-0.01} \times 10^{13}$	$0.93^{+0.18}_{-0.13} \times 10^{14}$	$0.156^{+0.030}_{-0.022}$
A3532	1477^{+57}_{-49}	$8.06^{+0.11}_{-0.06} \times 10^{13}$	$3.80^{+0.46}_{-0.36} \times 10^{14}$	$0.212^{+0.026}_{-0.020}$
A 0278	990^{+32}_{-27}	$2.97^{+0.04}_{-0.02} \times 10^{13}$	$1.14^{+0.11}_{-0.09} \times 10^{14}$	$0.261^{+0.021}_{-0.025}$
A 2051	937^{+2}_{-1}	$4.10^{+0.10}_{-0.08} \times 10^{13}$	$0.97^{+0.01}_{-0.01} \times 10^{14}$	$0.423^{+0.011}_{-0.009}$
A 2050	1427^{+30}_{-29}	$10.83^{+0.01}_{-0.02} \times 10^{13}$	$3.43^{+0.22}_{-0.20} \times 10^{14}$	$0.316^{+0.020}_{-0.018}$
A1689	2165^{+46}_{-41}	$34.07^{+0.35}_{-0.28} \times 10^{13}$	$11.66^{+0.77}_{-0.67} \times 10^{14}$	$0.292^{+0.020}_{-0.017}$
A0209 *	1577^{+9}_{-9}	$27.26^{+0.05}_{-0.05} \times 10^{13}$	$4.61^{+0.08}_{-0.08} \times 10^{14}$	$0.591^{+0.010}_{-0.010}$

X-ray observations. Important cosmological conclusions derived from X-ray observations of clusters usually rely on simple theoretical assumptions. For example, measurement of the cosmological parameters from the evolution of the cluster temperature function (Henry 1997) relies on the conversion of temperature to mass as $M \propto T^{3/2}$. Therefore, it is important to check this relation based on observed cluster temperature. Since mass is in proportion to cubic radius, this relation between temperature and mass can be written as $r \propto T^{1/2}$. We plot the r_{180} and the total mass within r_{180} against the cluster average temperature, which was estimated by spectral analysis, in figure 7.2. These correlation is very tight and close to the theoretically expected $r \propto T^{0.5}$ and $M \propto T^{1.5}$, respectively. We fit power law model to these temperature relations. The best-fit relations are written as

$$r_{180} = 2.15 \pm 0.03 \times (kT/10\ \mathrm{keV})^{0.56\pm0.15}\ \mathrm{Mpc} \tag{7.2}$$

and

$$M_{tot}(< r_{180}) \propto T^{1.67\pm0.05} \tag{7.3}$$

respectively, where we wrote the r_{180} relation as the same form of eq. 7.1 for easy comparison.

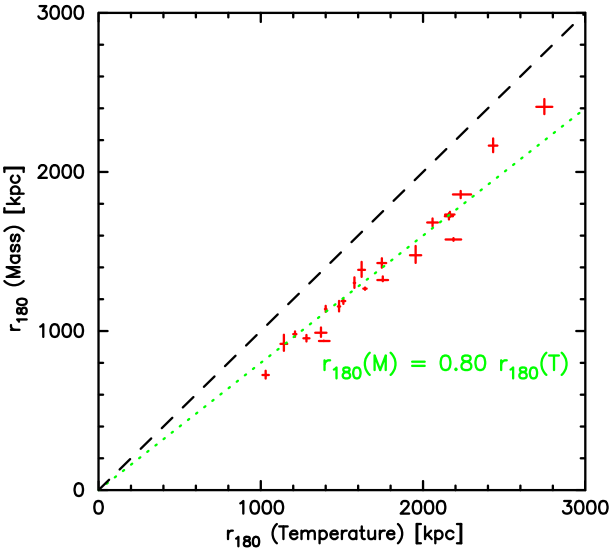

Figure 7.1: Comparision of r_{180} derived by the temperature relation eq. 7.1 with r_{180} estimated by the total mass profile based on the iteration procedure. The dashed line indicates both r_{180}'s being equal. The dotted line corresponds to the best-fit relation.

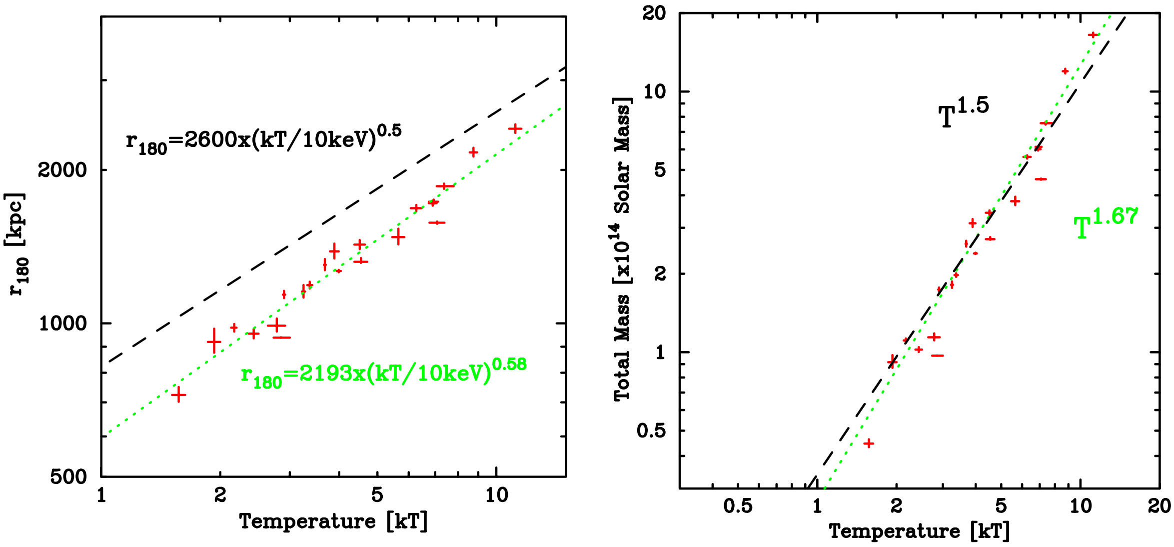

Figure 7.2: Temperature dependence of r_{180} (left) and the gravitational mass M_{tot} (right). In the left panel, the dashed line represents the relation of 7.1 and the dotted line represents the best-fit relation. In the right panel, the dashed and dotted lines represent $\propto T^{1.5}$ and best fit relation, respectively.

The best fit slope of the $M-T$ relation (1.67 ± 0.05) is formally inconsistent with the theoretical expectation ($= 1.5$) at more than 90% confidence level. However the value of this slope is decided by the two clusters with the highest temperature and one cluster with the lowest temperature. If we remove these three clusters from the fitting, the resultant slope becomes 1.56 ± 0.07 which is consistent with the theoretical prediction. The apparent discrepancy of the slope can be considered as a result of systematic error due to the small sample number.

Figure 7.3 show the temperature dependence of β, which was evaluted based on the β-model fit in the range $R_{in} - R_{out}$ (see §6.3.1). Because the radial range used for the

β-model fitting is rather limited, our resultant β values have large error. As shown in this figure, the values of β are distributed around the canonical value 2/3 (e.g. Jones & Forman 1984). According to some authors β-T relation shows week correlation (Arnaud & Evrard 1999, Helsdon & Ponman 2000, Sanderson et al 2003. and so on). There seems to be a correlation also in our β-T relation, but it is difficult to estimate the correlation large error.

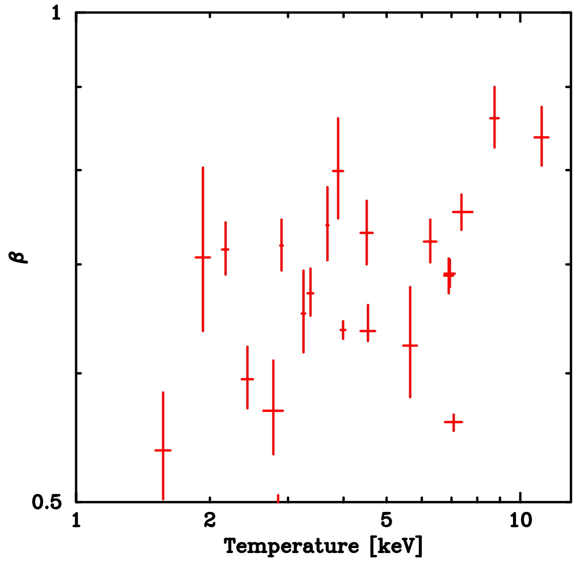

Figure 7.3: Temperature dependence of β. The values of β were estimated by the iteration method.

7.1.3 Gas fraction

In this subsection, we study redshift dependence of f_{gas}, which is the ratio gas mass to the total mass within r_{180}, which was summarized in tab. 7.1 for our sample clusters. Figure 7.4 (top) show the f_{gas} against the redshift of each clusters. As shown in this figure, the f_{gas} clearly increases with increasing cluster redshift (circled point). However we have to be careful to accept this resluts, because it is thought that f_{gas} is constant without no redshift dependence, according to the cosmology. We estimate f_{gas} as the ratio of the gas mass to the total mass within r_{180}. In this estimation, we use the critical density at $z = 0$. However, the critical density is dependent on the redshift in reality. The redshift dependence of the critical density is described as eq. 3.10 - 3.12. According to these equations, we recalculate the f_{gas}. Here, we assumed the SCDM and ΛCDM cosmology. The resultant f_{gas} value of each cosmology is overlaid in figure 7.4. The redshift dependence of the f_{gas} value show a different slop for different cosmology. With the SCDM cosmology with $z = z_{obs}$, for example, the redsift dependence of f_{gas} disappears in the range of $z > 0.1$, whereas f_{gas} still depends on the redshift with the ΛCDM.

We assumed the redshift when the cluster was collapsed is equal to $z = z_{obs}$. However we do not know the formation epoch. Since for most of our clusters, $r_{vir} \gg r_c$, the average density inside the r_{vir} is approximately $\propto kT\beta r_{vir}^{-2}$ (eq. 2.32). Since $\rho_{crit} \propto (1 + z_{col})^3$ for $\Omega_0 = 1$,

$$r_{vir} \propto (kT\beta)^{1/2}(1 + z_{col})^{-3/2}. \tag{7.4}$$

It is natural to believe that the redshift when the cluster is collapsed is older than the observed redshift, the r_{vir} should be in reality smaller than that estimated from eq. 7.4.

Generally, the radial distribution of the dark matter concentrates on the central region than the gas distribution. Accordingly the f_{gas} decreases toward the center. If the redshift when the cluster was collapsed is much earlier than $z = z_{obs}$, the redshift dependence of f_{gas} will be completely different from that shown in figure 7.4.

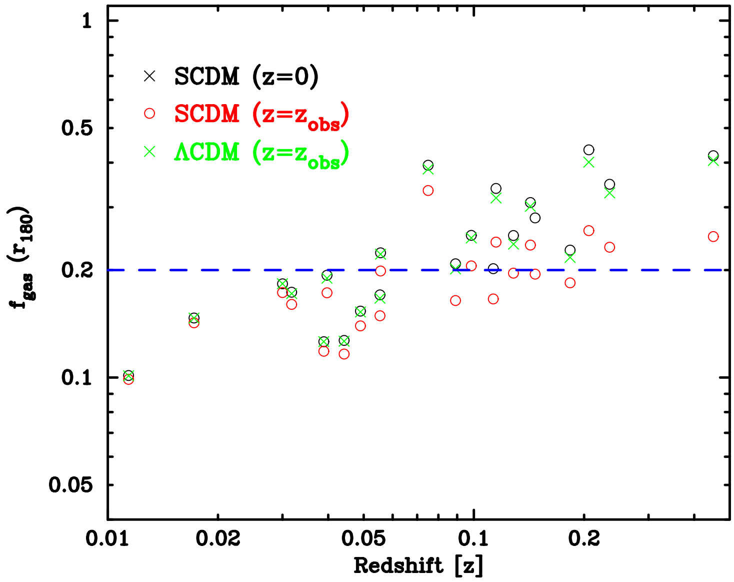

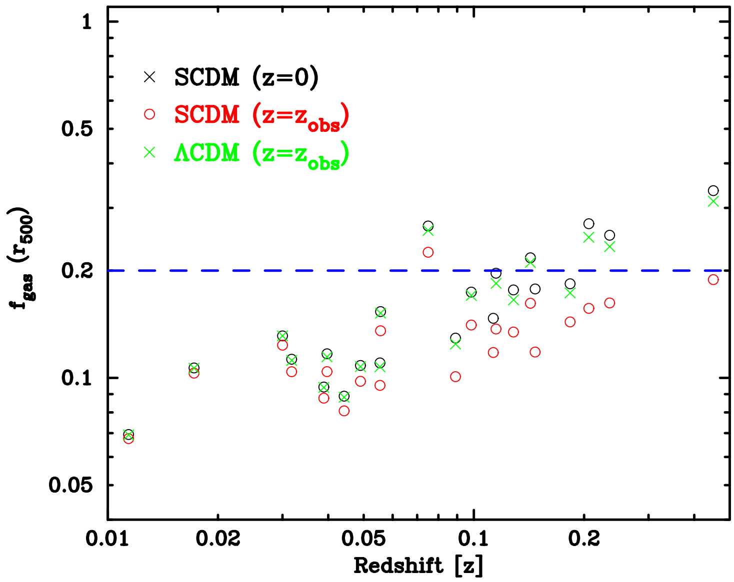

Figure 7.4: Redshift dependence of the f_{gas} within r_{180} (top) and r_{500} (bottom).

7.2 Temperature and abundance Distribution

7.2.1 Temperature Distribution

Radial temperature profiles of the ICM is one of the primary tools to study the gravitational processes responsible for large scale structure formation and nongravitational energy input into the ICM. The temperature profile is also an important consmological measurement because in dynamically relaxed systems it is the basic ingredient in estimating the total cluster mass distribution. Various observational studies have been carried out so far, which sometimes result in different conclusions regarding temperature gradients in the outer regions. Markevitch et al. (1998) analyzed projected radial temperature profiles of 30 clusters observed with *ASCA*, finding that nearly all the clusters in their sample, show a significant decline at large radii. However, White (2000) studied a sample of 106 clusters observed with *ASCA* and found that 90 percent of the clusters can be regarded as being isothermal. As the recent results, Piffaretti et al. (2005) and Vikhlinin et al (2005) study the radial temperature profiles of 13 nearby clusters with *XMM-Newton* and *Chandra*, respectively. They find the temperature drop at the outer radii which is consistent with the Markevitch's result. Such a different results are caused by difficulty of temperature measurement at cluster outer region. Cluster brightness at the virial radius is in general only 10% of the cosmic X-ray background in the soft X-ray band.

Figure 7.5 (top) shows the projected radial temperature profile of all our samples. Since deprojected temperture profile becomes statistically very poorer than projected profile, we use the projected temperature profiles. As shown in this figure, our cluster temperature profiles are equally distributed uniformly from 2 keV to 13 keV. Theory predicts that clusters should be approximately self similar because they form from scale-free density perturbations and their dynamics are governed by the scale free gravitational force. Self-similarity implies, in particlular, that cluster temperature and density profiles should be similar when radii are scaled with the cluster virial radius, for which we can adopt r_{180}. For our samples, we plot the radial temperature profile scaled by r_{180} in figure 7.5 (bottom). In this figure, the temperature is also scaled with the average temperature based on the spectral analysis in §5.1.2. The dashed line in figure 7.5 (bottom) represents the typical scatter of individual profiles Markevitch et al. (1998). Our measurements are roughly consistent with their result in the radius range of $0.05 < r/r_{180} < 0.55$ though the temperature slightly higher. In $0.05 > r/r_{180}$, the cD clusters show the temperature drop. This feature is not clear in the non-cD clusters.

7.2.2 Abundance Distribution

We also deal with the radial abandance profiles. As discussed above, we scaled the cluster radius using the r_{180}. Figure 7.6 shows the resultant scaled abundance profile of all our samples. De Grandi & Molendi (2004) analyzed the temperature and abundance profiles for 12 cooling flow and 10 non-cooling flow clusters observed with *BeppoSAX*. They found that the deprojected abundance profiles are strongly peaked at the center for the cooling flow clusters while they remain constant for non-cooling flow clusters. Furthermore, they found that the iron mass associated with abundance excess in the cooling flow clusters correlates with the optical magnitudes of the central bright galaxies. For these reasons, they thought that the abundance concentration of the cooling flow clusters is produced by the central bright galaxies. In our sample clusters, the cD clusters which has the central cool component shows the abundance concentration while the non-cD clusters show flat profile. This feature is consistent with that derived by De Grandi & Molendi (2004). Thus, we would conclude that the central abundance excess is produced by the central galaxy, especially by the cD galaxy.

According to De Grandi & Molendi (2004), the mean abundance at $r > 0.2r_{180}$ is different between cooling core and non-cool core clusters. They suggest that this could indicate that cooling core clusters are older systems than the non-cooling flow clusters. In this case the early-type galaxy population of cooling core clusters had more time to produce metals and eject them into the ICM than the non-cooling flow clusters. The average value of cooling core and non-cooling core clusters are ~ 0.4 and ~ 0.3 solar,

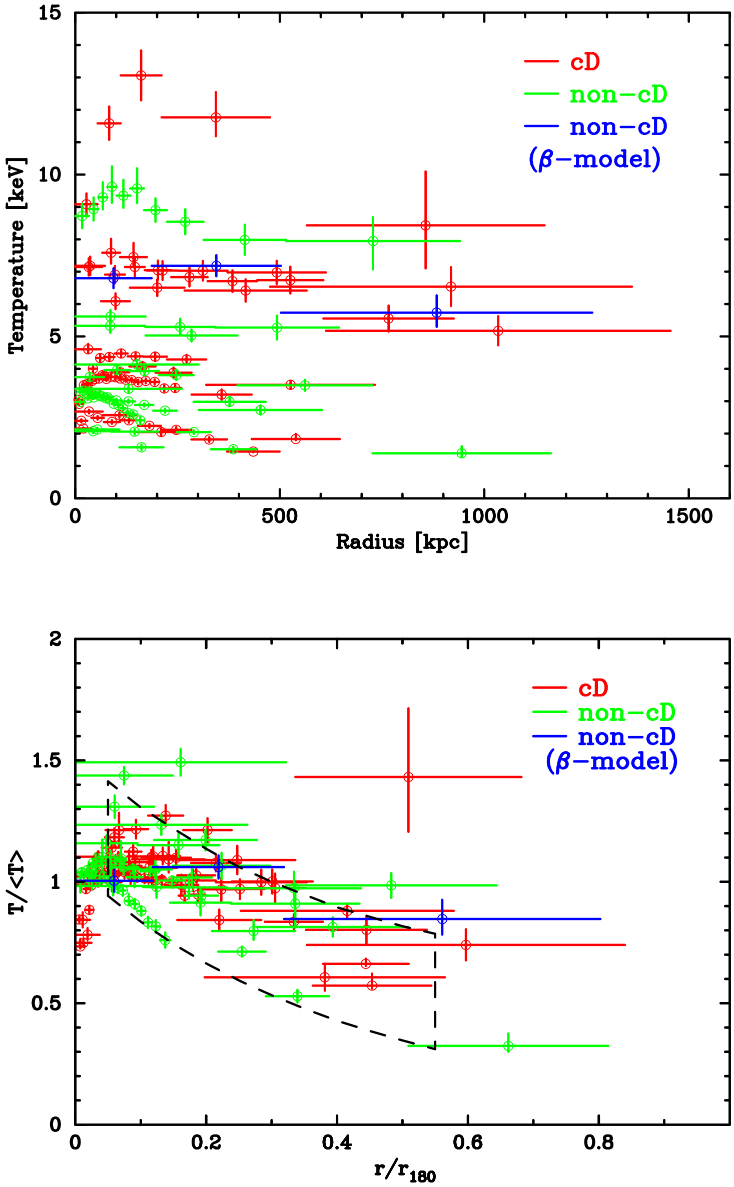

Figure 7.5: The top panel shows the radial temperature profiles of all our samples. We scaled the temperature and radius using the average temperature and r_{180} for each clusters. The red, green and blue lines represent the cD, non-cD and non-cD clusters whose entire profile can be fitted by a single β-model. The dashed line represents the typical scatter of individual profiles Markevitch et al. (1998).

respectively. In our resultant abundance profile, this feature is not clear, because the statistical error become large at large radii.

In some of our sample clusters, temperature couple with abundance and take a small values in particular in outer radii, and the abundance becomes close to 0 in such a case. This result is caused by the background uncertainty. We remove these regions.

7.3 Property of the cluster outer region

In this section, we discuss the property of the cluster brightness profile in outer region based on the β-model parameters, β and r_c. Figure 7.7 shows the β and r_c distributions

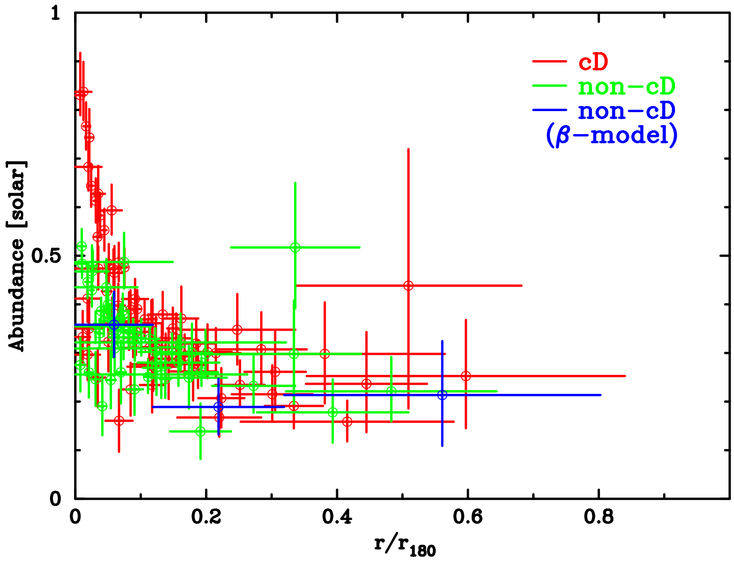

Figure 7.6: The radial abundance profile of all our samples. The radius which centerd on the cluster center are scaled using r_{180}. The red, green and blue lines represent the cD, non-cD and non-cD clusters whose entire profile can be fitted by a single β-model.

of the our cluster samples. As shown in these figures, β and r_c distribute evenly in $0.5 \leq \beta \leq 1$ and 50 kpc $\leq r_c \leq$ 300 kpc, respectively. We can not find any clear difference between the cD and non-cD cluster distributions.

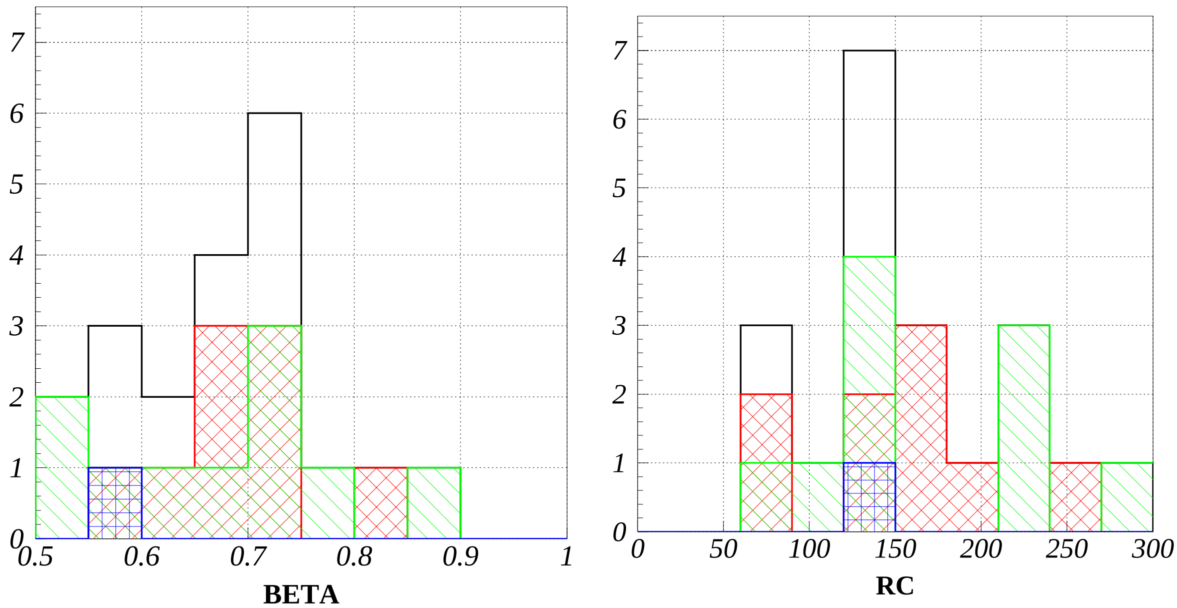

Figure 7.7: β (left) and r_c (right) distribution of the our cluster samples determined from outer regions. The red, green and blue boxes represent the cD, non-cD and non-cD clusters whose entire profile could be fitted by a single β-model. The sum of all the clusters are shown as brack line.

Next, we show the β and r_c relation in figure 7.8. The elongated circles represent the 90 % confidence range. We scale the r_c values in the left panel r_{180}. The resultant β-r_c/r_{180} relation is shown in the right panel. We can clearly see that the cD and non-cD clusters show different distributions.

The β and r_c values of the cD clusters show compact distribution at around $\beta \sim 0.7$ and $r_c/r_{180} \sim 0.11$, while the non-cD clusters show large scatter with β being in the range 0.5–0.9 and r_c/r_{180} centered at $\sim$0.14 being extended to larger value. Figure 7.9 show the distribution of r_c/r_{180}. As shown in this figure, the r_c/r_{180} values distributions of cD and non-cD clusters are clearly segregated, and cD clusters have a centrally-condensed mass distribution. The compact β distribution of the cD clusters also suggest that the cD clusters reach the stage of higher degree of evolution than the non-cD cluster.

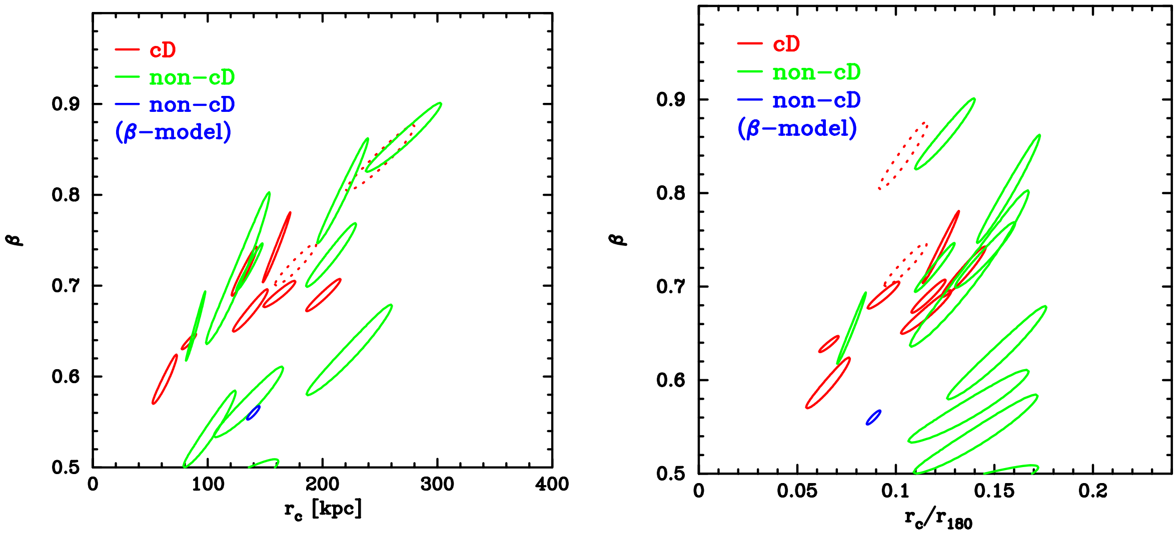

Figure 7.8: Comparision of the β and r_c values based on the β-model fitting. For r_c we adopt a unit of kpc in the left panel, whereas it is scaled r_c with r_{180} in the right panel. The red, green and blue ellipses represent the cD, non-cD and non-cD clusters whose entire surface brightness profile can be fitted with a single β-model.

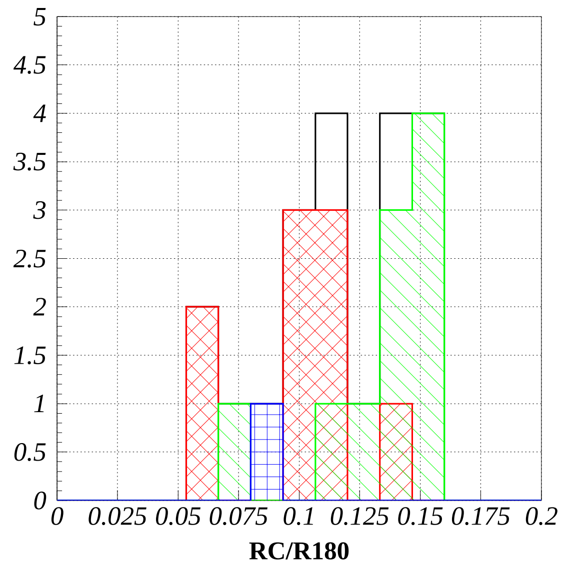

Figure 7.9: r_c/r_{180} distribution of our cluster samples. The red, green and blue boxes represent the cD, non-cD and non-cD clusters whose entire surface brightness profile can be fitted with a single β-model. The sum of all clusters are shown as black line.

7.4 Mass distribution

7.4.1 SSM-model fitting

In this subsection, we evaluate the observed surface brightness profile with the following three models.

- isothermal β-model
- SSM-model with $\alpha = 1.0$ (standard NFW model)
- SSM-model with $\alpha = 1.5$

where the SSM-model was described in eq. 6.4.1. Initially, α is fixed because there are a lot of parameters in the model. Figure 7.10 compares the results of the fit to the data with these three models. The left (right) panel show the comparison between β-model (SSM-model with $\alpha = 1.0$) and SSM-model with $\alpha = 1.5$. The SSM-model with $\alpha = 1.0$ correspond to standard NFW-model (Navarro, Frenk & White 1996). As shown in this figure, the SSM-model with $\alpha = 1.5$ provides the best fit. This is the first result that indicates the gas distribution systematically shows the profile represented by the SSM-model with $\alpha = 1.5$ rather than the NFW-like $\alpha = 1.0$. This result is suggested by the resent numerical simurations (Fukushige, Kawai & Makino 2004, Moore et al. 1999).

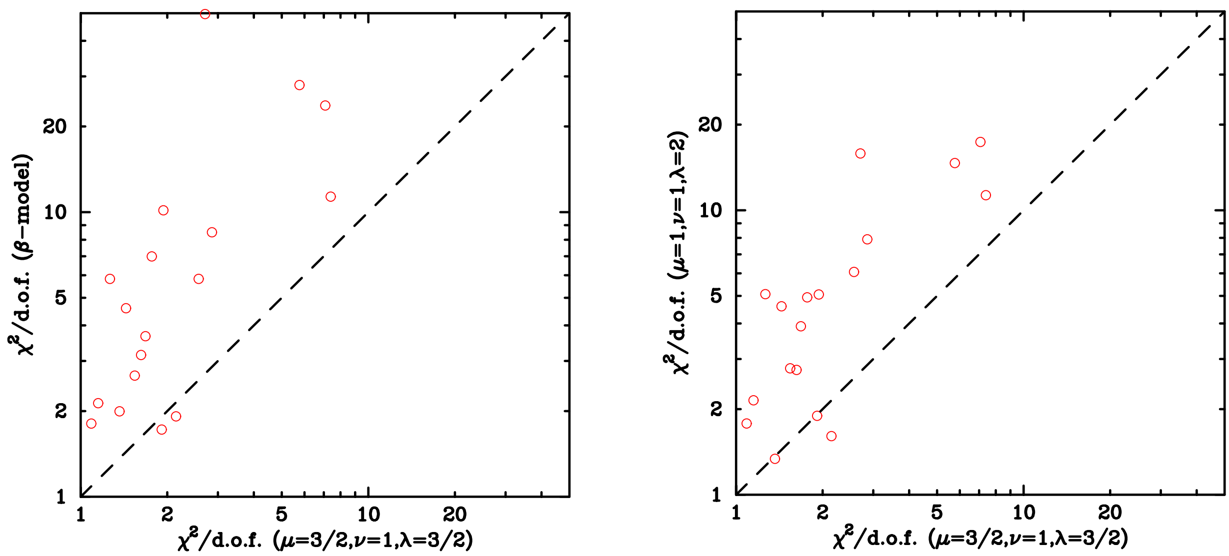

Figure 7.10: Comparision of the resultant $\chi^2/d.o.f.$ values based on the surface brightness model fits. The left (right) panel show the comparison between β-model (SSM-model with $\alpha = 1.0$) and SSM-model with $\alpha = 1.5$ fit. The SSM-model with $\alpha = 1.0$ correspond to the standard NFW-model (Navarro, Frenk & White 1996).

Next we carried out the SSM-model fit with α being set free to vary, in order to examine whether $\alpha = 1.5$ is the best fit and whether there is any difference between the cD and non-cD clusters. We plot the resultant α values in figure 7.11. The top figure show the resultant values of the α parameters of our sample clusters obtained from the SSM-model fit. The upper and lower arrows show the α values whose allowed upper and lower range can not be constrained. The lower left panel show the distribution of the α parameter, where we only utilize circle point in the top panel. As shown in fig. 7.11

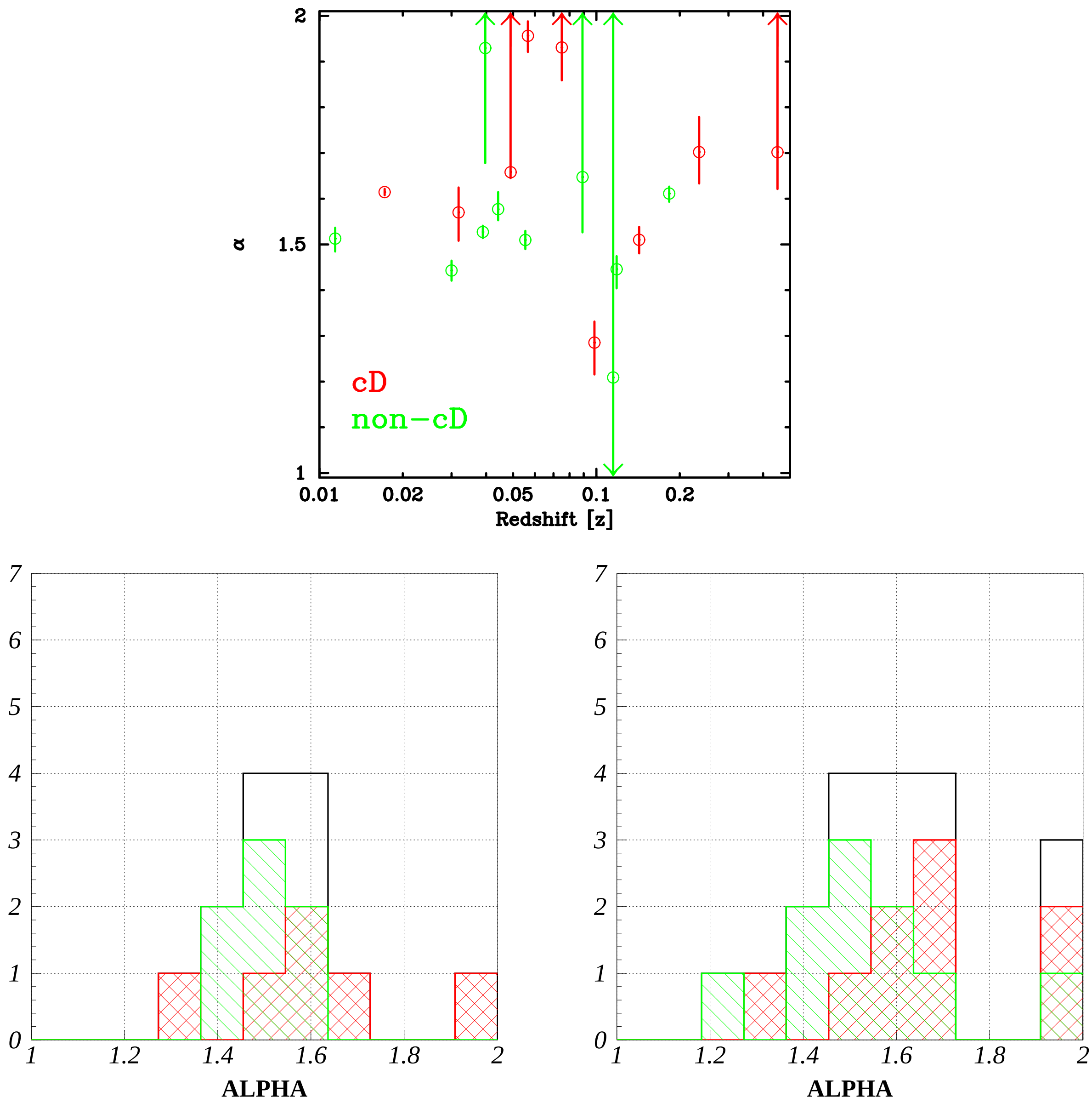

Figure 7.11: The top panel shows the α parameters of our sample clusters obtained from SSM-model fit with the α parameter being set free to vary in the range of $1 \leq \alpha \leq 2$. The upper and lower arrows show the α values whose allowed upper and lower range can not be constrained. The lower left panel show the distribution of the α parameter, where we only utilize circle point in the top panel. If we utilize all points in the top panel, the resultant α distribution become lower right panel.

(lower left), we can not confirm the difference in the distributions between cD and non-cD clusters, and the α value is centered at ~ 1.5 for both groups. The slope of the cluster total mass profile is $r^{-1.5}$, irrespective of cD or non-cD clusters. If we utilize all points in the top panel, however, the resultant α distribution(lower right) shows split between cD and non-cD clusters distrbutions. We discuss in detail about this difference based on the total gravitational mass profiles.

7.4.2 Iteration method

In this subsection, we discuss the difference between the cD and non-cD clusters based on the total gravitational mass profiles which was calculated by the iteration method in §6.3. The gravitational force contributes to the cluster evolution, and hence, we can expect to see the difference between the cD and non-cD cluster in the gravitational mass profile. Figure 7.12 shows the summary of the total gravitational mass and the mass density profiles of all our samples as a function of the radius in a unit of kpc. The total mass

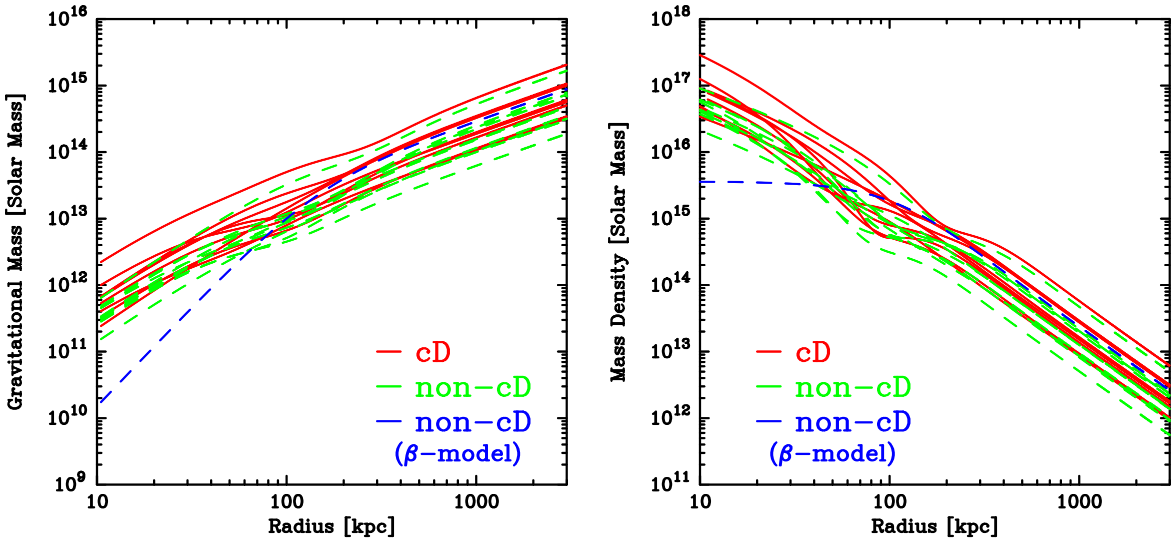

Figure 7.12: Summary of the integrated (left) and differentiated (right) gravitational mass profiles. These profiles are estimated by the iteration method in §6.3. The red, green and blue lines represent the cD, non-cD and non-cD clusters whose entire profile can be fitted by a single β-model.

of our samples distributes within the range of about an order of magnitude. Figure 7.13 shows the integrated (left) and differentiated (right) gravitational mass profiles against the scaled radius r/r_{180}. For integrated mass profiles, we also normalize the total mass within r_{180} $(M(r)/M(< r_{180}))$. We can obviously see following two characteristics. In the outer region, $r/r_{180} \geq 0.1 - 0.2$, the scaled mass profiles shows good agreement with all sample clusters. In contrast, for the inner region ($r/r_{180} \leq 0.1 - 0.2$), the scaled mass profiles shows large scatter, which seems to be related with the cD and non-cD clusters. The central mass of the cD clusters is relatively higher than the non-cD clusters. To demonstrate this split quantitatively, we draw the distribution of the total mass within the radius $r/r_{180} = 0.01$ and in figure 7.14. The total mass within 0.01 r_{180} of the cD clusters are systematically larger than that of the non-cD clusters. However, this feature disappears at the radius 0.1 r_{180}(fig. 7.14 right). It is difficult to explain this feature based on cD galaxy stellar mass distribution (see blue dash dot line in fig. 7.13).

In general, $r/r_{180} \sim 0.1 - 0.2$ correspond to the cooling radius within which the mean cooling time of the gas is equal to the Hubble time (1.3×10^{10} yr). The cooling time is calculated by $\propto n^{-1}T^{1/2}$. Figure 7.15 shows the cooling time of all our sample clusters. As shown in this figure, the inner region which has the large scatter is consistent with the cooling region. Since the cooling is important inside this raidus the gravitational energy is dissipated by means of the gas cooling, and consequently a cD galaxy is formed, due to the mass concentration. Note that the difference of the total mass within 0.01 r_{180} between cD and non-cD clustars are probably larger in reality than that shown in figure

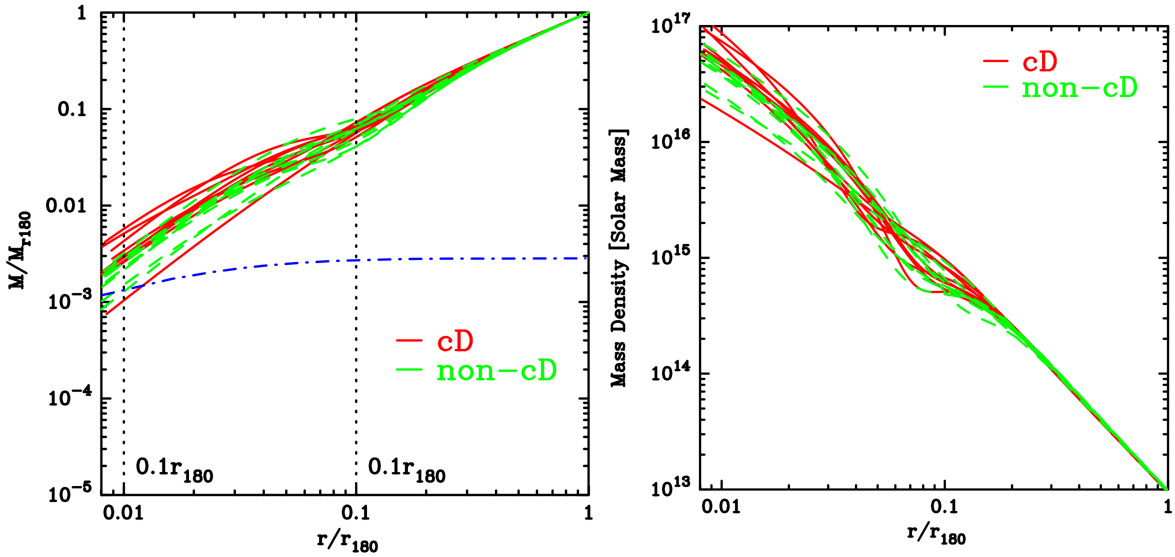

Figure 7.13: Summary of the scaled integrated (left) and differentiated (right) gravitational mass profiles. We scaled the radius using r_{180}, and then, for integrated mass profiles, we also scaled the normarization using the total mass within r_{180}. The red, green lines represent the cD, non-cD clusters. non-cD fitted by single β-model was removed. The blue dash dot line show the typical cD galaxy stellar mass distribution.

7.14, because we do not include irregular and gas poor clusters in our sample. These irregular and poor clusters are flatter in the radial mass distribution than the regular clusters. As a result, if we would include these them, their mass profile in the central region would distributed lower than lines in fig. 7.14.

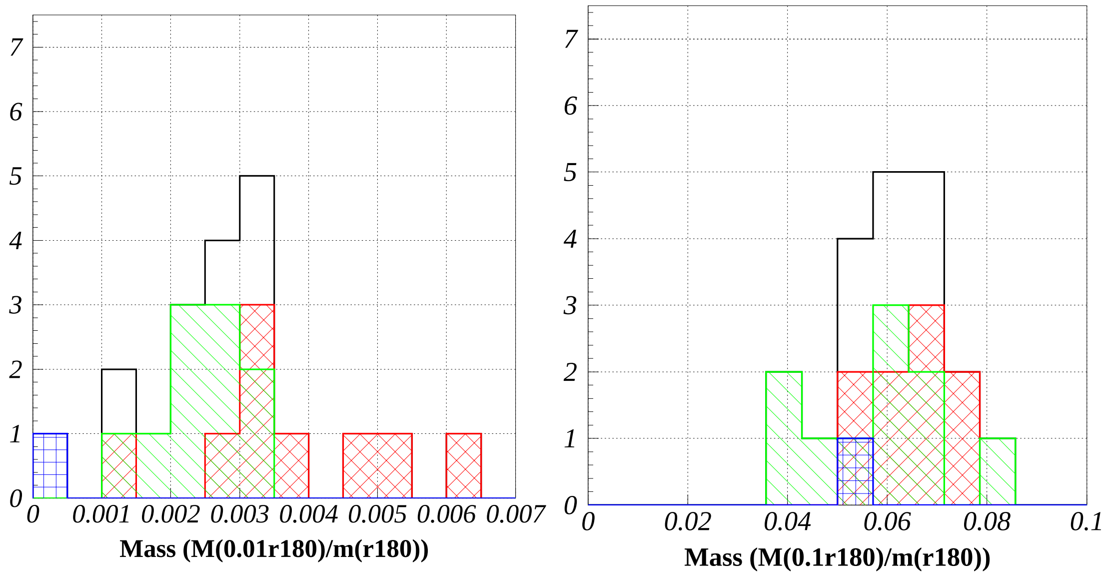

Figure 7.14: Distribution of total mass within $r < 0.01\ r_{180}$ (left), $0.1\ r_{180}$ (right). The red, green and blue boxes represent the cD, non-cD and non-cD clusters whose entire surface brightness profile can be fitted by a single β-model. The sum of all the clusters are shown as black line.

Finally, we would like to add the following two results based on the gravitational mass study, although these do not show difference between the cD and non-cD clusters.

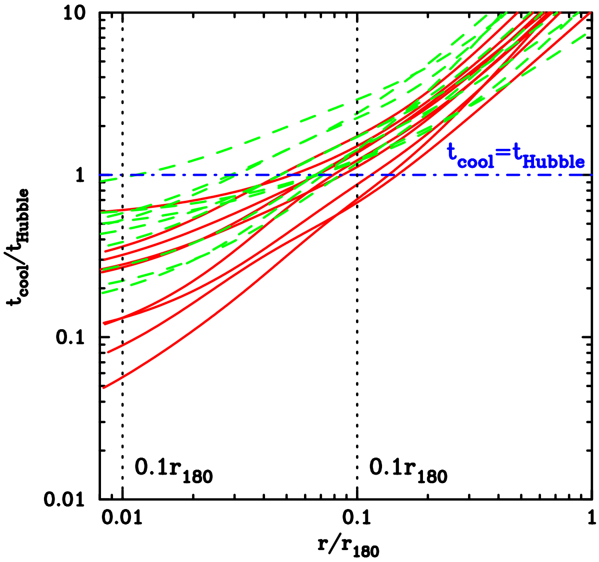

Figure 7.15: Cooling time of the ISM for each radius. We scaled the radius using r_{180}. The red lines and the green dashed lines represent the cD, non-cD clusters. The blue dash dot line represents the cooling time of the gas which is equal to the Hubble time.

- **f_{gas} distribution against r/r_{180}**

  Figure 7.16 shows the radial distribution of f_{gas} which was calculated as M_{gas}/M_{tot}. It seems that the gas is more concentrate dominant around the cD galaxy, although it may not be significant.

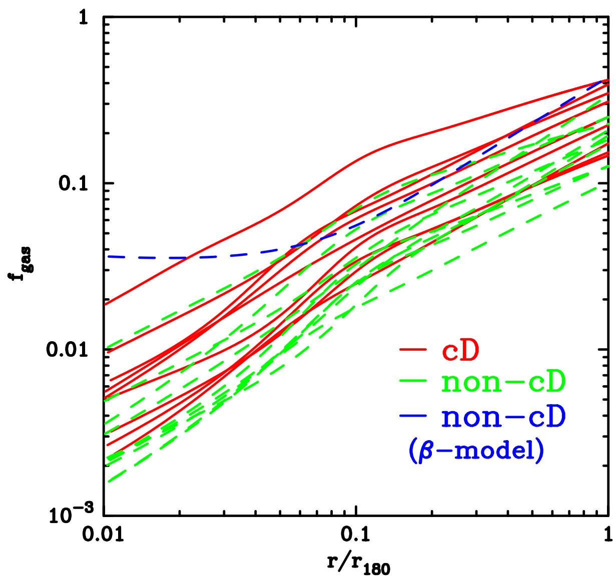

Figure 7.16: Radial f_{gas} distribution. We scaled the radius using r_{180}. The red, green and blue lines represent the cD, non-cD and non-cD clusters whose entire profile can be fitted by a single β-model.

- **Mass ratio Between before and after total mass distribution**

  Figure 7.17 show the mass ratio of the total gravitational mass profiles after and before the iteration method is applied. The mass profile before the iteration is the mass profile calculated from the isothermal β-model fitted to the data in the range of $R_{in} - R_{out}$ (see §6.3.1). There is no systematic difference of the iteration method on the central density enhancement between the cD and non-cD clusters, and hence, any difference between the cD and non-cD clusters derived from the iteration method is hardly a fake due to this method.

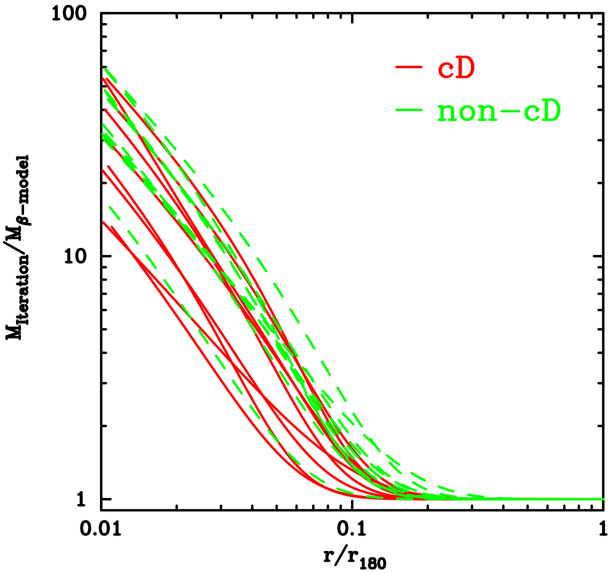

Figure 7.17: Mass ratio between before and after the iteration process. The cluster radius was scaled using r_{180}. The red, green and blue lines represent the cD, non-cD and non-cD clusters whose entire profile can be fitted by a single β-model.

Chapter 8

Summary and Conclusion

In order to study the difference between the cD and non-cD clusters, we analyzed the archival *XMM-Newton* data of 20 clusters. Among them, 18 clusters are nearby clusters in the redshift range of $z \leq 0.2$, where 7 of 18 clusters are cD type clusters, and the other 11 are non-cD type clusters. The remaining 2 are $z \geq 0.2$ clusters which were included to study the brightness profile of outer radius. Since the galaxy clusters have been considerd as being formed by the gravitational contraction, the presence or absence of the cD galaxy, which locates at the cluster center, is probably related with the stage of dynamical evolution of each cluster. Accordingly, we have attempted to obtain the gravitational mass profile of each cluster, in order to investigate the difference between cD and non-cD type clusters. In order to do this, we adopted the following two methods. One is the iterative method in which the radial gas density profile is iteratively adjusted so that it can finally reproduce the observed X-ray surface brightness distribution (see § 6.3). This method is developed by ourselves and is applied to the data for the first time in this thesis. We adopted this method to study the local mass density profile in detail (for exmaple only central and outer region). The other method is to utilize the semi-analytic model that was numerically computed by Suto, Sasaki, & Makino (1998) assuming the NFW mass profile. We hereafter refer to this as SSM-model. We used this later method to compare the overall profile.

In order to compare the profile of many clusters with different spatial extent, we scaled the radius of the cluster by the virial radius We then have obtained the following major results.

Universal gravitational mass profile

We found that the radial profile of the total gravitational mass can be fit well with the SSM model with the central slope of $\propto r^{-1.5}$. Note that this feature is independent of whether the cluster is cD type or not.

Difference mass between the cD and non-cD clusters

Within the radius of $r < 0.01\ r_{180}$, the total mass of the cD clsuters are found to be larger systematically than that of the non-cD clusters. Since the radius $0.1-0.2\ r_{180}$ is of similar size to the cooling radius, it is possible to regard the central mass concentration of the cD clsters as being caused by the gas cooling, which leads to the formation of the cD galaxy.

At $r \sim 0.1\ r_{180}$, the mass profile almost became uniform without the any difference. From β-model fitting of much outer region, we have found that the resultant parameters (r_c & β) show the different distoribution between the cD and non-cD clusters. For r_c, the value of cD clusters is less than that of the non-cD clusters, For

β, the value of non-cD cluster shows large scatter while the cD cluster converge at the ~ 0.7. These facts suggest that the cD clusters are more evolved dynamically than the non-cD clusters.

Virial radius

Based on the iterative method, we evaluated the radial density profile, and then obtained a relation between the virial radius r_{180} and the emission-weighted average temperature. The values of r_{180}, expected from $\langle T \rangle$ is found only to be 80% of the widely used prediction given by the simulation of Evrard et al. (1996). Similar results have been reported by Vikhlinin, Forman & Jones (1999) and Piffaretti et al. (2005).

Temperature & abundance distribution

We have performed spatially resolved temperature and abundance measurement for the 20 clusters. Normalizing the temperature by $\langle T \rangle$ and plotting it against the radius in a unit of r_{180}, we found that the resultant temperature profiles for $0.05 < r/r_{180} < 0.55$ of all our samples show the similar profiles, which is consistent with the encircled temperature range of Markevitch et al. (1998). We have found that the central cool compornent of cD clusters is stronger than the non-cD clusters.

The radial abundance profile strongly peaked for cD clusters while they remain almost constant for non-cD clusters in agreement with the result of De Grandi et al. (2002).

f_{gas}

We have found that the ICM gas to total mass ratio f_{gas} at the virialized radius r_{180} are consistent with the constant value of $\sim$0.2.

Appendix A

n_0 Estimation From Cluster Surface Brightness Profile

A.1 Assumption

In the cluster observation, we can only obtain two-dimensional surface brightness distribution projected on the sky. In order to reproduce three-dimensional density distribution from the two-dimensional surface brightness distribution, we make the following two assumptions.

(1) Isothermal and spherical symmetry.

(2) Density profile is represented with the following β-model equation.

$$n(\boldsymbol{r}) \;=\; n_0 \left[1 + \left(\frac{r}{r_c}\right)^2\right]^{-3\beta/2}, \tag{A.1}$$

where r_c is the core radius of the cluster.

A.2 Calculation

We use the cylindrical coordinate with z as the direction of line of sight. We can represent the r in eq. A.1 as,

$$r^2 \;=\; \rho^2 + z^2. \tag{A.2}$$

If we define the Cooling Function as $\Lambda(T)$, plasma luminosity within integrated radius R on the celestial sphere is expressed as follows.

$$\begin{aligned} L_{\mathrm{X}}(R) \;&=\; \Lambda(T) \int n^2(\boldsymbol{r})\, dV \;=\; n_0^2\, \Lambda(T) \int_{-\infty}^{\infty} dz \int_0^R d\rho\, \rho \int_0^{2\pi} d\theta \left(1 + \frac{\rho^2 + z^2}{r_c^2}\right)^{-3\beta} \\ &=\; 2\pi n_0^2 \Lambda(T) \int_{-\infty}^{\infty} dz \int_0^R d\rho\, \rho \left(1 + \frac{\rho^2 + z^2}{r_c^2}\right)^{-3\beta} \end{aligned} \tag{A.3}$$

where we use $dV = \rho\, d\rho\, dz\, d\theta$. Here, we transform the variable as

$$\zeta \equiv \frac{z}{r_c}, \quad \xi \equiv \frac{\rho}{r_c}. \tag{A.4}$$

Defining $\xi_R = R/r_c$, eq. A.3 is expressed as

$$L_{\rm X}(R) = 2\pi n_0^2 r_c^3 \Lambda(T) \int_{-\infty}^{\infty} d\zeta \int_0^{\xi_R} \frac{\xi\, d\xi}{(1+\zeta^2+\xi^2)^{3\beta}}. \tag{A.5}$$

And furthermore, transforming variable again as

$$x \equiv \frac{\xi^2}{1+\zeta^2}, \qquad \xi\, d\xi = \frac{1}{2}(1+\zeta^2)\, dx, \qquad \left(x_R \equiv \frac{\xi_R^2}{1+\zeta^2}\right), \tag{A.6}$$

we can expand eq. A.5 as follows,

$$\begin{aligned} L_{\rm X}(R) &= \pi n_0^2 r_c^3 \Lambda(T) \int_{-\infty}^{\infty} \frac{d\zeta}{(1+\zeta^2)^{3\beta-1}} \int_0^{x_R} \frac{dx}{(1+x)^{3\beta}} \\ &= \pi n_0^2 r_c^3 \Lambda(T) \int_{-\infty}^{\infty} \frac{d\zeta}{(1+\zeta^2)^{3\beta-1}} \cdot \frac{1}{3\beta-1} \left[1 - \frac{1}{(1+x_R)^{3\beta-1}}\right] \\ &= \frac{\pi n_0^2 r_c^3 \Lambda(T)}{3\beta-1} \int_{-\infty}^{\infty} \frac{d\zeta}{(1+\zeta^2)^{3\beta-1}} \left[1 - \frac{(1+\zeta^2)^{3\beta-1}}{(1+\xi_R^2+\zeta^2)^{3\beta-1}}\right] \\ &= \frac{\pi n_0^2 r_c^3 \Lambda(T)}{3\beta-1} \left[\int_{-\infty}^{\infty} \frac{d\zeta}{(1+\zeta^2)^{3\beta-1}} - \int_{-\infty}^{\infty} \frac{d\zeta}{(1+\xi_R^2+\zeta^2)^{3\beta-1}}\right]. \end{aligned} \tag{A.7}$$

Moreover, we carry out variable transformation in second and third terms as

$$\zeta \equiv \tan\theta, \qquad \zeta \equiv \sqrt{1+\xi_R^2}\, \tan\varphi \tag{A.8}$$

and

$$d\zeta = \frac{d\theta}{\cos^2\theta}, \qquad d\zeta = \frac{\sqrt{1+\xi_R^2}\, d\varphi}{\cos^2\varphi} \tag{A.9}$$

respectively, and then we can represent eq. A.7 as

$$\begin{aligned} L_{\rm X}(R) &= \frac{\pi n_0^2 r_c^3 \Lambda(T)}{3\beta-1} \left[\int_{-\pi/2}^{\pi/2} \cos^{6\beta-4}\theta\, d\theta - \frac{1}{(1+\xi_R^2)^{3\beta-3/2}} \int_{-\pi/2}^{\pi/2} \cos^{6\beta-4}\varphi\, d\varphi\right] \\ &= \frac{2\pi n_0^2 r_c^3 \Lambda(T)}{3\beta-1} \left(1 - \frac{1}{(1+\xi_R^2)^{3(\beta-1/2)}}\right) \int_0^{\pi/2} \cos^{6\beta-4}\theta\, d\theta \end{aligned} \tag{A.10}$$

When we use the following integration

$$\int_0^{\pi/2} \cos^{\alpha}\theta\, d\theta = \frac{\sqrt{\pi}}{2} \frac{\Gamma\left(\dfrac{\alpha+1}{2}\right)}{\Gamma\left(\dfrac{\alpha+2}{2}\right)} \qquad (\alpha > -1), \tag{A.11}$$

eq. A.10 can be written as follows,

$$\begin{aligned} L_{\rm X}(R) &= \frac{\pi^{3/2} n_0^2 r_c^3 \Lambda(T)}{3\beta-1} \left(1 - \frac{1}{(1+\xi_R^2)^{3(\beta-1/2)}}\right) \frac{\Gamma(3(\beta-1/2))}{\Gamma(3\beta-1)} && \text{(A.12)} \\ &= \frac{\pi^{3/2} n_0^2 r_c^3 \Lambda(T)}{3\beta-1} \left[1 - \left(\frac{r_c^2}{r_c^2+R^2}\right)^{3(\beta-1/2)}\right] \frac{\Gamma(3(\beta-1/2))}{\Gamma(3\beta-1)}, && \text{(A.13)} \end{aligned}$$

where we use $\alpha = 6\beta - 4$. The central density n_0 can be estimated when we solved eq. A.13.

Appendix B

Error estimation of the density profile

In this appendix, we estimate an error range of the radial density profile evaluated by means of the iteration method in §6.3. We decides the error which encloses the 90% confidence level. The error is divided into 2 components: inner and outer region, which are associated with the iteration process and the β-model, respectively. We estimate the radial density profile for each components separately.

At the outer region, the density profile is only decided by the β-model, which was fitted at the outer region (R_{in}–R_{out}). In figure B.1, we show a χ^2 contour at the 90% confidence level on the β–r_c plane of A 1060 as an example. The two parameters are strongly coupled and the allowed parameter range exists in an elongated region. Hence, we adopt a set of r_c and β values at both ends of the elongated contour as the upper and lower boundaries of these parameters. Figure B.2 shows the resultant profile of the β-model with the error ranges thus evaluated with the blue dashed line. Since this model was fitted using only outer region, the error become large at the both sides across the fitted region.

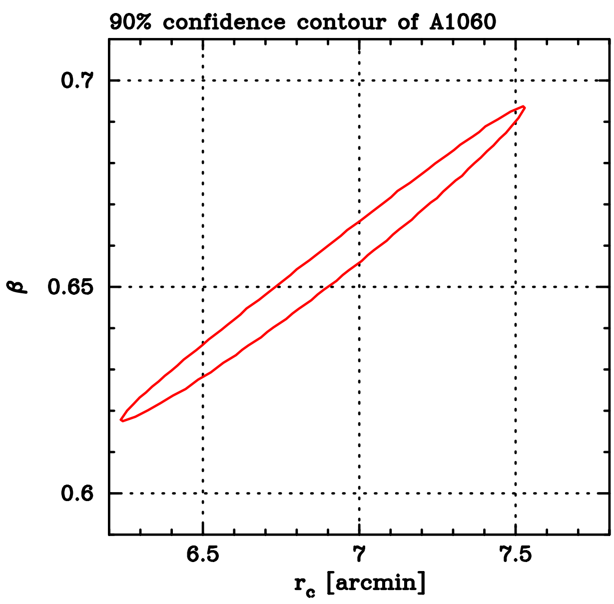

Figure B.1: χ^2 contour map of the single β model in the case of A 1060. The curve corresponds to the single-parameter error domain at the 90 % confidence level.

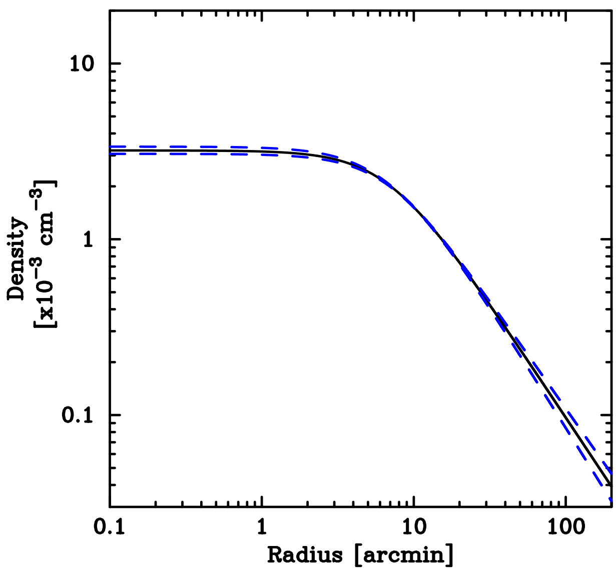

Figure B.2: The resultant profile based on the β-model with the 90% confidence error region. The error region was defined as the blue dashed line. The solid line describe the best fit β-model profile.

In the inner region, the excess component of the density profile was determined by the iteration process using the exponential function as a density ratio. In this process, the radial density profile was obtained so that it can successfully reproduce the observed surface brightness profile We estimate 90% confidence range of the density profile as follows.

After the radial density profile is estimated from the iteration process, we only change the normalization value of the final exponential function. We create the surface brightness profile from the modified density profile by changing the normalization of the exponential, and calculate the χ^2 using the obseved and model surface brightness profiles. The allowed range of the normalization, which directly results in the error of the radial density profile, is obtained by the χ^2 fit of the model surface brightness to the data. Figure B.3 shows the resultant density profile with the 90% confidence error range and the corresponding surface brightness profile as an example of A 1060. The resultant error value of all our samples is taken into account the error of n_0(after), while the n_0(before) error was estimated by β-model. Figure B.4-B.6 shos the superposed density profile with these two different error component. From these two error components, we define the error range of density profile.

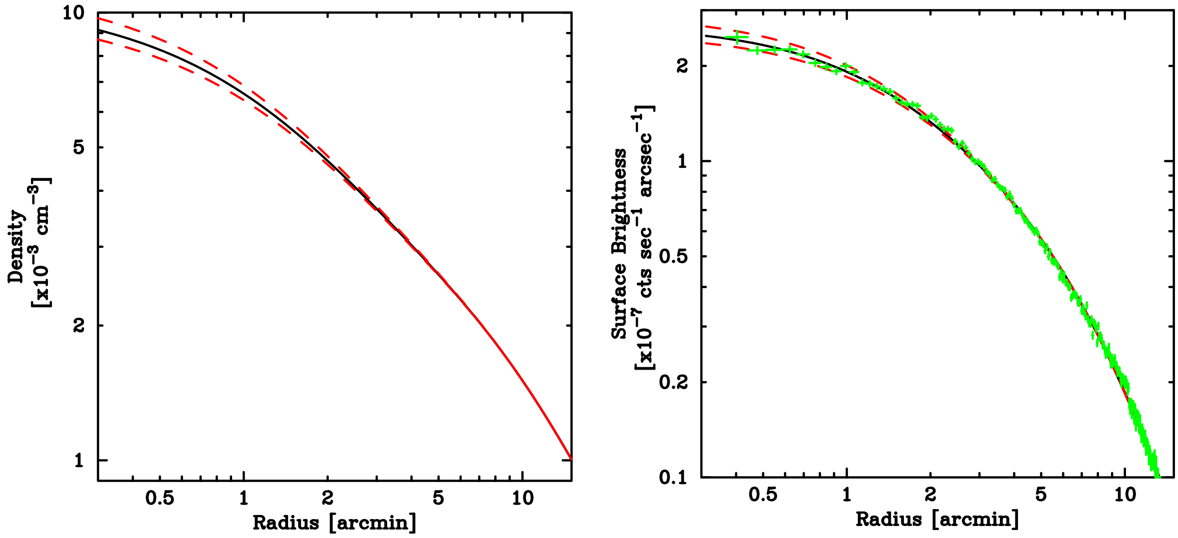

Figure B.3: Density profile (left) after the iteration process with the 90% confidence error and corresponding surface brightness profile (right) in the case of A 1060. The solid and dashed lines shows the best fit value and the 90% confidence level, respectively. In the right panel, the crossed mark shows the observed surface brightness profile.

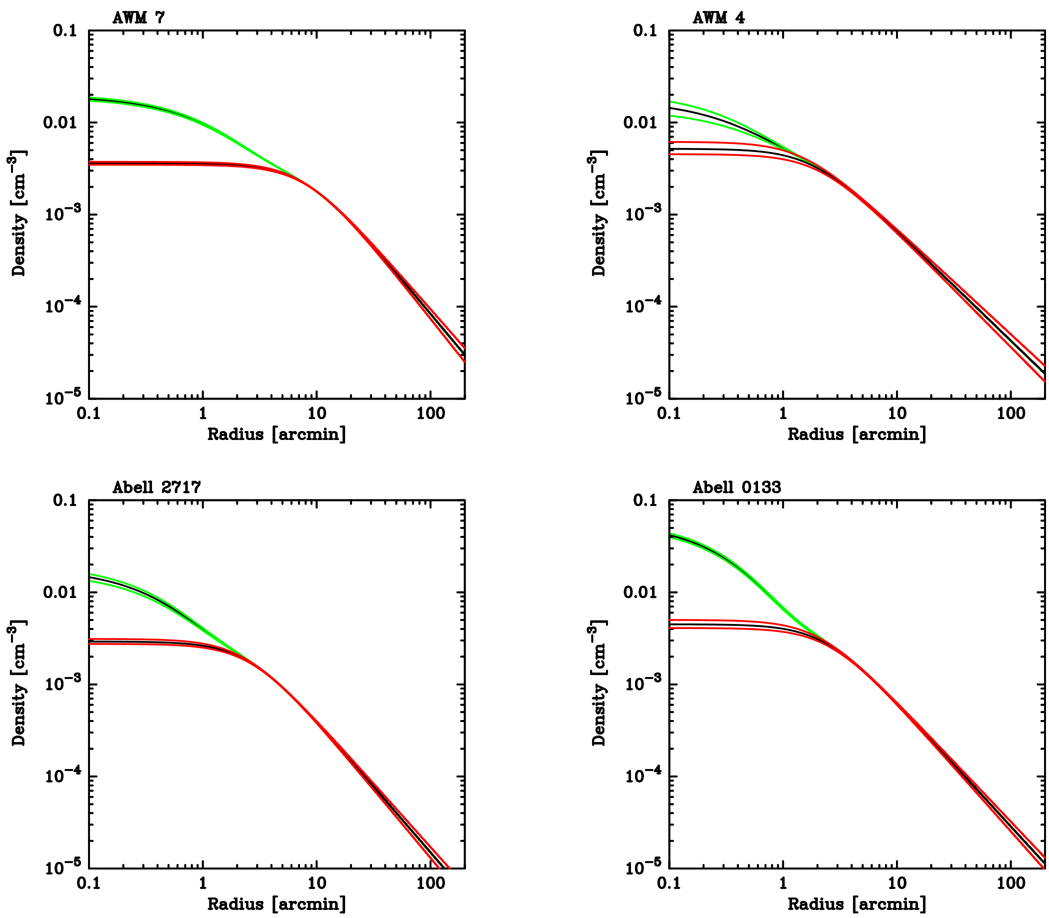

Figure B.4: Superposed density profile with the two different error components of all our sample clusters. The red and green lines show the each error components: estimated by the β-model in the outer region and the exponential function in the inner region, respectively. The error range is the single-palameter 90% confidence level.

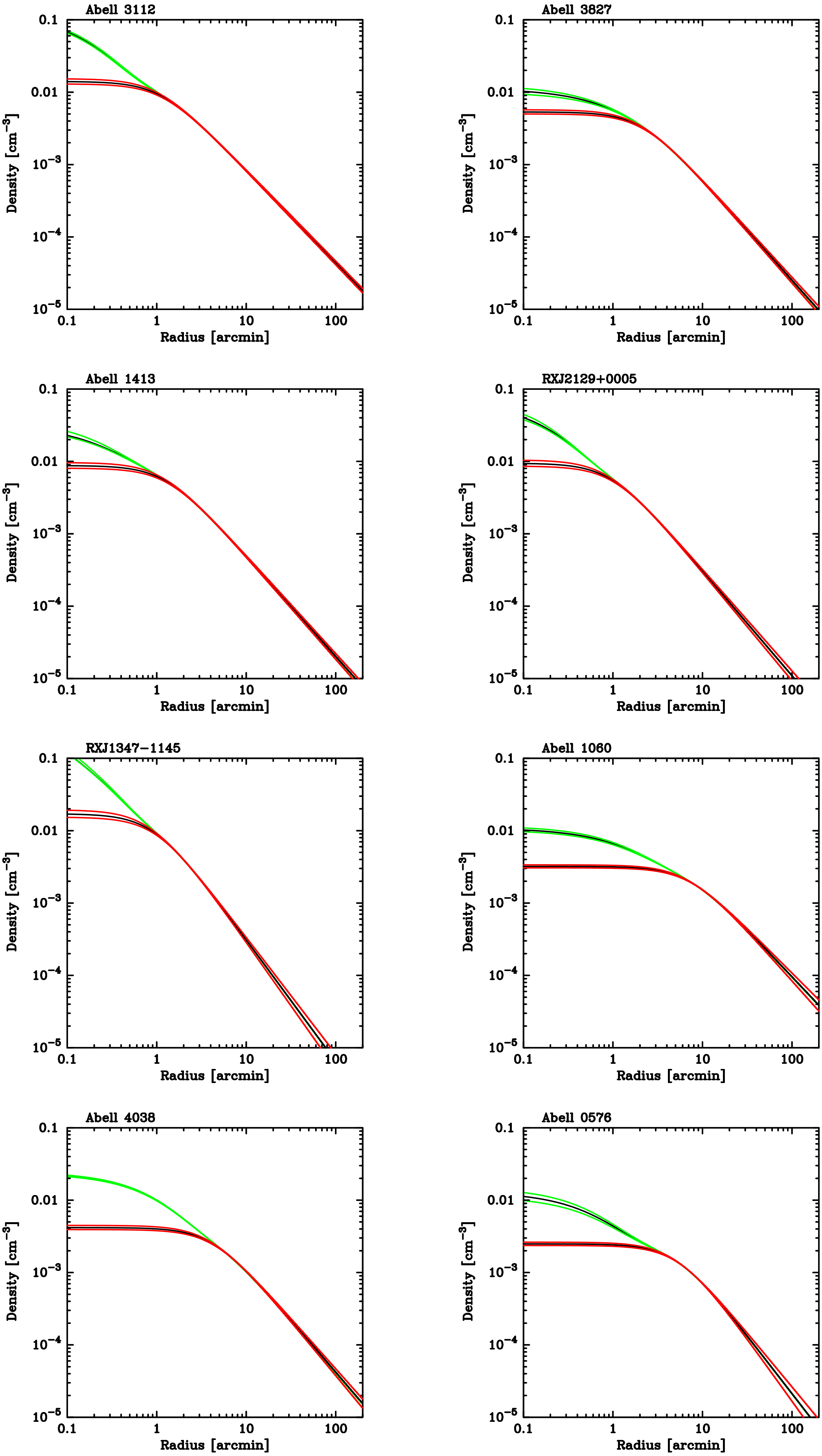

Figure B.5: Continued.

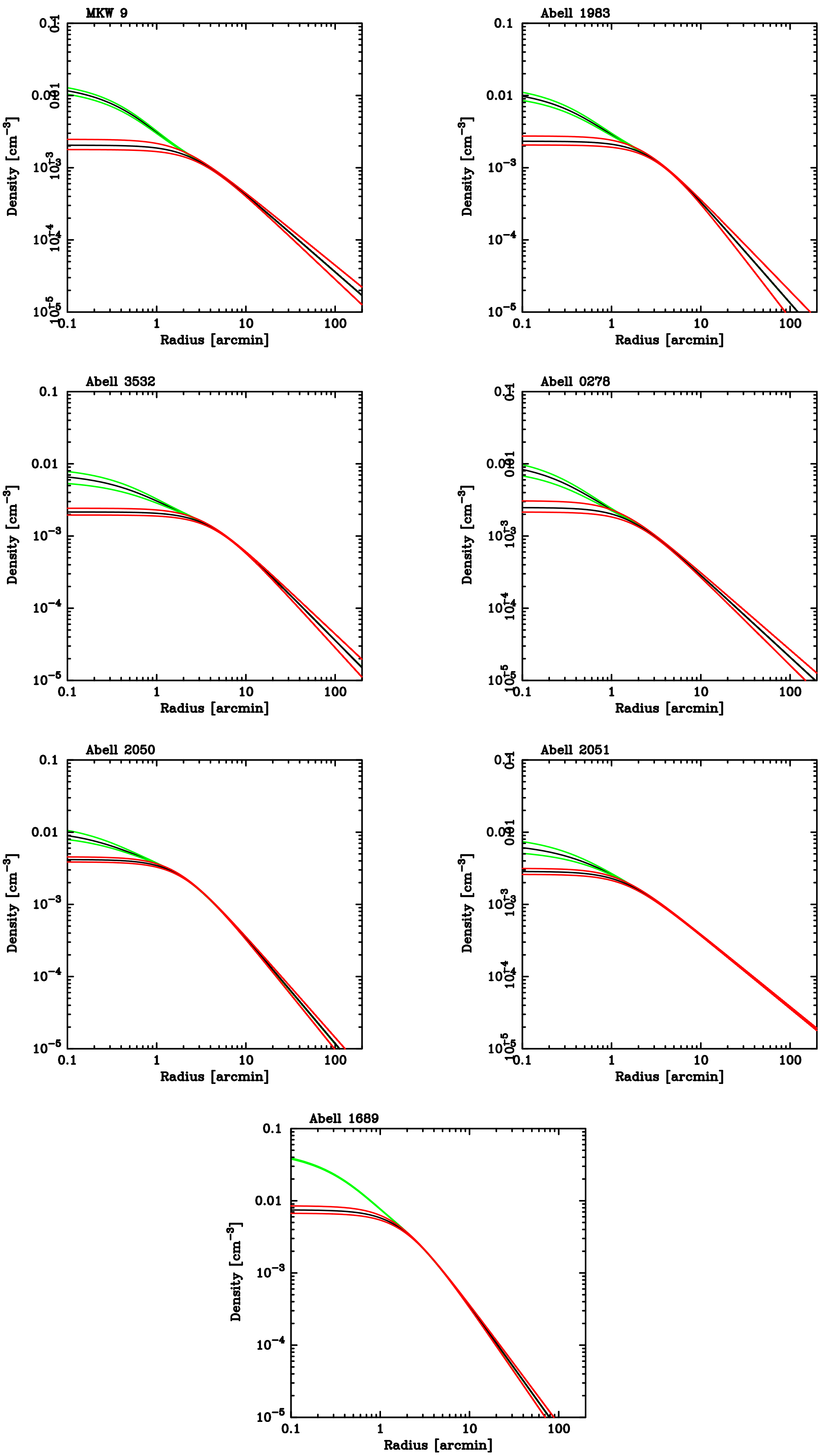

Figure B.6: Continued.

Bibliography

[1] Anders, E., & Grevesse, N. 1989, Acta, 53, 197

[2] Arnaud, M., et al. 2001, A&A, 365, L67

[3] Arnaud, M., & Evrard, A. E. 1999, MNRAS, 305, 631

[4] Bahcall, J. N., & Soneira, R. M. 1980, ApJL, 238, L17

[5] Bryan, G. L., & Norman, M. L. 1998, ApJ, 495, 80

[6] David, L. P., Jones, C., & Forman, W. 1996, ApJ, 473, 692

[7] De Grandi, S., & Molendi, S. 2002, ApJ, 567, 163

[8] De Grandi, S., Ettori, S., Longhetti, M., & Molendi, S. 2004, A&A, 419, 7

[9] de Vaucouleurs, G. 1948, Annales d'Astrophysique, 11, 247

[10] Durret, F., Slezak, E., Lieu, R., Dos Santos, S., & Bonamente, M. 2002, A&A, 390, 397

[11] Durret, F., Lima Neto, G. B., & Forman, W. 2005, A&A, 432, 809

[12] Eke, V. R., Navarro, J. F., & Frenk, C. S. 1998, ApJ, 503, 569

[13] Evrard, A. E., Metzler, C. A., & Navarro, J. F. 1996, ApJ, 469, 494

[14] Fukazawa, Y., Ohashi, T., Fabian, A. C., Canizares, C. R., Ikebe, Y., Makishima, K., Mushotzky, R. F., & Yamashita, K. 1994, PASJ, 46, L55

[15] Fukushige, T., Kawai, A., & Makino, J. 2004, ApJ, 606, 625

[16] Furusho, T., Yamasaki, N. Y., & Ohashi, T. 2003, ApJ, 596, 181

[17] Gehrels, N., & Williams, E. D. 1993, ApJL, 418, L25

[18] Gunn, J. E., & Gott, J. R. I. 1972, ApJ, 176, 1

[19] Hayakawa, A., Furusho, T., Yamasaki, N. Y., Ishida, M., & Ohashi, T. 2004, PASJ, 56, 743

[20] Helsdon, S. F., & Ponman, T. J. 2000, MNRAS, 315, 356

[21] Henry, J. P. 1997, ApJL, 489, L1

[22] Jansen, F., et al. 2001, A&A, 365, L1

[23] Jones, C., & Forman, W. 1984, ApJ, 276, 38

[24] Kaastra, J. S., & Mewe, R. 1993, A&AS, 97, 443

[25] Katayama, H., Takahashi, I., Ikebe, Y., Matsushita, K., & Freyberg, M. J. 2004, A&A, 414, 767

[26] Kikuchi, K., Furusho, T., Ezawa, H., Yamasaki, N. Y., Ohashi, T., Fukazawa, Y., & Ikebe, Y. 1999, PASJ, 51, 301

[27] King, I. 1962, AJ, 67, 471

[28] Koyama, K., Takano, S., & Tawara, Y. 1991, Nature, 350, 135

[29] Leir, A. A., & van den Bergh, S. 1977, ApJS, 34, 381

[30] Liedahl, D. A., Osterheld, A. L., & Goldstein, W. H. 1995, ApJL, 438, L115

[31] Madau, P. 1999, AIP Conf. Proc. 470: After the Dark Ages: When Galaxies were Young, 470, 299

[32] Makino, N., Sasaki, S., & Suto, Y. 1998, ApJ, 497, 555

[33] Markevitch, M., Forman, W. R., Sarazin, C. L., & Vikhlinin, A. 1998, ApJ, 503, 77

[34] Markevitch, M., et al. 2000, ApJ, 541, 542

[35] Mathews, T.A., Morgan, W.W., and Schmidt, M. 1964, ApJ 140, 35

[36] Mazzotta, P., Edge, A. C., & Markevitch, M. 2003, ApJ, 596, 190

[37] Mewe, R., Lemen, J. R., & van den Oord, G. H. J. 1986, A&AS, 65, 511

[38] Moore, B., Quinn, T., Governato, F., Stadel, J., & Lake, G. 1999, MNRAS, 310, 1147

[39] Navarro, J. F., Frenk, C. S., & White, S. D. M. 1996, ApJ, 462, 563

[40] Navarro, J. F., Frenk, C. S., & White, S. D. M. 1997, ApJ, 490, 493

[41] Ota, N., & Mitsuda, K. 2002, ApJL, 567, L23

[42] Peebles, P. J. E. 1980, The Large-Scale Structure of Universe, Princenton University Press, p77

[43] Peebles P.J.E., 1993, Principles of Physical Cosmoligy, Princeton University Press.

[44] Piffaretti, R., Jetzer, P., Kaastra, J. S., & Tamura, T. 2005, A&A, 433, 101

[45] Pizzolato, N., Ventura, P., D'Antona, F., Maggio, A., Micela, G., & Sciortino, S. 2001, A&A, 373, 597

[46] Raymond, J. C., & Smith, B. W. 1977, ApJS, 35, 419

[47] Read, A. M., & Ponman, T. J. 2003, A&A, 409, 395

[48] Rees, M. 1992, in Clusters and Superclusters of Galaxies, Proceedings of NATO Advanced Study Institute, ed. A.C. Fabian (Kluwer Academic Publishers)

[49] Richstone, D., Loeb, A., & Turner, E. L. 1992, ApJ, 393, 477

[50] Roettiger, K., Stone, J. M., & Mushotzky, R. F. 1998, ApJ, 493, 62

[51] Rybicki, G. B., & Lightman, A. P. 1979, Radiative Processes in Astrophysics, John Wiley & Sons, Inc.

[52] Sanderson, A. J. R., Ponman, T. J., Finoguenov, A., Lloyd-Davies, E. J., & Markevitch, M. 2003, MNRAS, 340, 989

[53] Sarazin, C. L. 1988, The X-ray Emission from Cluster of Galaxies, Cambridge: Cambridge University Press, 1988,

[54] Strüder, L., et al. 2001, A&A, 365, L18

[55] Suto, Y., Sasaki, S., & Makino, N. 1998, ApJ, 509, 544

[56] Tamura, T., et al. 1996, PASJ, 48, 671

[57] Tamura, T., Makishima, K., Fukazawa, Y., Ikebe, Y., & Xu, H. 2000, ApJ, 535, 602

[58] Turner, M. J. L., et al. 2001, A&A, 365, L110

[59] Watanabe, M., Yamashita, K., Furuzawa, A., Kunieda, H., Tawara, Y., & Honda, H. 1999, ApJ, 527, 80

[60] White, S. D. M. 1976, MNRAS, 177, 717

[61] Vikhlinin, A., Forman, W., & Jones, C. 1999, ApJ, 525, 47

[62] Vikhlinin, A., Markevitch, M., Murray, S. S., Jones, C., Forman, W., & Van Speybroeck, L. 2005, ApJ, 628, 655

[63] White, D. A. 2000, MNRAS, 312, 663

[64] Xu, H., Ezawa, H., Fukazawa, Y., Kikuchi, K., Makishima, K., Ohashi, T., & Tamura, T. 1997, PASJ, 49, 9

[65] Zwicky, F., & et al. 1961-1968, Catalogues of Galaxies and Clusters of Galaxies, Vol.1-6 Pasadena:Caktech